UNDERWATER ACOUSTIC COMMUNICATION UNDER DOPPLER EFFECTS

Camila Maria Gabriel Gussen

Tese de Doutorado apresentada ao Programa de Pós-graduação em Engenharia Elétrica, COPPE, da Universidade Federal do Rio de Janeiro, como parte dos requisitos necessários à obtenção do título de Doutor em Engenharia Elétrica.

Orientadores: Paulo Sergio Ramirez Diniz
Wallace Alves Martins

Rio de Janeiro
Março de 2018

UNDERWATER ACOUSTIC COMMUNICATION UNDER DOPPLER EFFECTS

Camila Maria Gabriel Gussen

TESE SUBMETIDA AO CORPO DOCENTE DO INSTITUTO ALBERTO LUIZ COIMBRA DE PÓS-GRADUAÇÃO E PESQUISA DE ENGENHARIA (COPPE) DA UNIVERSIDADE FEDERAL DO RIO DE JANEIRO COMO PARTE DOS REQUISITOS NECESSÁRIOS PARA A OBTENÇÃO DO GRAU DE DOUTOR EM CIÊNCIAS EM ENGENHARIA ELÉTRICA.

Examinada por:

Prof. Paulo Sergio Ramirez Diniz, Ph.D.

Prof. Wallace Alves Martins, D.Sc.

Prof. Raimundo Sampaio Neto, Ph.D.

Prof. Lisandro Lovisolo, D.Sc.

Prof. Marcello Luiz Rodrigues de Campos, Ph.D.

RIO DE JANEIRO, RJ – BRASIL
MARÇO DE 2018

Gussen, Camila Maria Gabriel

Underwater Acoustic Communication Under Doppler Effects/Camila Maria Gabriel Gussen. – Rio de Janeiro: UFRJ/COPPE, 2018.

XVI, 144 p.: il.; 29, 7cm.

Orientadores: Paulo Sergio Ramirez Diniz

Wallace Alves Martins

Tese (doutorado) – UFRJ/COPPE/Programa de Engenharia Elétrica, 2018.

Referências Bibliográficas: p. 135 – 144.

1. Digital Signal Processing. 2. Wireless communications. 3. Multicarrier systems. 4. Single carrier systems. 5. Doppler effect. 6. Underwater acoustic communications. I. Diniz, Paulo Sergio Ramirez *et al.* II. Universidade Federal do Rio de Janeiro, COPPE, Programa de Engenharia Elétrica. III. Título.

À vovó Angelina

Agradecimentos

"Ama e faz o que quiseres."
Santo Agostinho

Agradeço a Deus pela vida e pela infinitude.

Agradeço ao meu orientador Paulo Diniz por ter aceitado me orientar e proposto um tema inovador para a tese. Muito obrigada por todo o tempo dedicado a mim neste trabalho. Agradeço também a sua imensa sabedoria e compreensão durante todo o desenvolvimento da tese. A sua sabedoria e paciência proporcinaram condições para que eu conseguisse me desenvolver de forma plena na vida!

Agradeço imensamente ao meu co-orientador Wallace, que, apesar de ter começado a me orientar no período final da tese, conseguiu contribuir de uma forma extraordinária neste trabalho, e também na minha formação profissional. Espero conseguir ser tão objetiva, pragmática e positiva como você!

Agradeço ao professor Marcello Campos que me convidou para participar do projeto da Marinha, assim como por todas as suas contribuições na tese e nos outros projetos que trabalhamos juntos.

Agradeço também aos membros da banca, professores Raimundo Sampaio e Lisandro Loviloso por toda a atenção e tempo dedicados a este trabalho! As sugestões e orientações providas por vocês foram muito importantes e contribuíram muito para a tese.

Agradeço a todas as pessoas do IEAPM (Instituto de Estudos do Mar Almirante Paulo Moreira) que estiveram envolvidas de alguma forma com o desenvolvimento deste trabalho e também com a realização dos experimentos. Em especial, gostaria de agradecer ao Comandante Simões, Fabio Contrera, ao Alexandre Guarino e a todas as outras pessoas do grupo de acústica submarina do IEAPM.

Agradeço também ao CNPQ pelos anos concedidos de bolsa para o desenvolvimento da tese.

Gostaria de agradecer também a todas as pessoas do SMT por todo este período de convivência. Gostaria de agradecer especialmente às meninas Aninha Quaresma, Isabela Apolinário, Iandra Galdino e Bettina D'Ávila por ter passado com vocês momentos maravilhosos. Agradeço duplamente Isabela por me integrar em um

grupo de amigos tão legais e também aos deliciosos bolos e pães trazidos para o laboratório. Agradeço também a Michelle, Gabi, Amanda, Ana Paula e Vanuza por me auxiliarem de diferentes formas durantes este processo.

Agradeço também aos meus amigos do colégio Santo Agostinho, que mesmo depois de tantos anos de formados, continuam presentes na minha vida.

Agradeço também a Patrícia Barbosa, e a Erika Lazary por me ajudarem a ver e a viver a vida sob uma nova perspectiva! Agradeço também ao Victor Souza, Gilberto Schulz e Eckhart Tolle por me ajudarem de diferentes formas neste processo. Agradeço também ao Professor Eduardo por me introduzir na comunidade de meditação Tergar. Agradeço a todas as pessoas que participam da comunidade e especialmente ao Yongey Mingyur Rinpoche, Myoshin Kelley e Edwin Kelley.

Agradeço ao Reinaldo, por sempre ter me apoiado de todas as formas possíveis. Agradeço também por tudo que eu aprendi com você.

Agradeço também a toda a minha família por estar sempre unida e apoiando uns aos outros nos diversos momentos da vida. Agradeço a Tici por estar sempre disponível para conversar comigo e me acalentar em todos os momentos! Gostaria de agradecer especialmente a vovó Angelina, por sempre ter me amado e me aceitado de forma plena, e também por ter me ensinado tanto sobre a vida!

Agradeço imensamente aos meus pais e a minha irmã Clarissa, por sempre me darem amor, carinho e apoio em todos os momentos. Muitas vezes eu não consigo compreender a forma com que vocês transmitem estes sentimentos tão profundos, mas eu sou eternamente grata por vocês serem a minha fortaleza!

Resumo da Tese apresentada à COPPE/UFRJ como parte dos requisitos necessários para a obtenção do grau de Doutor em Ciências (D.Sc.)

COMUNICAÇÃO ACÚSTICA SUBAQUÁTICA SOB EFEITO DOPPLER

Camila Maria Gabriel Gussen

Março/2018

Orientadores: Paulo Sergio Ramirez Diniz
Wallace Alves Martins

Programa: Engenharia Elétrica

Nesta tese foi realizada uma pesquisa extensa sobre as tecnologias existentes para comunicação sem fio subaquática. Foram analisadas as principais características das comunicações acústica, RF e ótica. O estudo foi aprofundado na comunicação acústica, e foi realizada uma análise da resposta em frequência do canal de Arraial do Cabo com dados adquiridos no local. O efeito Doppler, um fenômeno inerente aos canais subaquáticos acústicos, foi investigado de forma minuciosa. Dentre as técnicas estudas para compensação deste efeito, foi escolhido um algoritmo adaptativo, o qual foi re-analisado com uma nova abordagem. Uma versão simplificada deste algoritmo foi proposta para reduzir a quantidade de símbolos pilotos. Foi também desenvolvida uma estratégia para determinar a frequência de retreinamento deste novo algoritmo.

A principal contribuição da tese é a proposta de uma nova estrutura de receptor para compensar o efeito Doppler. Nesta estrutura, é proposta a adaptação de forma iterativa do filtro correlator. A adaptação do suporte temporal deste filtro reduz a interferência inter-simbólica. Além desta ideia, foi demonstrado que a componente de fase do sinal recebido, que é dependente do tempo, deve ser removida em um estágio anterior ao usual. Ou seja, foi proposta uma modificação na sequência do processamento do sinal recebido para melhorar a sua estimativa. Para testar esta nova estrutura do receptor, foi implementado um sistema de comunicação. Foram realizadas simulações numéricas com sistemas de uma única e de múltiplas portadoras. Os resultados das simulações mostram que a nova estrutura pode reduzir a quantidade de erros de bits para altos valores de razão sinal-ruído. A melhora do desempenho pôde ser observada em todas as velocidades relativas testadas, e também para constelações densas.

Abstract of Thesis presented to COPPE/UFRJ as a partial fulfillment of the requirements for the degree of Doctor of Science (D.Sc.)

UNDERWATER ACOUSTIC COMMUNICATION UNDER DOPPLER EFFECTS

Camila Maria Gabriel Gussen

March/2018

Advisors: Paulo Sergio Ramirez Diniz
Wallace Alves Martins

Department: Electrical Engineering

In this thesis we perform a research survey of the three available technologies for wireless underwater communications. We discuss the main features and drawbacks inherent to acoustic, RF, and optical communications. We focus our research on underwater acoustic communications, and we analyze and evaluate the channel frequency response of Arraial do Cabo using data acquired in situ. We further investigate the Doppler effect, a phenomenon that is inherent to underwater acoustic channels. We analyze and justify a compensation algorithm to mitigate the Doppler effects. We propose a simplified algorithm version for minimizing the required number of pilot symbols. We also develop a simple strategy to determine how often our proposed compensation method should be retrained.

Our main contribution is the proposal of a new receiver design to deal with Doppler effects. We present the idea of iteratively adapt the correlator filter placed at the receiver side. We show that the adaptation of this filter's support reduces the inter-symbol interference of the estimated symbols. Besides this idea, we demonstrate that the time-dependent phase-shift component of the received signal should be removed beforehand. That is, we propose a modification in the signal processing sequence blocks for improving the symbol estimation. For testing and comparing this new receiver design, we implement a communication model encompassing physical layer aspects. We perform several numerical simulations for single-carrier and multicarrier systems. Simulation results show that our proposal might provide a reduction in the bit error rate for high signal-to-noise ratios. This performance improvement can be observed for all tested relative movement, and even with dense digital signal constellation.

Contents

List of Figures

List of Tables

Chapter 1

Introduction

There is an increasing interest in monitoring phenomena in underwater environment both in the ocean as well as and inland in lakes and rivers. For certain, wireless communications will play a key role in practical solutions. The applications include: oil and gas exploitation, security, environmental-impact monitoring, navigation, ocean-pollution control, among others. This work discusses some key issues related to underwater communications in general, focusing on proposing some possible solutions for underwater acoustic communications.

1.1 Motivation

Underwater wireless communications present new and distinct challenges when compared to wired and wireless communications through the atmosphere, requiring sophisticated devices to achieve relatively low transmission rates, even over short distances. As a result, one can find very few off-the-shelf solutions for reliable and economically viable underwater communications. This trend will certainly change in the near future.

There are three main technologies for underwater wireless communications [3, 4]. The first technology is underwater acoustic communications [5, 6] which allows a relatively long range of communication, but achieves low throughput and is highly impaired by Doppler effects. The second technology is the radio-frequency communications [7, 8] usually featuring very short range, higher data throughput than the acoustic solution, and whose Doppler effects are not so relevant. The third technology is the optical transmission [2, 9] in the blue-green wavelength range[1], which is not affected by Doppler effects, but it requires line-of-sight alignment. Nonetheless, for all these technologies, it is important to consider both the implementation costs

[1]The blue-green wavelength is the frequency range which enables the longest transmission distance for optical transmissions.

associated with a target data throughput for a prescribed communication range and the relative transmission power that might lead to impacts in marine life.

The correct exploitation of the ocean environment for communications requires a clear understanding of the mechanisms affecting the underwater signal such as the attenuation properties originated from the propagation characteristics of acoustic, RF, and optical transmissions. Assuming that a reliable underwater communication is targeted, the challenge would be proposing a flexible communication system using the aforementioned communication types. This flexible system could be intelligent so that the maximum transmission rate could be achieved considering, for instance, environmental conditions, distance and relative movement between transmitter and receiver. In addition, since all underwater communication systems have inherent limitations with respect to connections over long distances, the use of networks including several sensors and relays, with the aid of smart protocols, would be the natural solution [4].

1.1.1 Underwater Wireless Communications

An illustrative example of an underwater environment capitalizing on multiple communication technologies is depicted in Figure 1.1. Signal communication in such environment might include several possibilities such as links from land to satellite, then to buoy ship and/or oil platform. It is also possible to exchange data through RF antennas located at floating devices and land stations. Communication devices might be attached to floating structures to allow the exchange of information with stations placed underwater. In the water environment, it is possible to deploy numerous different types of communication nodes consisting of remotely operated vehicles (ROV's), local area wireless and wired networks. Some devices might be anchored or attached to the bottom of the seafloor.

In such flexible communication environment, it is possible to establish a software-defined network (SDN) where a large number of communication devices, each one with its inherent features, can exchange data. Considering that wireless link is a highly desirable feature for underwater applications, a proper knowledge of the physical constraints on the information passage over the physical layer must be acquired.

1.2 Objective

The objective of the first part of this thesis is to provide an overview of the three available technologies for wireless underwater communications, as well as to present their main challenges. The discussion about the main features and drawbacks inher-

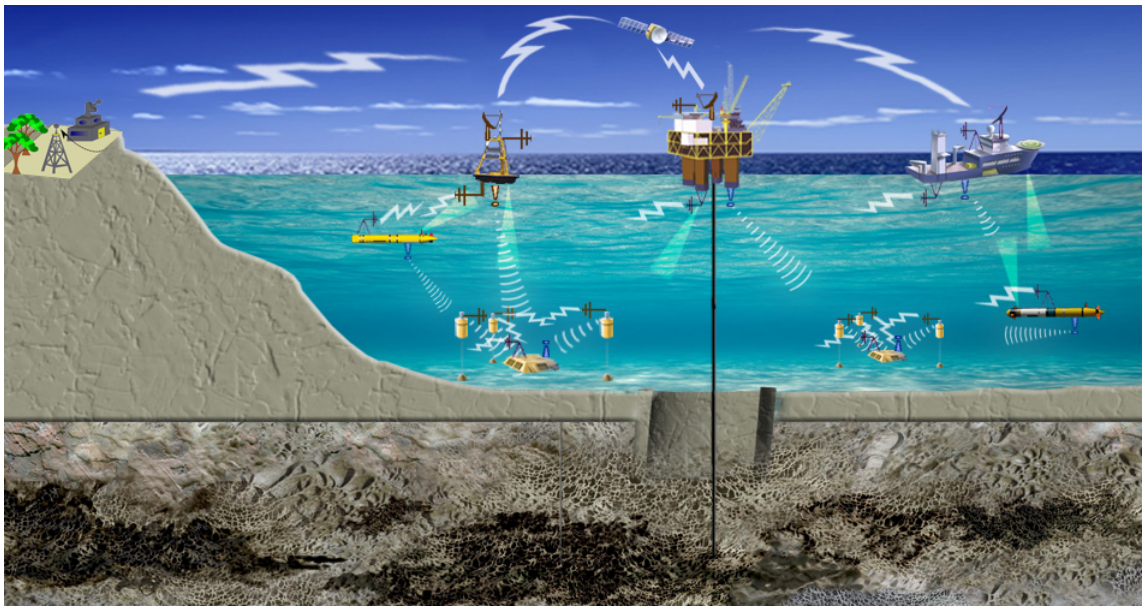

Figure 1.1: Scenarios of multiple communication technologies.

ent to acoustic, RF, and optical communications aims to give directions for choosing the most suitable technology under certain system requirements and environmental conditions.

In the second part of the thesis lies the main original contributions. In this part we further study underwater acoustic communications. One of the main reasons we focus our studies on this technology is the fact that it allows communications over longer distances than the other technologies. Despite the modeling of the underwater signal propagation being very difficult, its understanding plays a key role in determining the effective data processing at the transmitter and at the receiver to yield a reliable and accurate communication link. In order to achieve improved system performance, we study in detail the Doppler effect, a phenomenon that is inherent to underwater acoustic channels originating from the low propagation speed of the signals. We also study and analyze some available solutions to reduce the Doppler effect. Our main contributions are the proposals of new receiver designs for dealing with Doppler effect.

1.3 Contributions

In this thesis, we provide an overview of the three available technologies to transport information in the underwater environment. The importance of such survey lies in the fact that the knowledge of the environmental conditions in which the system has to operate, combined with the application requirements, might help the selection of a proper solution. Thus, in this thesis we analyze the main features and drawbacks inherent to each communication system: RF, optical and acoustics [4], [10].

In addition to the aforementioned survey, we performed an analysis concerning the channel frequency response of an underwater acoustic channel. In this work, we utilized data collected in situ for acquiring some knowledge about the channel frequency response in Arraial do Cabo, which has a Brazilian Navy monitoring station [11].

As part of our initial research concerning Doppler effects, we analyzed these effects in an RF communication over the air. In this study, we investigate how the Doppler spread affects the performance of block transceivers with reduced redundancy, in order to access, for the first time, the ability of these transceivers to cope with time-varying channels inherent to moving transmitter and/or receiver [12]. The expected benefit of these transceivers is a higher data throughput when compared to orthogonal frequency-division multiplexing (OFDM) and single-carrier frequency domain equalizer (SC-FDE) systems.

Another contribution of this thesis is the analysis and justification of an existing compensation algorithm to mitigating Doppler effects. We propose a simplified algorithm version in which pilot symbols are not available. For testing this new algorithm version, we also developed a simple strategy to determine how often the compensation method should be retrained before losing track of the received signal time scaling. Thus, the required amount of pilot symbols might be minimized, yielding higher system throughput.

Our main contribution is the proposal of a new receiver design to deal with Doppler effects. With a detailed analysis, we present our idea of iteratively adapt the correlator filter placed at the receiver side. We show that the adaptation of the support of this filter reduces the inter-symbol interference of the estimated symbols. Besides this idea, we demonstrate with another system model and via a numerical analysis that the time-dependent phase-shift component of the received signal should be removed beforehand. That is, we propose a modification in the signal processing sequence blocks for improving the symbol estimation.

Besides the aforementioned studies, we implemented a communication model encompassing the physical layer in order to test and compare the proposed receiver modifications. We provide an analysis regarding the benefits and the trade-off in employing our receiver structure with single-carrier and multicarrier systems. We show that this new receiver design might provide a reduction in the bit error rate at high signal-to-noise ratio. This performance improvement was observed for all tested relative velocities between transmitter and receiver, and even with dense digital signal constellation.

1.4 Thesis Outline

This thesis is organized as follows. Chapter 2 presents a survey on the available technologies for underwater wireless communications, discussing the main features and limitations of the three technologies: RF, optical and acoustics. In this chapter, we investigated further underwater acoustic communications. A comparison among the three technologies is also provided at the end of that chapter.

Chapter 3 introduces the system model employed along the thesis. We present some possible transmitter and receiver configurations, such as the usage of single-carrier or multicarrier transceivers. Other setup possibilities, such as the redundancy types zero-padding (ZP) or cycle prefix (CP), and the use of distinct guard interval durations are also shown. In this chapter we appended a work[2] that analyzes how the Doppler effect may disturb the performances of multicarrier and single carrier transceivers with distinct redundancy lengths in RF communications over the air. In the same chapter we analyze an underwater acoustic channel. We compute the channel frequency response of Arraial do Cabo, using field data, and with a ray tracing program.

Chapter 4 analyzes and justifies an algorithm for estimating and compensating the Doppler effect. In this chapter we also propose an algorithm simplification for dealing with scenarios with few pilot symbols. We also present a procedure to determine how often this algorithm version should be trained. At the end of this chapter, simulations are shown to assess the performance of the proposed procedure.

Chapter 5 presents our proposal for Doppler effect estimation and compensation. In this chapter, we introduce the idea of iteratively adapting the correlator filter[3] in order to reduce the intersymbol interference of the estimated symbols. Besides that, we propose a method to remove first the signal phase distortion, yielding a modification in the signal processing sequence blocks.

Chapter 6 presents the entire communication model implemented for testing the distinct receiver designs proposed in Chapter 5. We analyze with simulations the receiver's performances of single carrier and multicarrier systems for distinct relative movements, and for distinct digital modulation constellations. The obtained results show a performance improvement of the proposed receivers when operating in high SNR environments. It is important to highlight that these performance gains were obtained for all tested relative movement between transmitter and receiver.

Chapter 7 draws some conclusions, and also proposes some research problems to be addressed in the future.

[2]This work is presented in Appendix C, and was developed as an initial case study.

[3]The original idea of this filter is to be matched with the transmitted pulse shaping.

1.5 Notation

In this thesis we employed the following notations: vectors and matrices are represented in bold face with lowercase letters and uppercase letters, respectively. The notations $[\cdot]^T$, $[\cdot]^*$, $[\cdot]^H$, $[\cdot]^{-1}$ stand for transpose, conjugate, Hermitian (transpose and complex conjugation), and inverse operations in $[\cdot]$. The operation $x(t) * h(t)$ denotes the linear convolution of $x(t)$ with $h(t)$. $\mathbb{C}$, $\mathbb{R}$, $\mathbb{N}$ denote the set of complex, real, and natural numbers, respectively. $\Re$ returns the real part of a complex number. The symbols $\mathbf{0}_{M\times K}$ and $\boldsymbol{I}_M$ denote an $M \times N$ matrix with zeros and an $M \times M$ identity matrix, respectively.

Chapter 2

A Survey on Underwater Communications

The focus of this chapter is to provide a survey on key features inherent to the available underwater wireless communication technologies, putting into perspective their technical aspects, current research challenges, and to-be-explored potential.

We start the chapter discussing the radio frequency technology in Section 2.1, wherein we present the main features and limitations of this technology regarding the sea conditions. We introduce the optical technology in Section 2.2, along with the main environmental conditions that may affect its employment. The last technology to be presented is the acoustics in Section 2.3. As the main contributions of the thesis are related to underwater acoustic communications, we performed a further investigation on this technology. We conclude this chapter with a comparison among these technologies in Section 2.4.

2.1 Underwater RF Communications

One of the early attempts to perform underwater communications utilized radio-frequency electromagnetic transmissions. The first trials date back to the late 19th century being revisited in the 1970's [7]. The impression left by the pioneering work in the RF range was that electromagnetic signals were not suitable for underwater communications.

2.1.1 Electromagnetic Waves Overview

According to the physics, for the frequency ranges employed by mobile services, TV, radio, and satellite communications, the seawater is highly conductive, thus seriously affecting the propagation of electromagnetic waves. As a result, it is not easy to perform communications at both very- and ultra-high frequency ranges (VHF and

UHF, respectively) as well as at even higher frequencies, for distances beyond 10 meters [3]. Indeed at lower frequencies, namely at extremely and very-low frequency ranges (ELF and VLF, respectively), the electromagnetic-wave attenuation can be considered low enough to allow for reliable communications over several kilometers of distance [7]. Unfortunately, these frequency ranges from 3 Hz to 3 kHz and 3 kHz to 30 kHz are not wide enough to allow transmissions at high data rates. In addition, such small frequencies require large receiving antenna, which can hinder the applicability of the RF technology in some applications of underwater communications. The ELF and VLF frequency ranges are used for navy and environmental applications. For example ELF and VLF have been considered for communication from land to submerged submarines [13], [14] and [15]. The VLF range has been also used to monitor atmospheric phenomena such as lightning location [16]. Moreover, as expected, the longer the distance between transmitter and receiver, the lower is the reachable data rate. At short distances it is possible to achieve higher data throughput than acoustic-based solutions by employing frequency ranges beyond ELF and VLF.

Besides, this technology is much less affected by Doppler effects than acoustic communications. It should be mentioned that the propagation speed of the electromagnetic field increases with frequency in the water as described in the following equation [8]:

$$c_{\mathrm{RF}} = 2\sqrt{f\pi/(\mu_0\sigma)} \tag{2.1}$$

where f is the frequency in hertz, $\mu_0 = 4\pi \times 10^{-7}$ H/m is the free space permeability, and σ is the water conductivity. It is important to highlight that the above equation is valid for the propagation of the electromagnetic wave in a conductor medium. It is also worth mentioning that in free-space the wave speed propagation is approximately constant with respect to frequency.

As an example, in Table 2.1 we list some wave propagation velocities for seawater and fresh water. The main difference between these two water types is the conductivity: $\sigma = 4.3$ Siemens/meter for seawater and $\sigma = 0.001$ Siemens/meter for fresh water, resulting in different wave propagation velocities [7]. It is worth mentioning as illustration that the salinity in the Baltic sea is lower than in the open ocean. The salinity of the Baltic sea is $S = 8$ ppt (parts per thousands) while in open ocean is around $S = 35$ ppt, resulting in conductivities of $\sigma = 0.88$ Siemens/meter and $\sigma = 3.35$ Siemens/meter, respectively, for $T = 5$ degrees Celsius. The conductivities are one order of magnitude different from each other, resulting in a better propagation of electromagnetic waves in the Baltic sea. The air conductivity lies in the range 3×10^{-15} to 8×10^{-15} Siemens/meter. However, as the air is a dieletric

Table 2.1: Speed of propagation in m/s

	10^2 Hz	10^3 Hz	10^4 Hz	10^6 Hz
Seawater	1.52×10^4	4.82×10^4	1.52×10^5	1.52×10^6
Fresh water	1.00×10^6	3.16×10^6	1.00×10^7	1.00×10^8

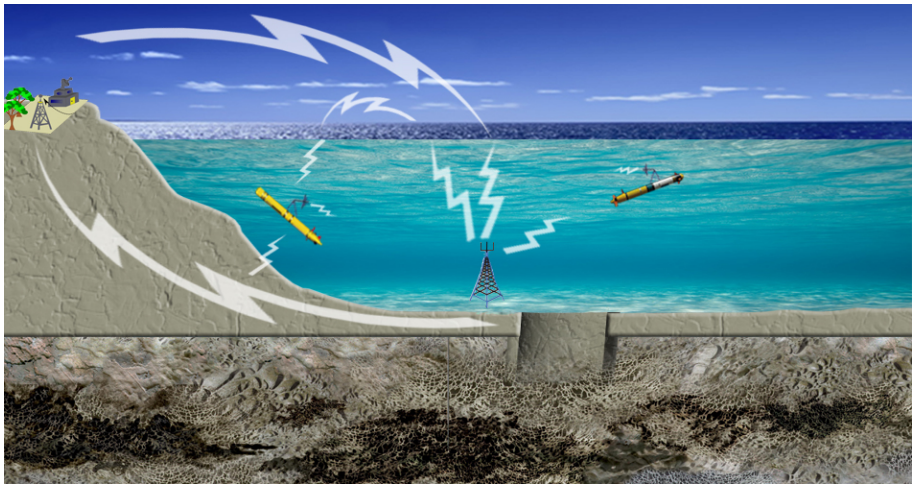

Figure 2.1: Multipath propagation of an RF signal.

medium, it is not possible to calculate the wave propagation velocity in the air using Eq. (2.1).

2.1.2 RF Signal Fading

The RF signal suffers from multipath as illustrated in Figure 2.1. This signal can cross the water-air boundary as well as can propagate through the seabed. Hence, it is possible to use these multiple paths to increase the signal propagation distance in shallow water, and as a consequence, a submerged station can transmit information for an onshore station [8].

As the propagation speed of RF signals in the water is higher than for acoustic signals [7], we can expect to be less affected by Doppler effects. In part, we can capitalize on the knowledge of the free-space RF propagation to deal with the modeling of the underwater RF propagation. Therefore, we can access the multipath fading and the techniques used for the mitigation of the intersymbol interference.

The typical attenuation model in seawater follows the behavior [8]

$$\alpha(f) = \kappa\sqrt{f}, \tag{2.2}$$

where f represents the RF (carrier) signal frequency in Hertz and

$$\kappa = \sqrt{\pi\sigma\mu_0}, \tag{2.3}$$

with σ representing the water conductivity in Siemens/meters, $\mu_0 \approx 4\pi\, 10^{-7}$ H/m (Henrys per meter) being the vacuum permeability. In the above description $\alpha(f)$ represents the channel attenuation per meter.

The corresponding channel model transfer function is described by

$$H(f) = |H(f)|\mathrm{e}^{-\mathrm{j}\theta(f)} \tag{2.4}$$

with

$$|H(f)| = H_0\mathrm{e}^{-\kappa\sqrt{f}d}, \tag{2.5}$$

where H_0 is the DC channel gain, and d represents the distance between transmitter and receiver. For a fixed frequency, the channel magnitude response decreases exponentially with distance. In the literature, it is common to consider the distance where the signal power is reduced by $\frac{1}{\mathrm{e}}$, known as skin depth [8]. This parameter is given by

$$\delta_{\text{skin}} = \frac{1}{\kappa\sqrt{f}} = \frac{1}{\sqrt{\pi\sigma\mu_0 f}} \tag{2.6}$$

in unit of meters. It is worth mentioning that the attenuation in RF transmissions is usually given in dB per meter, whereas the acoustic signal attenuation is given in dB per kilometers, reflecting the higher attenuation of the RF signal.

The conductivity in the seawater is around 4.3 Siemens/meter, whereas in the fresh water is in the range of 0.001 to 0.01 Siemens/meter. As a result, it is expected that the attenuation of the RF signal is higher in the seawater than in the fresh water, considering that the higher conduction of the seawater has more impact in attenuating the electric field, as indicated by Eqs. (2.2) and (2.3). The permeabilities of seawater and fresh water are around the same.

In the seawater case by taking into consideration that $\sigma \approx 4.3$ Siemens/meter the skin depth is around

$$\delta_{\text{skin}} \approx \frac{0.2427 \times 10^3}{\sqrt{f}}, \tag{2.7}$$

corresponding to an attenuation of (see Eqs. (2.2), (2.6))

$$\alpha(f) \approx \frac{1}{242.7}\sqrt{f}, \tag{2.8}$$

so that for a frequency of transmission at 1 MHz the signal power would decrease by 1/e in approximately 0.2427 meters.

In Figures 2.2 and 2.3 it is possible to observe the magnitude variation of the

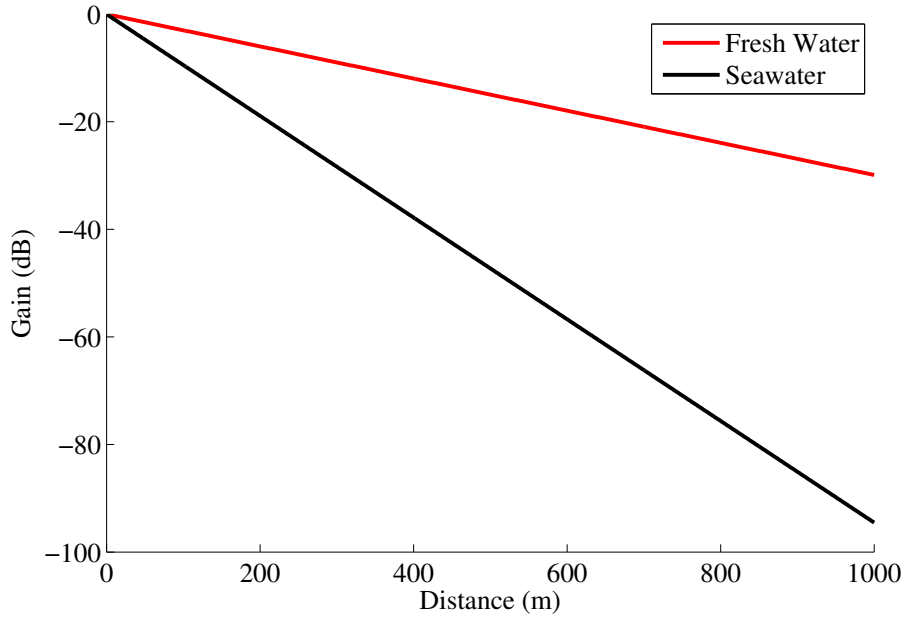

Figure 2.2: Channel gain *versus* distance for $f = 3$ kHz.

channel frequency response with respect to the distance for $f = 3$ kHz and $f = 30$ kHz respectively, considering $H_0 = 1$. From Figures 2.2 and 2.3, we can also see that the low frequency ($f = 3$ kHz) achieves a longer distance for the same attenuation. Comparing the attenuation for seawater and for fresh water, we observe that for the same frequency and distance, the corresponding attenuation is always lower for fresh water.

In Figures 2.4 and 2.5 it is shown the magnitude variation of the channel frequency response with respect to the frequency, considering $H_0 = 1$, $d = 0.5$ m and $d = 1$ m for fresh water and seawater, respectively. It is possible to observe that for $d = 0.5$ m, the attenuation is always lower than for $d = 1$ m for the two water types. In addition, freshwater always presents lower attenuation than seawater meaning that it is possible to transmit over longer distances in this medium.

Figures 2.6 and 2.7 illustrate the magnitude variation of the channel response with respect to the frequency and distance, for $H_0 = 1$, considering fresh water and seawater, respectively. As observed before, the attenuation for seawater is always higher than for fresh water for all distances and frequencies. Moreover, low frequency and distance leads to less attenuation for all water types.

According to the literature, it appears that undersea RF transmissions typically requires higher power-per-bit transmission and achieve lower communication range than acoustics communications. However, for short ranges and considering its much lower sensitivity to Doppler effects, the RF transmission is a sure candidate to complement the achievements of acoustic and optical communication solutions.

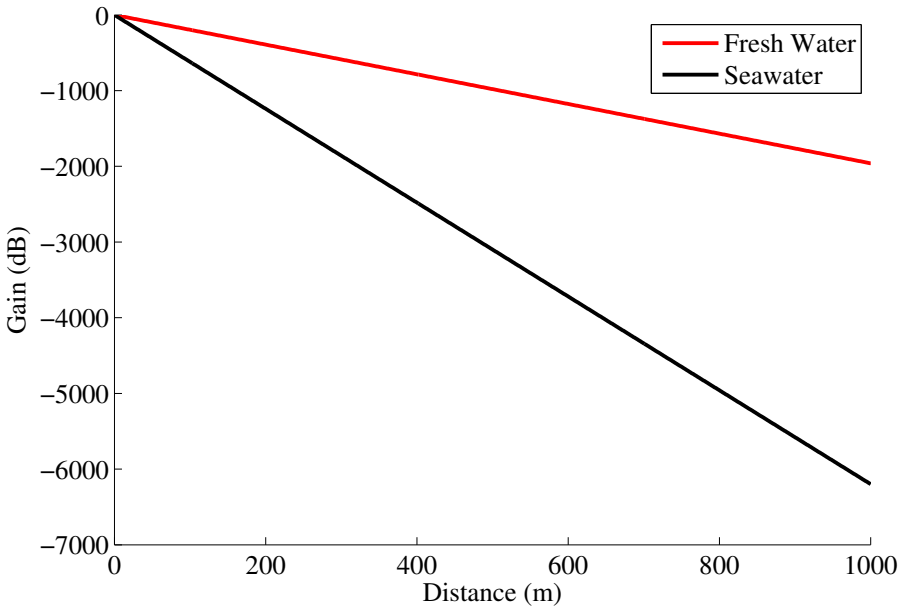

Figure 2.3: Channel gain *versus* distance for $f = 30$ kHz.

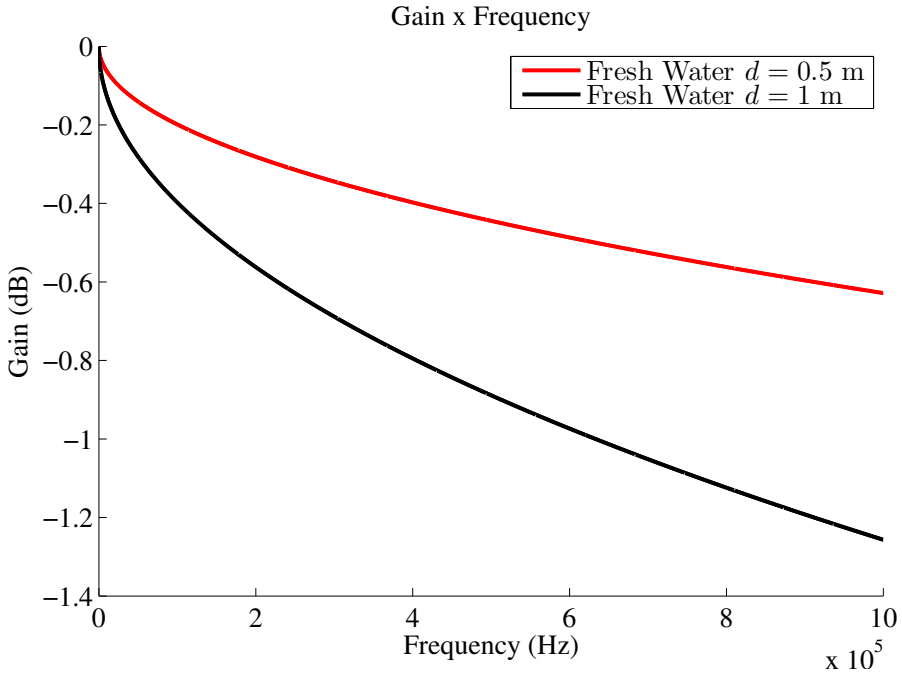

Figure 2.4: Channel gain *versus* frequency for fresh water.

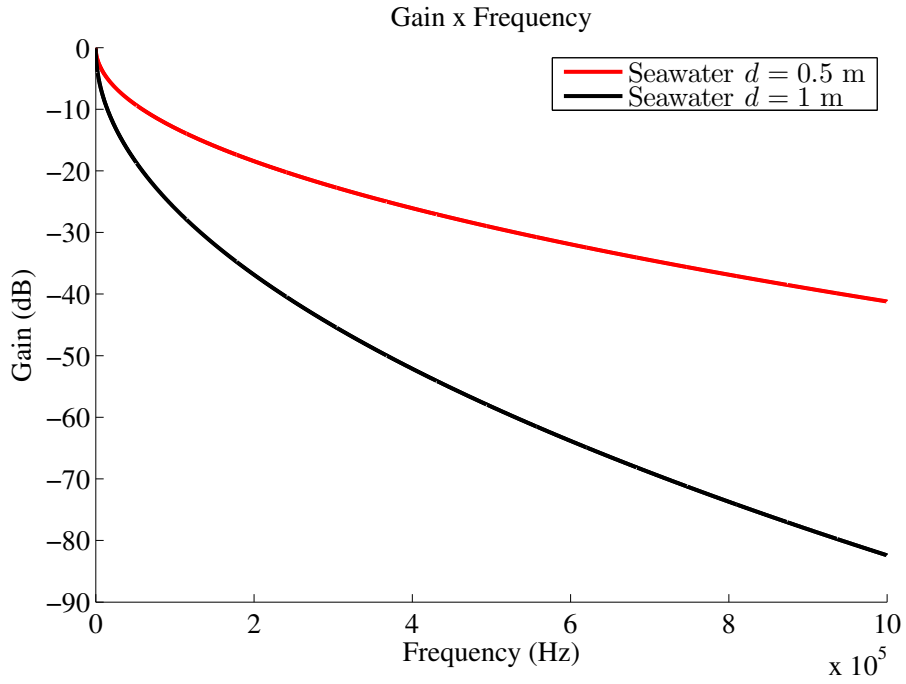

Figure 2.5: Channel gain *versus* frequency for seawater.

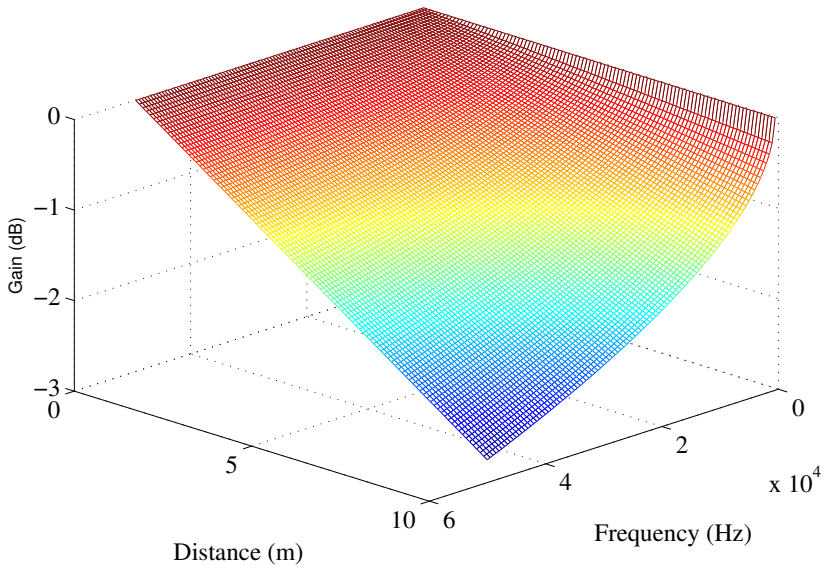

Figure 2.6: Channel gain *versus* frequency and distance for fresh water.

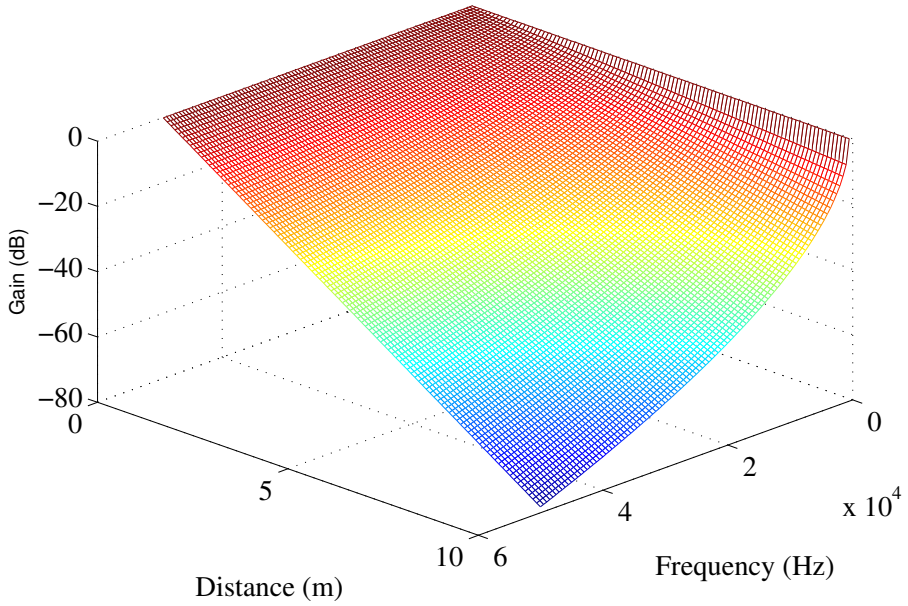

Figure 2.7: Channel gain *versus* frequency and distance for seawater.

Noise in Underwater RF Communications

RF propagation and noise models in underwater environments are not widely discussed in the open literature. One of the few exceptions is the work of [17] suggesting that the environment noise follows a probability density function similar to the Gaussian distribution with zero mean.

RF Transducers

The RF underwater transmission requires two transducers, namely a transmitting antenna and a receiving antenna. Their role is to convert electric signal into electromagnetic field and electromagnetic field into electric signal, respectively. The antennas are properly encapsulated for their operation in the underwater environment.

Typically the antennas' lengths are related to their shape aiming at a prescribed radiation pattern. A common type of antenna is the $\frac{\lambda}{2}$ dipole whose overall length of the antenna is half of the wavelength, and another widely used type is the $\frac{\lambda}{4}$ monopole antenna.

2.1.3 Main Concerns in RF Communications

The main drawbacks concerning RF technology relate to severe constraints on data rates and on propagation distances. These are the main reasons for the small number of products using this communication technology so far. Nonetheless, there are some

applications in which alternative technologies based on acoustic or optical transmissions are not viable solutions. For example, a suitable technology for monitoring seabed sediments in order to control coastal erosion is through the deployment of a sensor network that can exchange information through RF signals [8].

2.2 Underwater Optical Communications

Optical wireless underwater communications can be a complementary transmission technique to underwater acoustic communications. Underwater optical communications can provide higher data rates, however, the propagation range is limited up to a few hundred meters [3].

The main difference between RF and optical propagation in seawater is the medium behavior: the water is seen as conductor for RF and as dielectric for optical propagation. The explanation for this phenomenon lies on the plasma frequency, which is a frequency that determines the range of frequencies that the medium behaves as a conductor or as a dielectric. For seawater, the plasma frequency is 250 GHz [3], meaning that seawater behaves as a conductor for $f < 250$ GHz and as a dielectric for $f > 250$ GHz.

2.2.1 Optical Signal Propagation Overview

The propagation of the optical signal depends on environmental conditions, that are strictly connected to the attenuation of the optical waves. The attenuation of light in water is caused by absorption and scattering. In seawater, the photons can be absorbed by molecules of water, chlorophyll in phytoplankton, dissolved salts in the water and colored dissolved organic matter (CDOM). In Subsection 2.2.2, a model of these phenomena is given. Besides the dependence on environmental conditions, the propagation of the optical signal is frequency dependent, meaning that each light wavelength will undergo different attenuation. The "blue-green optical window" has lower attenuation and this knowledge has been used for improving blue-green sources and detectors as discussed in [18].

Typically the optical communication requires line-of-sight between transmitter and receiver, which requires some sort of direction tracking to maintain the communication link. Considering the environmental conditions that affect specifically optical communications, the water has been classified in different ways. The two main classifications, which are related with the water turbidity, are the *Jerlov Water Types*, that has three major classes and an alternative classification which considers four water types. According to [3], Jerlov divided the water types in these three main classes:

- I - Clearest water: examples of this water type is the mid-Pacific and Atlantic oceans;
- II - Intermediate water: this water type is typical of Northern Pacific ocean;
- III - Murkiest water: typical of the North Sea and Eastern Atlantic.

The alternative classification considered in [1], [2] is the following:

- Pure seawater: the major attenuation for this water type is absorption;
- Clear ocean water: this water type is also affected by scattering due to a higher concentration of particles in comparison with pure seawater;
- Coastal ocean water: this water type has even higher concentration of particles that affect the scattering and the absorption;
- Turbid harbor and estuary water: this water has the highest concentration of particles.

Typical values of the attenuation for these water types are available in Subsection 2.2.2.

2.2.2 Optical Signal Fading

The water when used as a medium for wireless optical communication has two important types of properties that will influence light propagation: Inherent Optical Properties (IOPs) and Apparent Optical Properties (AOPs). Inherent optical properties depend only on the medium (water) while apparent optical properties depend on the light source characteristics, e.g., if the laser source produces collimated or diffuse rays and depend also on IOP [19]. As stated in [19] for optical underwater wireless communications, IOP is more relevant and therefore will be explained here.

The two main inherent optical properties are the spectral absorption coefficient and the spectral volume scattering function [1]. The volume scattering function is the main IOP for describing scattering while the spectral absorption coefficient quantifies absorption.

Absorption is the process that transforms the electromagnetic radiation into heat, i.e., the energy that would be re-emitted is absorbed [1, 3, 9]. We will denote as $a(\lambda)$ the spectral absorption coefficient, with λ being the wavelength. The absorption occurs at chlorophyll in phytoplankton, at the colored dissolved organic matter (CDOM), at the water molecule, and at dissolved salts in the water [19].

The direction of the photons changes due to scattering. Scattering can be originated by salt ions in pure water and by particulate matter [19]. Scattering by objects

smaller than the light wavelength is described by Rayleigh model, whereas scattering by objects greater than the light wavelength is described by Mie theory [3]. The spectral volume scattering coefficient designates the ratio of the scattering energy loss and the transmitted energy per unit of distance, and it is denoted herein as $b(\lambda)$ [20].

The beam attenuation coefficient is related to the total energy that is lost due to absorption and scattering, and is defined as [1, 9, 21]

$$c(\lambda) = a(\lambda) + b(\lambda). \tag{2.9}$$

Many applications employ also the back-scattering coefficient $b_{\mathrm{b}}(\lambda)$, which is the part of the scattering coefficient related to the amount of light that returns to the transmitter. This coefficient can be used to estimate water quality: the knowledge of the water turbidity can be important to the design of smart transmitters, which are able to change transmission power and data rate accordingly [9].

Typical values for absorption coefficient $a(\lambda)$, scattering coefficient $b(\lambda)$, and beam attenuation coefficient $c(\lambda)$ are shown in Tables 2.2 and 2.3, whose values are taken from [1] and [2] respectively. In addition, Table 2.2 presents typical values of backscattered coefficient $b_{\mathrm{b}}(\lambda)$ and of chlorophyll concentration C_{c}.

Table 2.2: Values for beam attenuation coefficient, absorption coefficient, scattering coefficient, backscattered coefficient and chlorophyll concentration from [1]

Water type	$c(\lambda)$	$a(\lambda)$	$b(\lambda)$	$b_{\mathrm{b}}(\lambda)$	C_{c}
Pure seawater	0.056	0.053	0.003	0.0006	0.005
Clear ocean	0.150	0.069	0.080	0.0010	0.310
Coastal ocean	0.305	0.088	0.216	0.0014	0.830
Turbid harbor	2.170	0.295	1.875	0.0076	5.900

Table 2.3: Values for beam attenuation coefficient, absorption coefficient, and scattering coefficient from [2]

Water type	$c(\lambda)$	$a(\lambda)$	$b(\lambda)$
Pure seawater	0.043	0.041	0.003
Clear ocean	0.151	0.114	0.037
Coastal ocean	0.298	0.179	0.219
Turbid harbor	2.190	0.266	1.824

Thus, considering all the coefficient models presented above, the corresponding

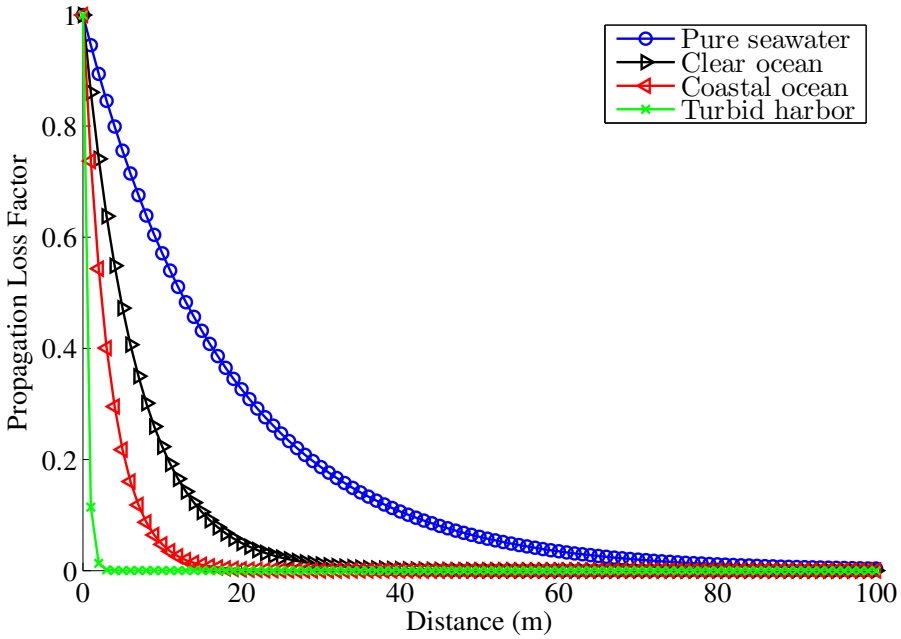

Figure 2.8: Attenuation of the optical signal (propagation loss factor) considering the values of Table 2.2.

attenuation of the optical signal can be described as [9]

$$I = I_0 \mathrm{e}^{-c(\lambda)d}, \tag{2.10}$$

where I is the light intensity at the receiver, I_0 is the light intensity at the transmitter and d is the distance between transmitter and receiver. We can define

$$L(\lambda, d) = \mathrm{e}^{-c(\lambda)d} \tag{2.11}$$

as the propagation loss factor that is shown in Figures 2.8 and 2.9 for the coefficient values of Tables 2.2 and 2.3 respectively. As observed, the more limpid water results in the lower attenuation for the optical signal. For turbid harbor waters, the signal is rapidly attenuated, meaning that the signal propagation distance is severely reduced when comparing with pure seawater.

Noise in Underwater Optical Communications

The main noise types impairing underwater optical transmissions are [3, 22]: excess noise, quantum shot noise, optical excess noise, optical background noise, photodetector dark current noise, and electronic noise.

- Excess noise is generated in the process of amplifying the signal at the receiver. Such procedure is performed for dealing with thermal noise;
- Quantum shot noise occurs due to random variations of the number of photons;

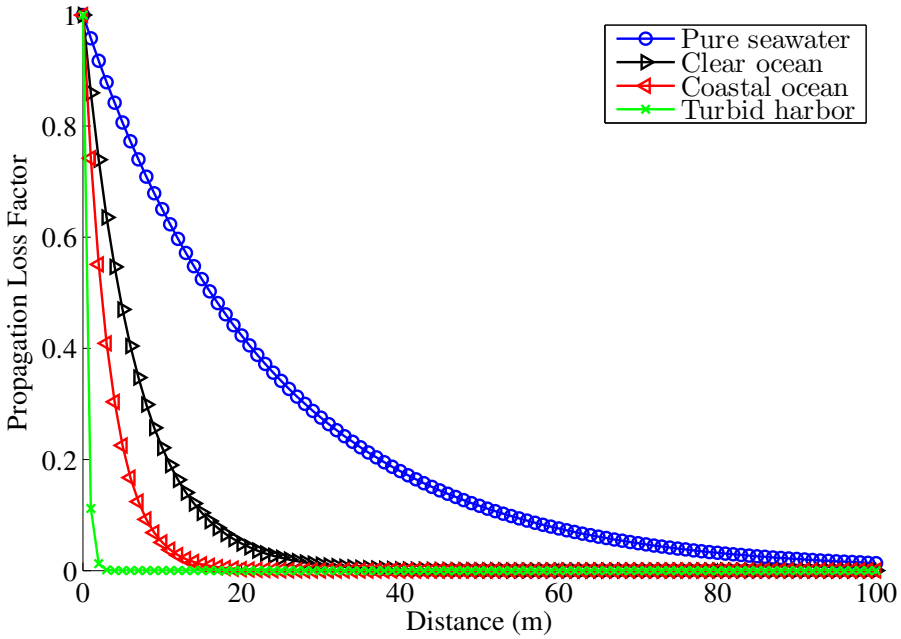

Figure 2.9: Attenuation of the optical signal (propagation loss factor) considering the values of Table 2.3.

- Optical excess noise is caused by transmitter imperfections;
- Optical background noise occurs due to environmental optical clutter;
- Photo-detector dark current noise is caused by electrical current leakage from photo-detector;
- Electronic noise comes from electronic components whose main sub-types are: thermal noise, electronic shot noise, pink or $1/F$ noise, and preamplifier noise.

Optical Transducers

Transducers for underwater optical communications have different requirements depending on whether they are working as sensors at the receiver end or as actuators at the transmitter end. Transducers designed for generating optical signals from electrical signals are composed of optical source, projection optical system, and beam steering, whereas transducers for sensing optical signals and converting them to electrical signals are composed of collection optics and detector.

1. Transmitter Part

   The optical source can be either a laser (light amplification by stimulated emission of radiation) or a LED (light-emitting diode). In the case of laser sources, there are different technologies that have specific applications depending on the corresponding system requirements. One technology is argon-ion lasers,

in which the electrical to optical conversion is extremely inefficient [3]. Other technologies include the diode-pumped solid-state (DPSS) lasers, the InGaN lasers, whose devices are a hundred times more expensive than LEDs [3] and are susceptible to over-current problems, and the tunable lasers which can adapt the frequency of emission in order to have lower wave propagation attenuation according to the particular environment characteristics. Another technology is the laser modulators, whose data rates are extremely low (in the order of Hz or kHz) and the propagation range is relatively longer (in the order of hundreds of meters) [3]. On the other hand, LEDs are cheaper optical sources, when compared to lasers, but they have lower propagation range [9].

The function of projection optics is to focus the beam towards a predefined direction, which presumably contains the receiver end. The beam steering is fundamental to the optical system performance. Indeed, transmitter and receiver have to establish line-of-sight so that the optical signals that arrive at the receiver end have enough energy to be reliably decoded. Smart transmitters are able to estimate the water quality through the backscattered signal [9]. With this knowledge, the transmitter can adapt the transmission power accordingly, thus improving the overall transmission process.

2. Receiver Part

   Transducers designed to act as receivers are composed of collection optics and detector. The collection optics can be a single or an array of lenses, whose main role is to gather the transmitted rays. The detector is a photosensor, whose main role is to convert the optical signal into an electrical signal. The objective of the transducer at the reception end is to collect the maximum amount of photons that were transmitted. In order to improve the system performance, some relevant characteristics of the collection optics and of the detector have to be analyzed and considered in the system design.

   One characteristic is the aperture size of the photosensor. It is desirable to have a sensor with large aperture size. One photosensor with this characteristic is the photomultiplier tube (PMT). These sensors can be expensive and bulky [9] which is a disadvantage for some applications. Another alternative for increasing the aperture size is to use an array of lenses in front of the small collection area photosensor.

   An ideal photosensor is cheap, small, robust and power efficient [23], however, these requirements cannot be fulfilled simultaneously in the current technology state [23]. According to the system specifications, a particular type of photosensor must be chosen. The main photosensor types are: Photoresistors,

Photothyristors, Phototransistors, Photomultiplier Tube (PMT), p-n Photodiodes, Avalanche Photodiode (APD), Photon Detector Selection, Semiconductor Photosensors, and Biologically-inspired Quantum Photosensors (BQP). Details of each type can be found in [23], [3], and [19].

In order to improve system performance, the concepts of smart transmitter and receiver are introduced in [9]. The smart receiver should be quasi-omnidirectional, and the smart transmitter should have a higher directionality and an electronic switched light beam direction. At the receiver end, this can be achieved combining a lenses array with a photodiode array and/or combining the outputs of the photodiodes for improving the received signal [9].

2.2.3 Main Concerns in Optical Communications

The main drawback related to optical communications is the dependence on water turbidity. This environmental condition constrains the propagation distance, meaning that the propagation distance achievable when using optical technology may not be sufficient for some applications.

2.3 Underwater Acoustics Communications

Despite requiring rather sophisticated modeling, the acoustics propagation in the ocean meets no competition for long distance propagation when compared to electromagnetic waves. The acoustics signal suffers little attenuation at low frequencies, and despite its increasing attenuation at higher frequencies, it can reach higher distance than other alternative technologies.

2.3.1 Acoustics Communication Overview

When dealing with acoustic-based communications, the first parameter that should be taken into account in order to understand the overall communication process is the speed of propagation of sound waves. Indeed, it is well-known that the speed of propagation of waveforms in any communication system is finite and depends on the electromagnetic or mechanical properties of the channel. Electromagnetic waves usually propagate at speeds close to the speed of light at vacuum, which is around 4 to 5 orders of magnitude larger than the speed of propagation of acoustic waves in fluids. This imposes tremendous constraints on the overall transmission process through sound waves, therefore the parameters affecting the speed of propagation play a major role in acoustic communications underwater.

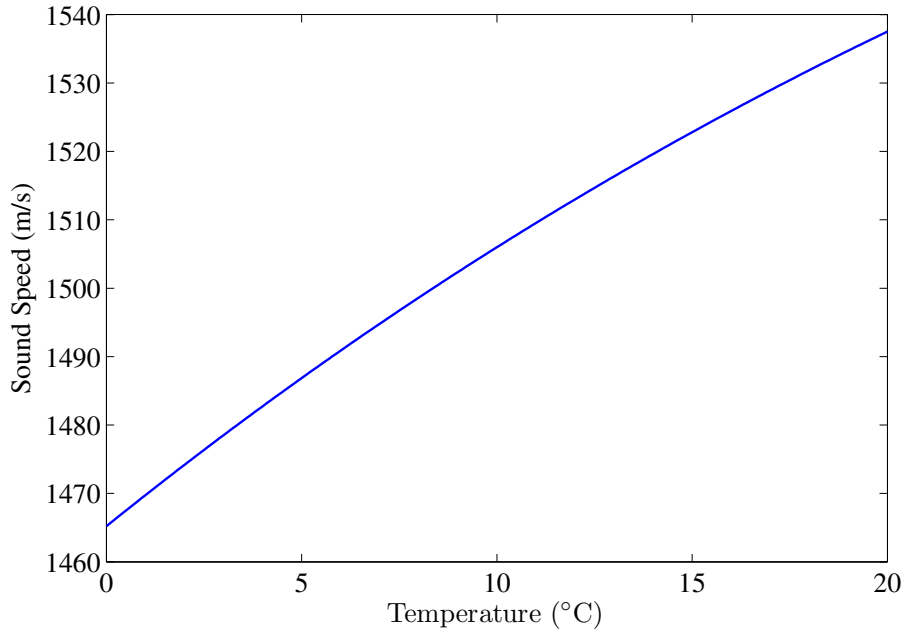

Figure 2.10: Sound speed *versus* temperature for $S = 35$ ppt, $z = 1000$ m.

The speed of propagation of acoustic waves in underwater environments, denoted as c (in meters per second), depends on several sea conditions, as described by the following relation [24]:

$$c = 1449.2 + 4.6T - 0.055T^2 + 0.00029T^3 + (1.34 - 0.01T)(S - 35) + 0.016z, \tag{2.12}$$

in which T is the temperature (in degrees Celsius), S is the salinity (in ppt — parts per thousand), and z is the water depth (in meters). For example, the speed of sound is $c = 1482.7$ m/s, considering a salinity $S = 35$ ppt, for a water temperature $T = 4\,^{\circ}\text{C}$, and assuming an ocean depth $z = 1000$ m. This value of salinity is typical for open oceans, although the salinity can be as low as $S = 8$ ppt in the Baltic sea. Figures 2.10, 2.11, 2.12 show the variability of the speed of propagation as a function of temperature, salinity and depth, respectively. It is possible to observe that the propagation speed is always an increasing function of temperature, salinity and depth when two of these parameters are fixed. For all these cases, the speed of the acoustic wave has always the same order of magnitude.

Signal propagation is another relevant issue in underwater acoustic communication. Multiple delayed and distorted versions of the transmitted signal arrive at the receiver due to the multipath channel, as shown in Figure 2.13. These phenomena generate distortions in the signal such as intersymbol-interference (ISI), which must be compensated by the transceiver. As a consequence, knowledge of the channel model might enable the design of more efficient transceivers [5, 25, 26], leading to a

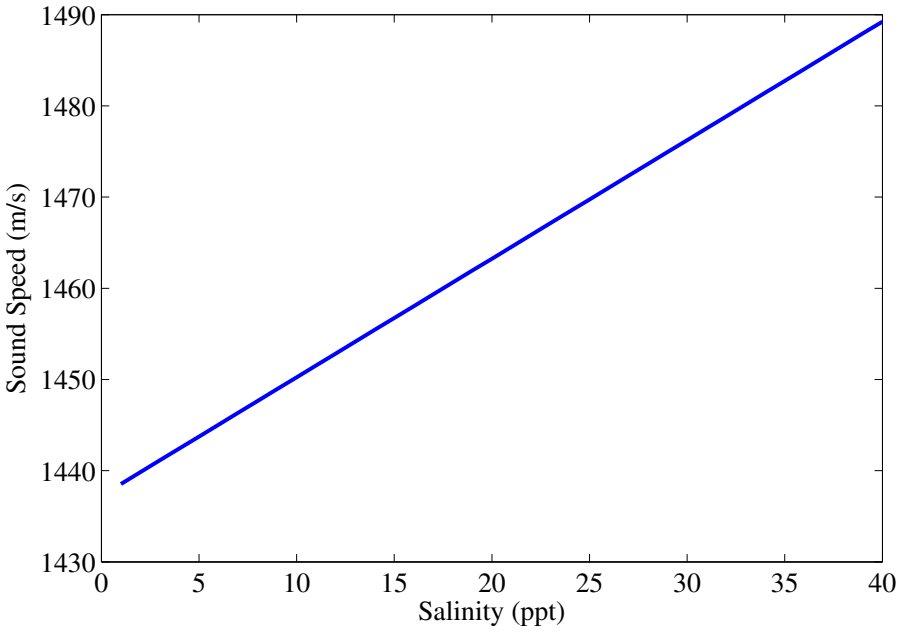

Figure 2.11: Sound speed *versus* salinity for $T = 4\,^{\circ}\mathrm{C}$, $z = 1000$ m.

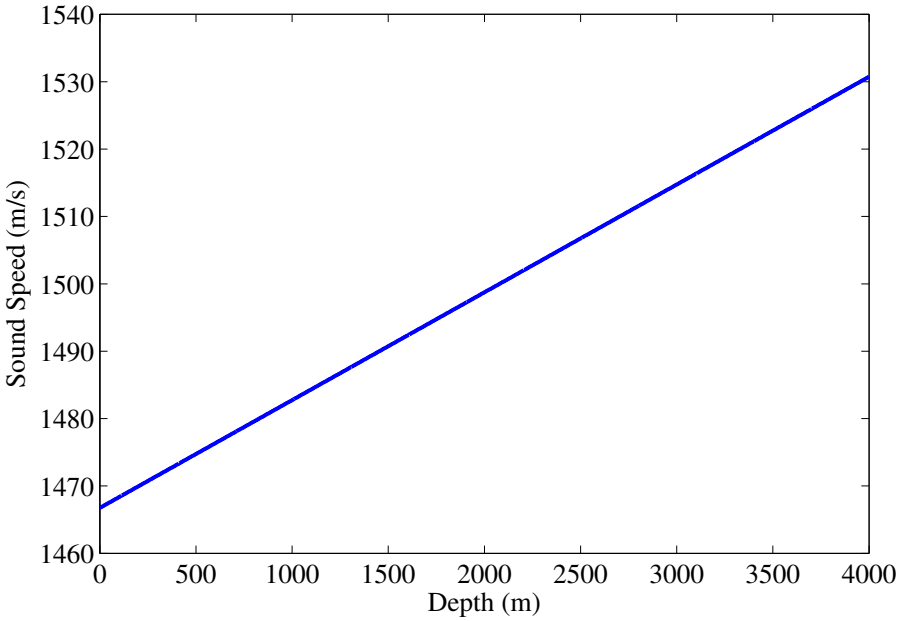

Figure 2.12: Sound speed *versus* depth for $S = 35$ ppt, $T = 4\,^{\circ}\mathrm{C}$.

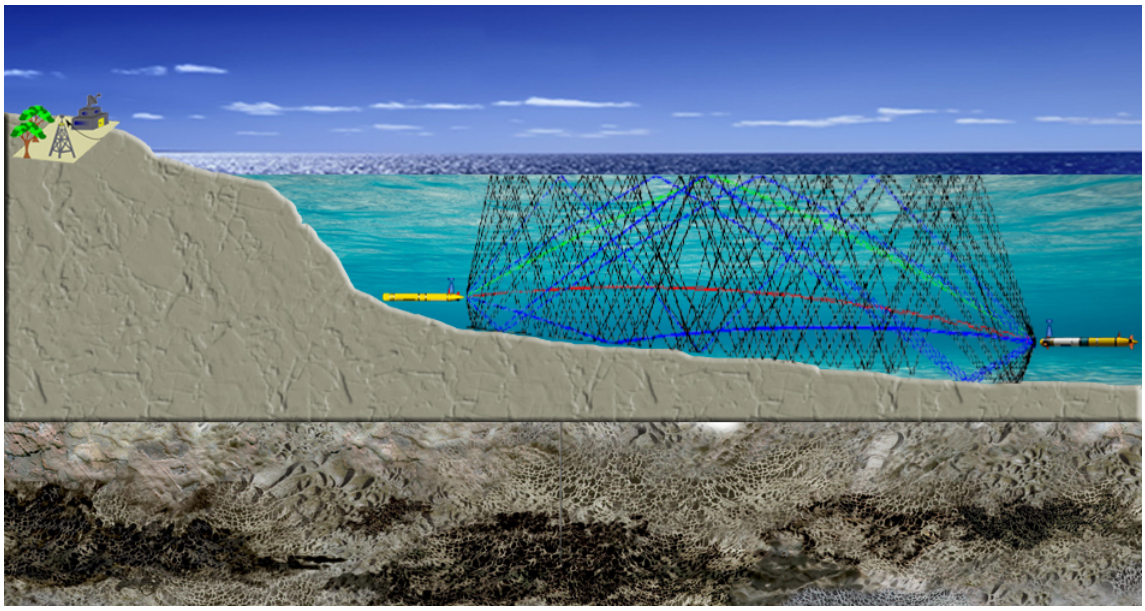

Figure 2.13: Example of a communication in shallow water environment. Multiple delayed and distorted versions of the transmitted signal arrives at the receiver-end.

communication with improved data rate. Thus, a current concern is the characterization of the underwater acoustic channel [27–29], as well as its capacity [30, 31].

The acoustic waves propagate facing frequency-dependent attenuation and delay, and this fact plays a central role in the design of traditional wireless communication systems. Determining the attenuation behavior as a function of frequency is quite desirable for a system designer, since it gives technical support for choosing the frequency bands to be employed in the communication. The acoustic signal suffers little attenuation at low frequencies, and increasing attenuation at higher frequencies. Nonetheless, low frequency ranges and low speed of propagation are two major issues that might hinder high-throughput undersea communications. Indeed, low bandwidth imposes a constraint on the amount of bits that can be transmitted in each channel utilization, whereas the low speed of propagation increases the round-trip time and amplifies Doppler effect.

Taking into consideration the propagation properties, from a signal processing viewpoint, a given snapshot of the underwater channel could be characterized by its channel-impulse response. The channel transfer function might have non-minimum phase [32], thus implying that the inverse system is not stable. Such fact, eventually, can turn the equalization process harder to implement. Some well-known equalization techniques applied for underwater acoustics are MMSE-based DFEs (minimum mean-squared error-based decision-feedback equalizers) [33], adaptive turbo equalizers [34], and TRM (time reversal mirror) [35, 36]. Another common problem occurs when the receiver is at a shadow zone, so that the received signals are relatively weak, causing loss of connection [32]. Other phenomena that yield variation in the

sound propagation are tides, currents, and internal waves [37].

Furthermore, as for RF and optical technologies, it is common to classify acoustic communications considering the underwater environments. The underwater environment is classified as shallow water and deep water, whereas each water type possesses two distinct definitions [38]: hypsometric and acoustic. In the hypsometric definition, shallow water is located in the continental shelf, in which the water column depth is mainly lower than 200 meters. Generally the sea bottom on the border of the continental shelf falls off rapidly into deep water, in which the water column has more than $2,000$ m depth. The shallow water classification in acoustic definition considers that the acoustic waves reflect at the sea floor and at the sea surface before they are detected at the receiver, whereas in deep water, the wave does not necessarily reflect at the sea bottom.

2.3.2 Fading Sources of Acoustics Waves

In this section, the main phenomena that contribute to the fading of acoustic waves are described, and their respective models are presented. The three main fading sources are spreading loss, absorption loss, and scattering loss [32].

The spreading loss is the expansion of a finite amount of energy that is transmitted by an omnidirectional point source and that propagates over a large surface area [32]. Depending on range of distances, the surface is modeled either as a sphere or as a cylinder. For long ranges, the spread loss is modeled as cylindrical since the range of propagation is bounded by the sea floor and by the sea surface.

The absorption loss is the conversion of part of the transmitted energy of the acoustic wave into heat. The higher is the frequency, the larger is the absorption loss. Similarly, a longer propagation distance leads to higher absorption loss [39].

Scattering is the modification of acoustic wave propagation due to obstacles. These obstacles can be sea surface, sea floor, objects in the water, just to mention a few examples. The bubbles also absorb the acoustic energy. Usually, the bubbles near the sea surface result from breaking waves caused by winds or by the waves generated by moving ships (ships' wake), whereas in deep layers they stem from biological organisms [24, 40].

As stated before, scattering can be modelled in different ways, depending on the obstacle type. In order to illustrate this dependence, the model of two specific types of scattering are shown. The first case models the scattering strength in the sea surface (γ_{S}) [24] and is given by

$$\gamma_{\mathrm{S}} = 3.3\beta \ \log\left(\frac{\theta}{30}\right) - 42.4\log(\beta) + 2.6, \tag{2.13}$$

in which β is given as

$$\beta = 107(wf^{1/3})^{-0.58}, \tag{2.14}$$

where γ_{S} is in dB, w is the wind speed in m/s, f is the frequency in Hz and θ is the grazing angle[1] in degrees. This model is valid for wind speeds below 15 m/s and for the frequency range 400-6400 Hz.

The second model of scattering is related to the sea floor. This surface not only scatters the signal, but also absorbs the signal. The model of the signal that is backscattered, i.e., the signal returning to the transmitter, is given by

$$\gamma_{\mathrm{B}} = -5 + 10\log(\sin^2(\theta)) \tag{2.15}$$

with γ_{B} being the backscattering strength in dB.

The aforementioned spreading loss and absorption loss phenomena contribute to the path loss, whose simplified model is expressed in dB as [6, 39, 41, 42]:

$$10\,\log A(l,f) = \underbrace{10\,\log A_0}_{\mathrm{NF}} + 10\,k\,\log l + l\,\underbrace{10\,\log a(f,S,T,c,pH,z)}_{\alpha(f,S,T,c,pH,z)} \tag{2.16}$$

where l is the distance (in meters) between transmitter and receiver, f is the frequency (in kHz), k is the spreading factor, whose commonly employed values are: 1 for cylindrical spreading, 2 for spherical spreading, and 1.5 for "practical spreading" [39]. The parameter $\mathrm{NF} = 10\,\log A_0$ is a normalization factor that can be related to the inverse of the transmitted power. The variable $\alpha(f,S,T,c,pH,z)$ represents the attenuation coefficient (in dB/m). Typically, for shallow water, the spreading is considered to be cylindrical, whereas for deep water, the spreading is considered to be spherical at positions relatively near to the transmitter.

The attenuation coefficient depends on environmental conditions in the following way [42]

$$\alpha(f,S,T,c,pH,z) = \frac{A_1P_1f_1f^2}{f^2+f_1^2} + \frac{A_2P_2f_2f^2}{f^2+f_2^2} + A_3P_3f^2 \tag{2.17}$$

where f is the frequency in kHz and

$$f_1 = 2.8\left(\frac{S}{35}\right)^{0.5} \times 10^{4-\frac{1245}{273+T}}$$

[1]Grazing angle is the angle between the beam and the surface.

where S is the salinity measured in ppt, T is the temperature in degree Celsius and

$$f_2 = \frac{8.17 \times 10^{8-\frac{1990}{273+T}}}{1 + 0.0018(S-35)},$$
$$A_1 = \frac{8.68}{c} 10^{0.78\text{pH}-5}$$

where c is the propagation speed of the acoustic wave, pH represents the potential of hydrogen of water and

$$P_1 = 1$$
$$A_2 = 21.44\frac{S}{c}(1 + 0.025T)$$
$$P_2 = 1 - 1.37 \times 10^{-4} z + 6.2 \times 10^{-9} z^2$$

where z is the water depth, and

$$P_3 = 1 - 3.83 \times 10^{-5} z + 4.9 \times 10^{-10} z^2$$
$$A_3 = \begin{cases} 4.937 \times 10^{-4} - 2.59 \times 10^{-5} T + 9.11 \times 10^{-7} T^2 - 1.5 \times 10^{-8} T^3 & \text{for } T \leq 20 \\ 3.964 \times 10^{-4} - 1.146 \times 10^{-5} T + 1.45 \times 10^{-7} T^2 - 6.5 \times 10^{-10} T^3 & \text{for } T > 20 \end{cases}$$

As seen before, the path loss depends on several factors such as frequency and distance between transmitter and receiver. This dependence can be seen in Figures 2.14, 2.16, 2.15, 2.17 for shallow and deep water respectively. For computing the path losses, the factor NF was considered to be zero and the spreading factor of $k = 1$ for shallow water and $k = 2$ for deep water. For a fixed distance, there is a minimum loss value that is related to the spreading loss and the attenuation factor ($l\,\alpha(f)$) dominates in higher frequencies. From these figures, we observe that for low frequencies, the path loss is around the same for different distances. The path loss increases considerably when the frequency and the distance between transmitter and receiver increases. This behavior can be observed in Figures 2.18 and 2.19, where the dependence of the path loss with respect to the distance and frequency is clear.

It appears that at the same frequency and the same distance, signals propagating in deep water always have a lower attenuation than signals propagating in shallow water. This behavior is confirmed in Figures 2.18 and 2.19.

A simplified expression of the attenuation coefficient, known as Thorp's formula is [24]

$$\alpha(f) = 3.3 \times 10^{-3} + \frac{0.11 f^2}{1 + f^2} + \frac{44 f^2}{4100 + f^2} + 3.0 \times 10^{-4} f^2 \text{ [dB/km]}, \tag{2.18}$$

where f is the frequency of a time-harmonic signal expressed in kHz, and this formula

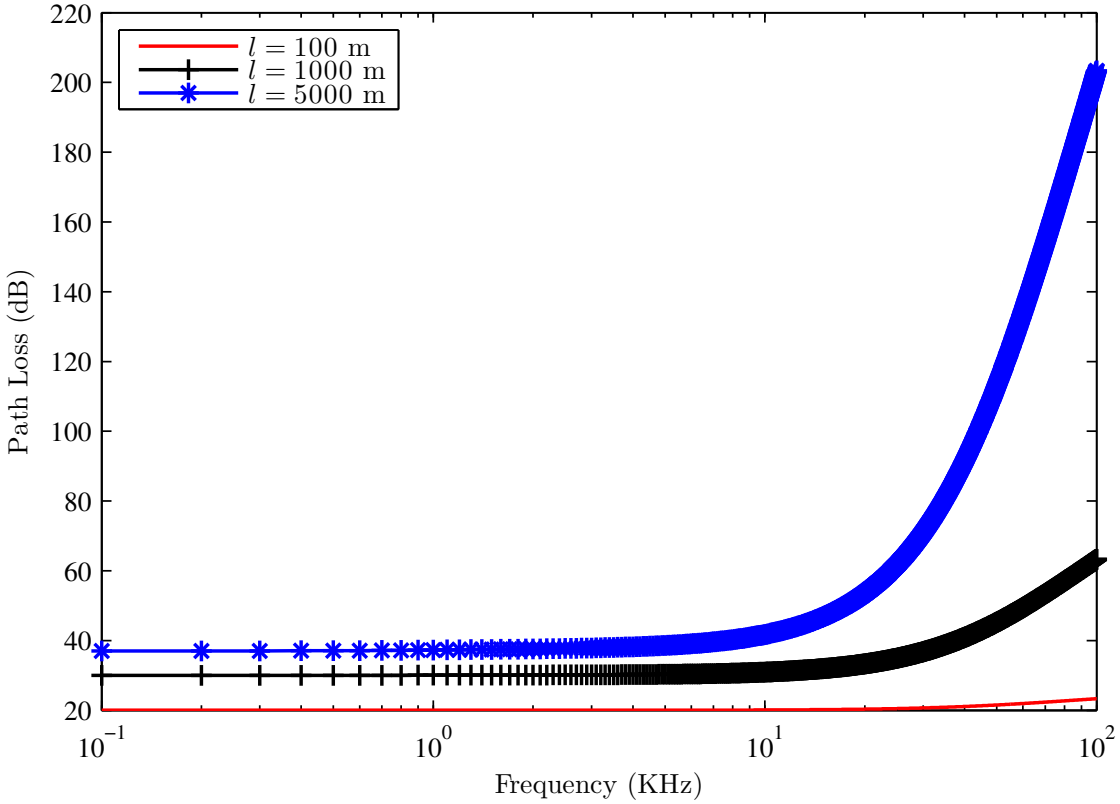

Figure 2.14: Shallow water — Path loss *versus* frequency for temperature 10°C, salinity 35 ppt, ocean depth 60 m, and pH = 8.

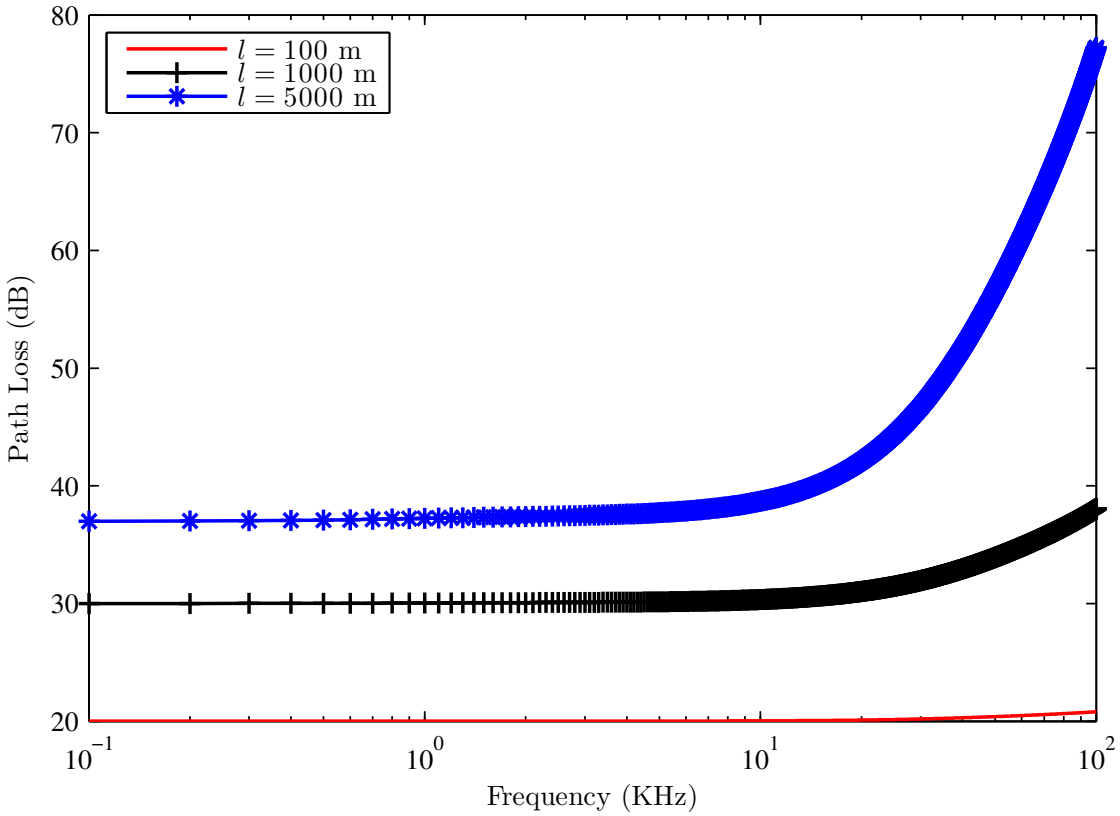

Figure 2.15: Deep water — Path loss *versus* frequency for temperature 4°C, salinity 35 ppt, ocean depth 10000 m, and pH = 8.

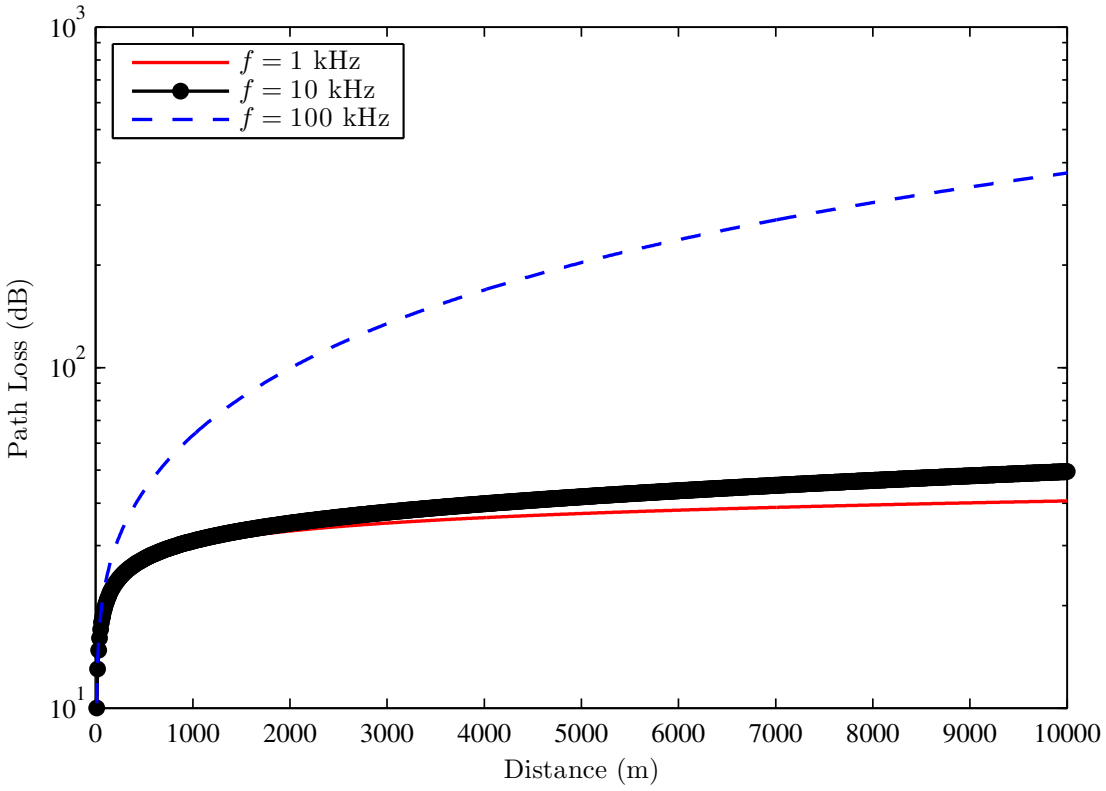

Figure 2.16: Shallow water — Path loss *versus* distance for temperature 10°C, salinity 35 ppt, ocean depth 60 m, and pH = 8.

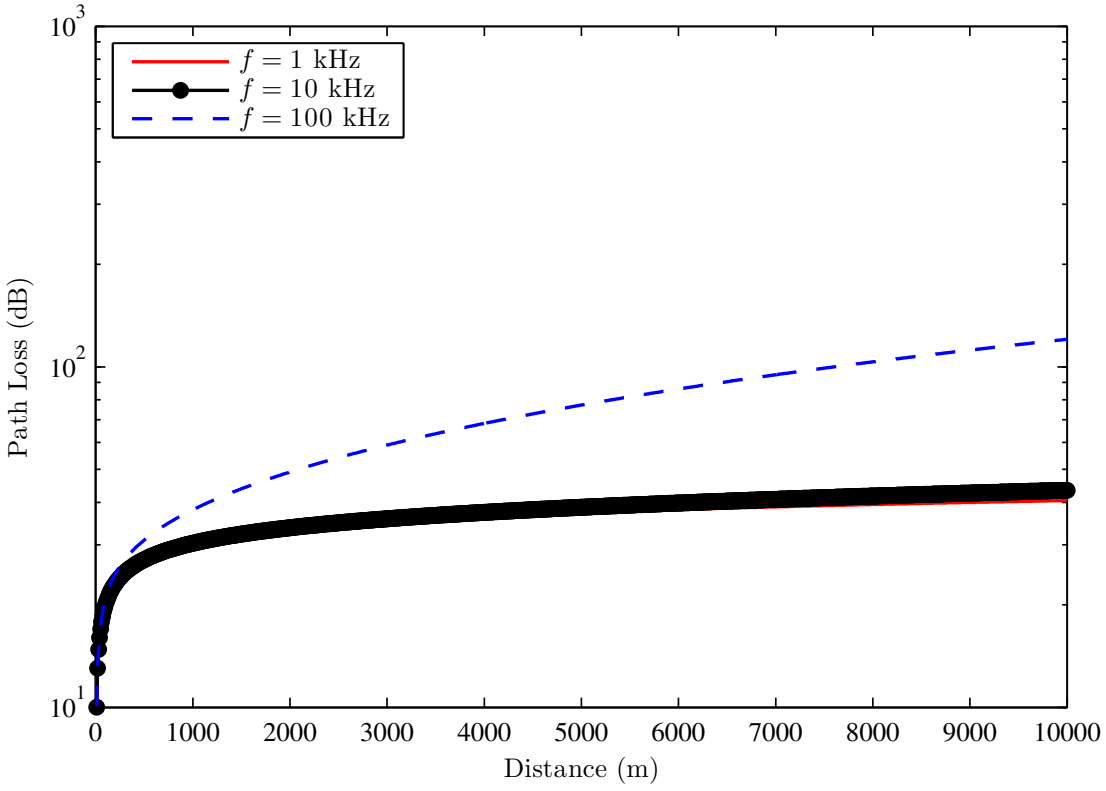

Figure 2.17: Deep water — Path loss *versus* distance for temperature 4°C, salinity 35 ppt, ocean depth 10000 m, and pH = 8.

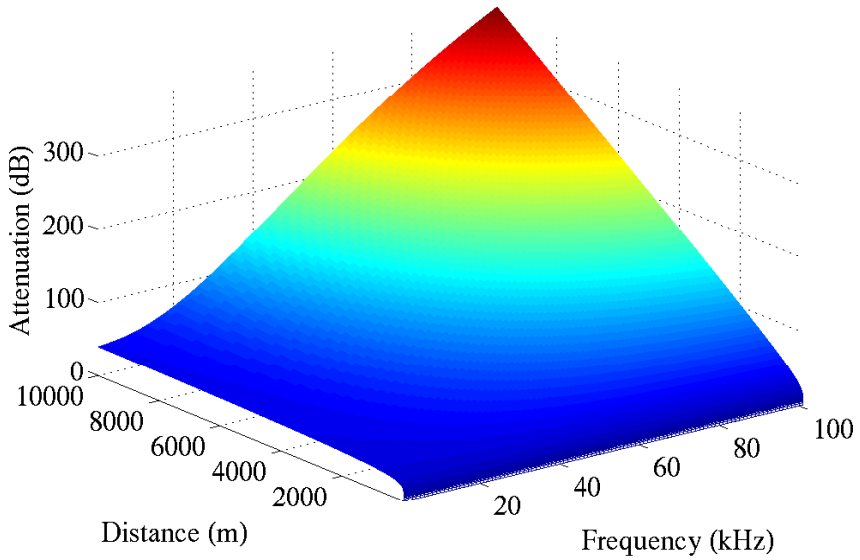

Figure 2.18: Shallow water — Path loss *versus* distance *versus* frequency for temperature 10°C, salinity 35 ppt, ocean depth 60 m, and pH = 8.

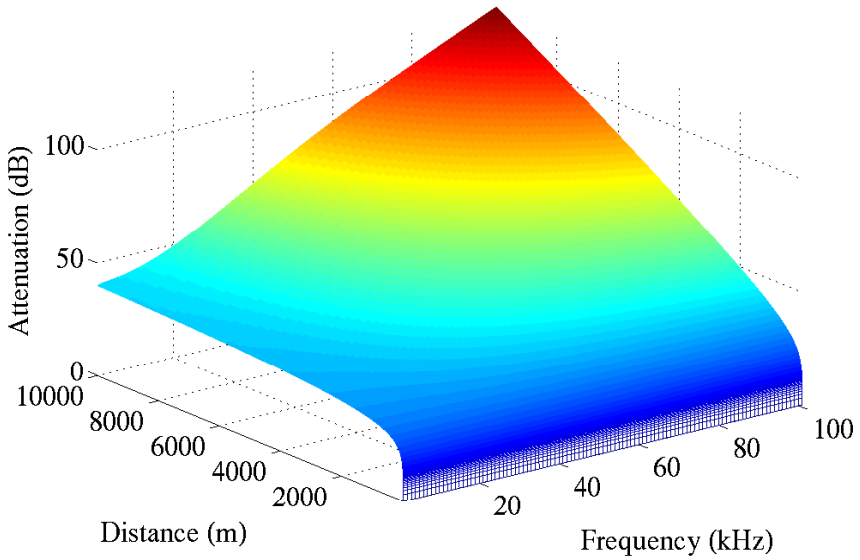

Figure 2.19: Deep water — Path loss *versus* distance *versus* frequency for temperature 4°C, salinity 35 ppt, ocean depth 10000 m, and pH = 8.

is accurate only for a temperature of 4°C, a salinity of 35 ppt, and ocean depth of around 1000 m.

A possible multipath model for the acoustics environment has the channel coefficients related to the path loss as

$$h_m(t) = \frac{\delta(t)}{\sqrt{A(l_m, f)\gamma_m}}. \tag{2.19}$$

The coefficient γ_m accounts for additional transmission losses, such as reflection and scattering losses, faced by the m-th multipath. It should be noticed that in this case $h_m(t)$ is not in dB. The frequency dependent function $A(l_m, f)$ represents the path loss of the m-th multipath.

Noise Model

Another important issue for the channel model is the ambient noise that interferes with the signal when it is passing through the channel. In [39], [40] four different types of noise presented in underwater acoustics environment are described; each type is more influential in a different range of frequencies:

- $f < 10$ Hz: the dominant noise for this range is related to earthquakes, turbulences in the ocean and in the atmosphere, distant storms, and vulcan eruptions underwater [40]. The power spectral density (PSD) in dB re μ Pa per Hz is formulated as [39]

$$10 \log N_{\mathrm{t}}(f) = 17 - 30 \log f \tag{2.20}$$

  where f is the frequency in kHz,

- $10 < f < 100$ Hz:[2] the main noise source is the traffic of distant shipping and its PSD is modeled as [39]

$$10 \log N_{\mathrm{s}}(f) = 40 + 20(s - 0.5) + 26 \log f - 60 \log(f + 0.03) \tag{2.21}$$

  with s being the factor of shipping activity

- 100 Hz $< f <$ 100 kHz:[3] this noise is originated from the state of the sea surface and of the wind speed (w in m/s) [39]

$$10 \log N_{\mathrm{w}}(f) = 50 + 7.5 w^{\frac{1}{2}} + 20 \log f - 40 \log(f + 0.4) \tag{2.22}$$

[2] In [40] the range $50 < f < 300$ Hz is considered, while in [39] is considered the range $10 < f <$ 100 Hz.

[3] In [40] the range 500 Hz $< f <$ 50 kHz is considered, while in [39] is considered the range 100 Hz $< f <$ 100 kHz.

- $f > 100$ kHz: thermal noise is the main source in this frequency range and the PSD is [39]

$$10 \log N_{\text{th}}(f) = -15 + 20 \log f. \tag{2.23}$$

  Notice that the thermal noise described by Eq. (2.23) is from underwater environment, therefore being distinct from the thermal noise caused by electronic components of the receiver device.

Acoustics Transducers

Acoustic transducers convert electrical signals into sound (transmitter) or sound into electrical signals (receiver). The transmitters are called sources or projectors and the receivers are called hydrophones. However, commonly a single transducer acts as a transmitter and as a receiver in an acoustic modem. These devices are designed for underwater environments and can be attached to floating objects (e.g. boat or buoy) or can be moored.

Generally the sources or projectors work in particular frequency bands, that are generally narrower than the hydrophone frequency band. Projectors can be omnidirectional or hemispherical, whereas hydrophones can be omnidirectional or directional. Several omnidirectional hydrophones can compose an array, so that when the acquired signals are properly combined, it is possible to select a preferential receiving direction, or to use diversity for improving system performance.

The most common types of transducers are the piezoelectric and magnetostrictive [24]. There are also other types, e.g., parametric or finite-amplitude sources and receivers, but a discussion on those falls beyond our concern.

2.3.3 Main Concerns in Acoustic Communications

Most acoustic communication links demand the mitigation of the Doppler effects, that might utilize fast learning and tracking adaptive algorithms such as Kalman filters. The dispersive characteristics of the acoustic channel model is another important issue to guarantee successful equalization and synchronization. The use of multicarrier transceivers is also possible as a solution to channel estimation but the high Doppler effect in the acoustic communication case affects subchannel orthogonality of the subcarriers. The propagation delay of the acoustic signal in the water places additional constraints on the signal processing solution utilized in these systems; a typical example is the challenge of deploying relay sensor networks.

The relative velocity between transmitter and receiver ends, and the underwater dynamical environment cause the Doppler phenomenon. Although also present in radio-frequency communication, Doppler effect is particularly noticeable when

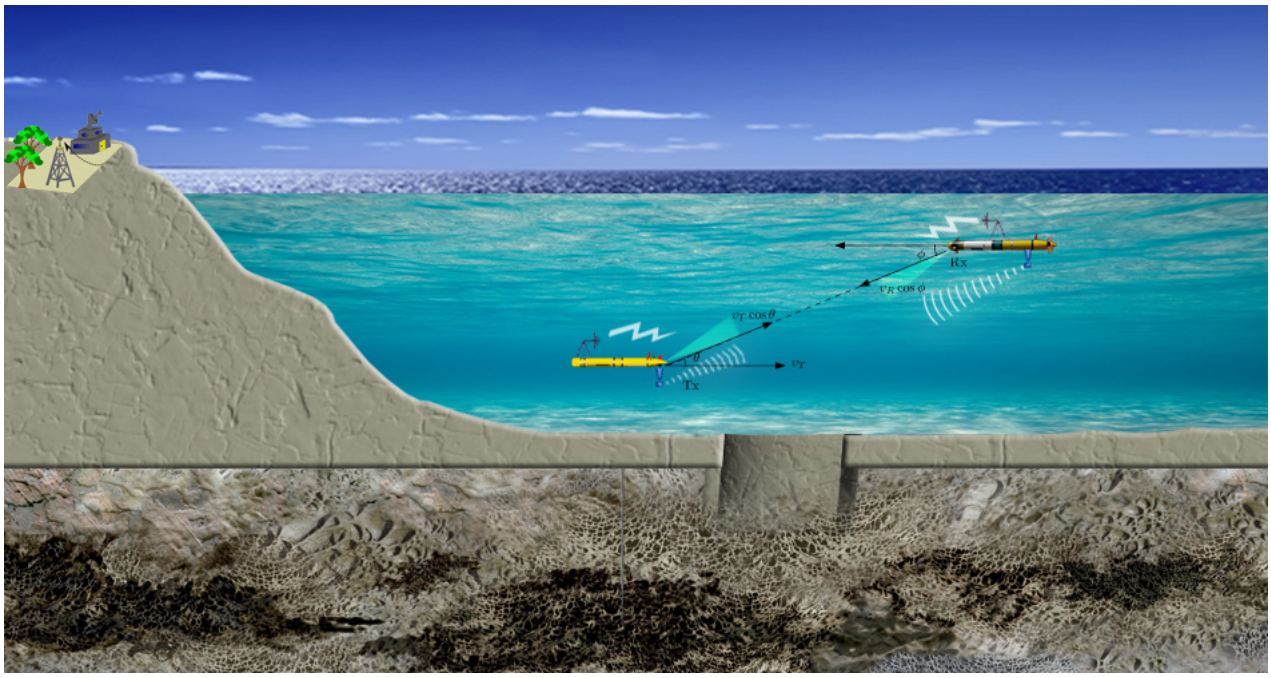

Figure 2.20: Transmitter and receiver moving with respect to the propagation medium.

communicating using pressure waves, due to the relatively low speed of propagation of the wavefront. The effect is even more pronounced for underwater acoustic communication, since in this case, buoys and vessels which host transmitter and receiver are seldom at absolute rest. Therefore, Doppler distortion is hard to ignore, and mitigating its effect is of paramount importance for an efficient communication system.

The Doppler effect produces a time warping effect on the transmitted signal. In addition to the expansion or contraction of the signal duration, the time warping effect also distorts the signal phase. Time warping can be seen as a modification of the time index from t to $\bar{t} = [t + \rho(t)]$, where $\rho(t)$ can be approximated by $(v_R \cos\phi + v_T \cos\theta)/c$, in which v_R, v_T are the receiver and the transmitter speeds, respectively, and the angles ϕ and θ are shown in Figure 2.20. The reader should keep in mind that speeds and angles are expected to vary with time, therefore $\rho(t)$ holds explicitly its time dependence. Once the Doppler factor $\rho(t)$ is estimated, this effect may be compensated by a proper adjustment of the sampling frequency, followed by a signal phase correction [43]. Although, a residual distortion may remain, which is usually treated in the channel estimation procedure. Therefore, any Doppler estimation scheme implemented must be robust and resilient. In order to address this issue, new approaches for estimating and compensating Doppler effect have been studied in [44–57]. Nonetheless, there is no consensus about the optimal way to tackle this problem.

Another concerning issue in underwater acoustic communications is related to

the channel impulse response. As the speed of propagation of acoustic waves is lower than the speed of propagation of electromagnetic waves in the air, the coherence time of the acoustic channel is smaller than the aerial RF channel. Indeed, a channel possessing a higher delay spread might require a receiver with higher computational complexity, due to the augmented number of variables. A possible approach to avoid this complexity increment is to employ the knowledge that the acoustic channel is intrinsically sparse. So, a great number of researches exploit this property for estimating the channel: [47, 58–63].

The channel equalization is another big issue in underwater acoustic communication. Those channel features mentioned above may introduce severe ISI and inter-carrier interference (ICI) in the received signal. So, the equalizer should be capable of removing and compensating these distortions. Some techniques like MMSE-based DFEs [33], TRM [35, 36, 64] and turbo equalizers [34, 65–68] have been extensively studied in the literature.

2.4 Technology Comparison

Before concluding which technology should be the best to transport information, one must know in which environmental conditions the system has to operate, as well as what are the communication requirements. Table 2.4 summarizes the main features and drawbacks inherent to each technology that might help approach a proper solution. This table compares the water properties that mostly affect each transmission technique: salinity for RF, water turbidity for optical, and water depth for acoustic. Each technology is mainly affected by distinct water features, as described in Table 2.4. The interested reader can refer to [69–76] for further information regarding achievable data rates for different technologies and parameters.

In addition, to achieve robust and reliable underwater communications, the challenge is to propose flexible communication systems including all the aforementioned communication technologies. This flexible system could be intelligent so that the maximum transmission rate could be achieved considering, for instance, environmental conditions, distance, and relative movement between transmitter and receiver. Such heterogeneous system would be able to switch technology of transmission/reception according to a predefined cost function: the receiver would send from time to time an acknowledgment signal to the transmitter that would take the appropriate action. Furthermore, since all underwater communication systems have inherent limitations with respect to connections over long distances, the use of networks including several sensors and relays, with the aid of smart protocols, seems to be necessary. The network nodes could be fixed or mobile, and all nodes should ideally be able to transmit and/or receive with the three technologies [76]. The

mobile nodes should be smart enough such that moving to a nearby position would result in improved communication by optimizing an appropriate cost function.

Table 2.4: Wireless underwater technologies: RF, optical and acoustic

	Technology		
Main issues	**RF**	**Optical**	**Acoustics**
Key water property	Salinity	Water turbidity	Water depth
Water types	Fresh water × Seawater	• Main Jerlov water types: Clearest water, Intermediate water, Murkiest water • From [1], [2]: Pure seawater, Clear ocean water, Coastal ocean water, Turbid harbor and estuary water	Shallow water × Deep water
Drawbacks and/or requirements	High attenuation over short distances	• Line of sight link • Receiver direction tracking • Subject to marine fouling	• Doppler estimation and compensation • Latency in communication • Existence of shadow zones
Main characteristics	Can cross water/air surface (boundary)	Achieve higher data rates	Propagates over longer distances
Reliable communication distance	Few meters	Tens of meters	Kilometers
Achievable data rates	1 to 10 Mbps (@$1-2$ m, [7]) 50 to 100 bps (@200 m, [7])	1 Gbps (@2 m, [18]) 1 Mbps (@25 m, [75])	1.5 to 50 kbps (@0.5 km, [77]) 0.6 to 3.0 kbps (@$28-120$ km, [78])
Dependence of the speed propagation	Frequency, water conductivity (salinity and temperature)	Frequency, water turbidity (chlorophyll concentration, salt ions, etc.)	Temperature, salinity, water depth

Despite all these extensive research, we are going to study further specific issues related to acoustics technology. Our motivation in choosing underwater acoustics communications lies on its wide usage and on the possibility of testing our ideas with

practical experiments. Our aim is to solve problems related to the Doppler effect in order to have a reliable communication, and therefore improve system throughput. In the following chapters we show a study concerning the acoustic channel in a specific location, and how the Doppler spread affects the system performance.

Chapter 3

System Model and Underwater Acoustic Channel Assessment

This chapter presents and describes the block transceiver setup along with the physical channel model considered in this thesis. This chapter also shows an example of an underwater acoustic channel using data collected in the coast of Arraial do Cabo.

We start this chapter describing the system model employed in this thesis in Section 3.1. Subsection 3.1.1 presents some possible transmitter configurations along with their respective mathematical models. In Subsection 3.1.2, a mathematical model for the channel impulse response is shown, and the relationship of some channel parameters with Doppler effect is discussed. Subsection 3.1.3 presents some signal processing techniques performed at the receiver side.

In Section 3.2, we assess the channel frequency response of Arraial do Cabo. An analysis considering some channel features using a ray tracing program is performed. In the same section, we show the obtained results and our conclusions concerning this work. Section 3.3 presents the chapter summary.

3.1 Communication Model

The overall communication setup considered in this thesis is depicted in Figure 3.1. Depending on the choice of the transmitter matrix $\bar{\boldsymbol{F}}$, this block diagram represents either single carrier or multicarrier systems. For both cases, the transceivers redundancy may vary between the minimum case, i.e., half of the channel with even order[1], and the full case, in which the redundancy amount is equal to the channel order.

[1] Or $\lceil L/2 \rceil$, where L is the channel order, and $L+1$ is the channel length.

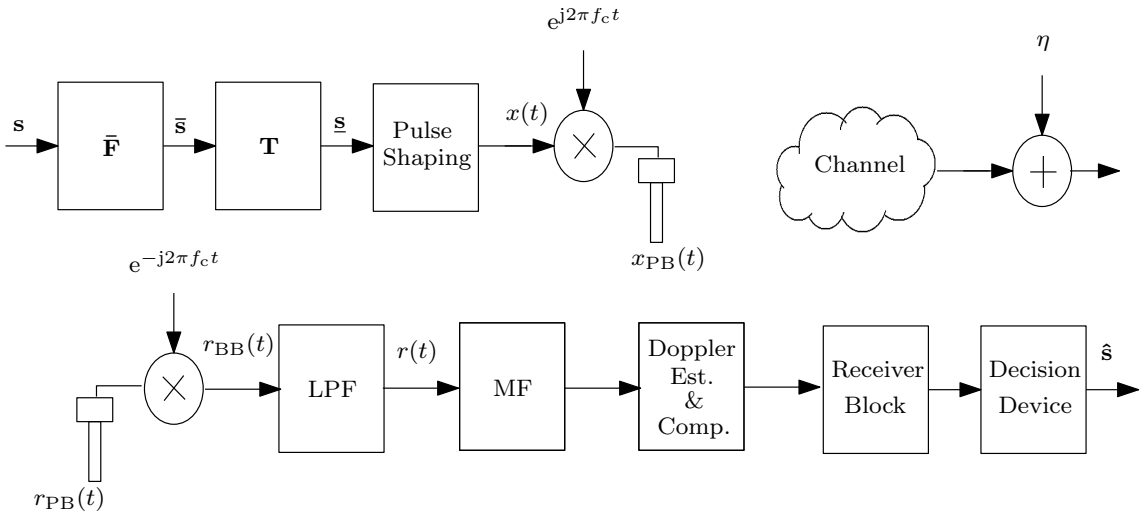

Figure 3.1: Communication model.

3.1.1 Transmitter Model

Let $\boldsymbol{s}_i \in \mathbb{C}^M$ be a block of data with index $i \in \mathbb{N}$ containing M symbols. A transmitter matrix is applied in each data block as:

$$\bar{\boldsymbol{s}}_i = \bar{\boldsymbol{F}}\boldsymbol{s}_i. \tag{3.1}$$

where $\bar{\boldsymbol{F}} \in \mathbb{C}^{M\times M}$ is the transmitter matrix. For the Single-Carrier Frequency Domain (SC-FD) system, $\bar{\boldsymbol{F}} = \boldsymbol{I}$, and for Orthogonal Frequency-Division Multiplexing system (OFDM), $\bar{\boldsymbol{F}} = \boldsymbol{F}^{-1}$, where $\boldsymbol{F}^{-1} \in \mathbb{C}^{M\times M}$ is the IDFT matrix with $[\boldsymbol{F}]_{k,l} = \frac{1}{\sqrt{M}} e^{-j\frac{2\pi}{M}kl}$. In the following step, a prefix with size K is added to $\bar{\boldsymbol{s}}_i$:

$$\underline{\boldsymbol{s}}_i = \boldsymbol{T}\bar{\boldsymbol{s}}_i, \tag{3.2}$$

where $\boldsymbol{T}$ is the matrix that adds the prefix, usually selected as a zero prefix or a cyclic prefix. $\boldsymbol{T}_{\text{ZP}}$ represents the matrix that adds the zero prefix and is defined as

$$\boldsymbol{T}_{\text{ZP}} = \begin{bmatrix} \boldsymbol{I}_M \\ \boldsymbol{0}_{K\times M} \end{bmatrix}, \tag{3.3}$$

whereas $\boldsymbol{T}_{\text{CP}}$ represents the matrix that adds the cyclic prefix:

$$\boldsymbol{T}_{\text{CP}} = \begin{bmatrix} \boldsymbol{0}_{K\times(M-K)} & \boldsymbol{I}_K \\ & \boldsymbol{I}_M \end{bmatrix}. \tag{3.4}$$

The amount of redundancy K inserted in the signal is $\left\lceil \frac{L}{2} \right\rceil \leq K \leq L$ and the size of the transmitted block is $(M + K) > L$. In other words, the amount of redundancy inserted in the signal has at least half of the channel order (L).

The sequence of vectors $\underline{\boldsymbol{s}}_i$ is mapped into a waveform format as follows:

$$x(t) = \sum_{i=0}^{I-1} \sum_{n=0}^{M+K-1} \underline{s}_i(n) p(t - nT - i(M+K)T), \tag{3.5}$$

where $p(t)$ is the basic pulse waveform, T is the symbol period and I is the number of blocks being considered in the analysis. The resulting signal $x(t)$ is modulated by the carrier generating the passband signal:

$$x_{\mathrm{PB}}(t) = 2\Re\left\{x(t)\mathrm{e}^{\mathrm{j}2\pi f_c t}\right\} \tag{3.6}$$

with f_c being the central frequency of the carrier. The signal $x_{\mathrm{PB}}(t)$ is now ready to be transmitted through the channel.

3.1.2 Channel Model

The channel impulse response is given by

$$h(t,\tau) = \sum_{l=0}^{L} h_l(t)\delta(\tau - \tau_l(t)) \tag{3.7}$$

where $L+1$ is the channel length, and $\tau_l(t)$ is the time delay of path l or the time that the transmitted signal takes to be observed at the receiver.

The time delay of path l, represented by $\tau_l(t)$ can be defined as

$$\tau_l(t) = \frac{d_l(t)}{c} = t - \alpha_l(t), \tag{3.8}$$

where $d_l(t)$ is the distance that the signal, transmitted at time $\alpha_l(t)$, travels before reaching the receiver. As in [79], using Taylor series, the time delay $\tau_l(t)$ can be approximated by a polynomial of order N_{delay} as:

$$\tau_l(t) \approx a_0^{(l)} - a_1^{(l)}t + \frac{1}{2}a_2^{(l)}t^2 - \frac{1}{6}a_3^{(l)}t^3 + \cdots + \frac{(-1)^{N_{\mathrm{delay}}}}{N_{\mathrm{delay}}!}a_{N_{\mathrm{delay}}}^{(l)}t^{N_{\mathrm{delay}}}. \tag{3.9}$$

A possible interpretation of the coefficients of Eq. (3.9) is given hereafter. Without loss of generality, the transmitter can be considered static, and just the receiver to be moving. In this case, the distance that the signal will travel from transmitter to the receiver through path l is given by

$$d_l(t) \approx d_{0,l} + v_{0,l}t + \frac{1}{2}m_{0,l}t^2 + \frac{1}{6}b_{0,l}t^3 + \cdots \tag{3.10}$$

where $d_{0,l}$ is the initial distance of path l, $v_{0,l}$ is the initial relative velocity perceived

by the signal that traversed path l, $m_{0,l}$ is the initial acceleration, and $b_{0,l}$ is a parameter representing the acceleration derivative. Notice that $d_l(t)$ represents the distance that the signal arriving at t has traveled.

For a constant wave speed c, the relationship between the distance $d_l(t)$ and the time delay $\tau_l(t)$ is

$$\tau_l(t) = \frac{d_l(t)}{c} = \underbrace{\frac{d_{0,l}}{c}}_{a_0^{(l)}} + \underbrace{\frac{v_{0,l}}{c}}_{-a_1^{(l)}} t + \frac{1}{2}\underbrace{\frac{m_{0,l}}{c}}_{a_2^{(l)}} t^2 + \frac{1}{6}\underbrace{\frac{b_{0,l}}{c}}_{-a_3^{(l)}} t^3 + \cdots . \tag{3.11}$$

Remark:

The first order approximation of the polynomial in Eq. (3.9) (as in [80]), results in

$$\tau_l(t) \approx a_0^{(l)} - a_1^{(l)} t. \tag{3.12}$$

Considering the approximation of Eq. (3.12), we notice that the Doppler frequency is related to $a_1^{(l)}$ as follows

$$f_{\mathrm{D}_l} = -f_{\mathrm{c}} a_1^{(l)} = f_{\mathrm{c}} \frac{v_l}{c}, \tag{3.13}$$

where f_{D_l} is the Doppler frequency inherent to path l, v_l is the relative velocity between transmitter and receiver perceived by the signal that traversed path l, and c is the wave speed. From Eq. (3.13) one can conclude that higher relative velocity leads to higher Doppler effect. The Doppler effect produces a time warping effect on the transmitted signal. Besides, it also distorts the signal phase. Thus, in order to recover the original signal, this effect must be properly estimated and compensated.

As the wave speed of propagation depends on the medium, and on the wave type, each communication system may experience distinct Doppler effect intensities. Appendix B contains a comparison of Doppler effects in two distinct transmission mediums, in order to understand the influence of the central frequency, as well as the relative movement, which are related to the Doppler frequency (see Eq. (3.13)).

For understanding the accuracy requirement of the Doppler estimator, we started our research considering a scenario with mild Doppler effect, i.e., an RF communications over the air. We investigated the performance of transceivers with distinct redundancy lengths embedded in an environment subject to Doppler effects. This study is presented in Appendix C.

3.1.3 Receiver Model

The received signal in the passband can be written as

$$\begin{aligned} r_{\mathrm{PB}}(t) &= x_{\mathrm{PB}}(t) * h(t,\tau) + \eta_{\mathrm{PB}}(t) \\ &= \int_{-\infty}^{\infty} h(t,\tau) x_{\mathrm{PB}}(t-\tau) d\tau + \eta_{\mathrm{PB}}(t) \\ &= \int_{-\infty}^{\infty} \sum_{l=0}^{L} h_l(t)\delta(\tau-\tau_l(t)) x_{\mathrm{PB}}(t-\tau) d\tau + \eta_{\mathrm{PB}}(t) \\ &= \sum_{l=0}^{L} h_l(t) x_{\mathrm{PB}}(t-\tau_l(t)) + \eta_{\mathrm{PB}}(t), \end{aligned} \tag{3.14}$$

where

$$\begin{aligned} x_{\mathrm{PB}}(t-\tau_l(t)) &= 2\Re\left\{x(t-\tau_l(t))\mathrm{e}^{\mathrm{j}2\pi f_{\mathrm{c}}(t-\tau_l(t))}\right\}. \\ &= x(t-\tau_l(t))\mathrm{e}^{\mathrm{j}2\pi f_{\mathrm{c}}(t-\tau_l(t))} + x^*(t-\tau_l(t))\mathrm{e}^{-\mathrm{j}2\pi f_{\mathrm{c}}(t-\tau_l(t))}. \end{aligned} \tag{3.15}$$

Substituting Eq. (3.15) in Eq. (3.14), we get

$$\begin{aligned} r_{\mathrm{PB}}(t) &= \sum_{l=0}^{L} h_l(t)\left\{x(t-\tau_l(t))\mathrm{e}^{\mathrm{j}2\pi f_{\mathrm{c}}(t-\tau_l(t))} + x^*(t-\tau_l(t))\mathrm{e}^{-\mathrm{j}2\pi f_{\mathrm{c}}(t-\tau_l(t))}\right\} \\ &\quad +\eta_{\mathrm{PB}}(t). \end{aligned} \tag{3.16}$$

The representation of the received signal in baseband can be obtained by removing the carrier frequency

$$\begin{aligned} r_{\mathrm{BB}}(t) &= r_{\mathrm{PB}}(t)\mathrm{e}^{-\mathrm{j}2\pi f_{\mathrm{c}}t} \\ &= \sum_{l=0}^{L} h_l(t)\left\{x(t-\tau_l(t))\mathrm{e}^{-\mathrm{j}2\pi f_{\mathrm{c}}\tau_l(t)} + x^*(t-\tau_l(t))\mathrm{e}^{-\mathrm{j}2\pi f_{\mathrm{c}}(2t-\tau_l(t))}\right\} \\ &\quad +\eta_{\mathrm{PB}}(t)\mathrm{e}^{-\mathrm{j}2\pi f_{\mathrm{c}}t}. \end{aligned} \tag{3.17}$$

A lowpass filter is employed in order to remove the unwanted components that are located at high frequency, resulting in:

$$\begin{aligned} r(t) &= \mathrm{LPF}\left\{r_{\mathrm{BB}}(t)\right\} \\ &= \sum_{l=0}^{L} h_l(t) x(t-\tau_l(t))\mathrm{e}^{-\mathrm{j}2\pi f_{\mathrm{c}}\tau_l(t)} + \eta_{\mathrm{PB}}(t)\mathrm{e}^{-\mathrm{j}2\pi f_{\mathrm{c}}t}. \end{aligned} \tag{3.18}$$

After the lowpass filter, a Doppler estimation and compensation technique is performed in the signal of Eq. (3.18). Notice that in this processing block, a signal rate convertion is performed. Before this block, the signal was represented in the

continuous domain as $r(t)$, and after this processing, the signal is represented in the discrete domain as $y(n)$, whose sampling period is T.

As our objective is to study further and to propose new techniques for Doppler estimation and compensation, we skip the mathematical model of this signal processing block in this chapter. A detailed discussion concerning this issue is presented in Chapters 4 and 5.

Assuming that the Doppler effect was perfectly estimated and compensated, the signal before being processed by the receiver block (see Fig. 3.1) can be written as

$$y(n) = \sum_{l=0}^{L} h_l(n)x(n-l) + \eta(n). \tag{3.19}$$

Considering that the channel is time invariant during the entire transmission, i.e., $h_l(n) = h_l$, Eq. (3.19) can be rewritten as

$$y(n) = \sum_{l=0}^{L} h_l x(n-l) + \eta(n). \tag{3.20}$$

For the zero padding case, the signal of Eq. (3.20) can be described in a vector form, with i-th block being represented as

$$\boldsymbol{y}_i = \boldsymbol{H}_{\text{ISI}}\boldsymbol{T}_{\text{ZP}}\bar{\boldsymbol{F}}\ \boldsymbol{s}_i + \boldsymbol{H}_{\text{IBI}}\boldsymbol{T}_{\text{ZP}}\bar{\boldsymbol{F}}\ \boldsymbol{s}_{i-1} + \boldsymbol{\eta}_i, \tag{3.21}$$

where $\boldsymbol{H}_{\text{ISI}} \in \mathbb{C}^{(M+K)\times(M+K)}$, $\boldsymbol{H}_{\text{IBI}} \in \mathbb{C}^{(M+K)\times(M+K)}$ are respectively the matrix comprising part of the channel that causes the intersymbol interference (ISI) inside the same block, and the matrix containing part of the channel that causes interblock interference (IBI). $\boldsymbol{H}_{\text{ISI}}$ is given by the following Toeplitz matrix

$$\boldsymbol{H}_{\text{ISI}} = \begin{bmatrix} h_0 & 0 & 0 & & \cdots & & 0 \\ h_1 & h_0 & 0 & & & & \\ \vdots & \vdots & \ddots & & & & \\ h_L & h_{L-1} & & \ddots & \ddots & & \vdots \\ 0 & h_L & & & \ddots & & \\ \vdots & \ddots & \ddots & & & \ddots & 0 \\ 0 & \cdots & 0 & h_L & \cdots & & h_0 \end{bmatrix}, \tag{3.22}$$

and $\boldsymbol{H}_{\text{IBI}}$ is given by the following matrix

$$\boldsymbol{H}_{\text{IBI}} = \begin{bmatrix} 0 & \cdots & 0 & h_L & \cdots & h_2 & h_1 \\ & & & 0 & h_L & \cdots & h_2 \\ & & & & & \ddots & \vdots \\ \vdots & & & & \ddots & & h_L \\ & & & & & & 0 \\ & & & & & & \\ 0 & & & \cdots & & & 0 \end{bmatrix}. \tag{3.23}$$

In the next step, a linear transformation $\boldsymbol{G}$ is applied in the signal $\boldsymbol{y}_i$ described by Eq. (3.21), resulting in the following signal estimation

$$\hat{\boldsymbol{s}}_i = \boldsymbol{G}\boldsymbol{H}_{\text{ISI}}\boldsymbol{T}_{\text{ZP}}\bar{\boldsymbol{F}}\ \boldsymbol{s}_i + \boldsymbol{G}\boldsymbol{H}_{\text{IBI}}\boldsymbol{T}_{\text{ZP}}\bar{\boldsymbol{F}}\ \boldsymbol{s}_{i-1} + \boldsymbol{G}\boldsymbol{\eta}_i, \tag{3.24}$$

with $\boldsymbol{G}$ being represented by

$$\boldsymbol{G} = \left[\mathbf{0}_{M\times(L-K)} \quad \overline{\boldsymbol{G}}\right], \tag{3.25}$$

and $\overline{\boldsymbol{G}} \in \mathbb{C}^{M\times(M+2K-L)}$ is the receiver matrix. Eq. (3.24) is rewritten as

$$\hat{\boldsymbol{s}}_i = \bar{\boldsymbol{G}}\bar{\boldsymbol{H}}\bar{\boldsymbol{F}}\ \boldsymbol{s}_i + \boldsymbol{G}\boldsymbol{\eta}_i. \tag{3.26}$$

It is important to perceive that the process of insertion and removal of the zeros eliminated the IBI. The abovementioned matrix $\bar{\boldsymbol{H}}$ is given by

$$\bar{\boldsymbol{H}} = \begin{bmatrix} h_{L-K} & \cdots & h_0 & 0 & 0 & \cdots & 0 \\ \vdots & \ddots & & & & & \vdots \\ h_K & \ddots & & & & & 0 \\ \vdots & \ddots & & & \ddots & & h_0 \\ h_L & & & & & & \vdots \\ 0 & & & & \ddots & & h_{L-K} \\ \vdots & & & & & & \vdots \\ 0 & \cdots & 0 & 0 & h_L & \cdots & h_K \end{bmatrix}. \tag{3.27}$$

A possible receiver matrix $\bar{\boldsymbol{G}}$ is [81]:

$$\bar{\boldsymbol{G}}_{\text{MMSE}} \ = \ \boldsymbol{F}^H \left(\bar{\boldsymbol{H}}^H\bar{\boldsymbol{H}} + \frac{1}{\text{SNR}}\boldsymbol{I}_M\right)^{-1}\bar{\boldsymbol{H}}^H, \tag{3.28}$$

where SNR is the signal-to-noise ratio. Notice that the objective of this receiver matrix is to minimize the mean square error (MSE) of the received signal. Besides that, the matrix described in Eq. (3.28) considers a multicarrier system, and is designed for a reduced redundancy system K, with $\lceil L/2 \rceil \leq K < L$.

The channel impulse response denoted by $\bar{\boldsymbol{H}}$ can be estimated as [82]

$$\hat{\boldsymbol{h}} = \left(\bar{\boldsymbol{S}}^H \bar{\boldsymbol{S}} + \frac{1}{\text{SNR}} \boldsymbol{I}_{L+1} \right)^{-1} \bar{\boldsymbol{S}}^H \boldsymbol{y} \tag{3.29}$$

with $\bar{\boldsymbol{S}}$ being a Toeplitz matrix containing the transmitted pilot symbols, whose first row is $[\bar{s}(L/2) \cdots \bar{s}(0) \;\; \mathbf{0}_{1\times L/2}]$, and the first column is $[\bar{s}(L/2) \cdots \bar{s}(M-1) \;\; \mathbf{0}_{1\times L/2}]^T$. Notice that this channel estimation considers a minimum redundancy system, and that the first transmitted block contains only pilot symbols.

Notice that the main feature of block transceivers presented here is their ability to cope with dispersive channels. Thus, if we have additional knowledge about the underwater acoustic channel, we might be able to design transceivers that are even more suitable for underwater acoustic environment, and improve the system performance. With this objective, we analyzed and studied the channel frequency response of a given location. All this analysis will be presented in the following section.

3.2 Evaluation of Underwater Acoustic Channel in Arraial do Cabo

Several attempts to model the underwater acoustic communication channel have been made. For example, in [37], measurements were performed in the north of Europe to characterize the underwater acoustic channel. However, the conclusion of the work was that none of the observed effects could be considered as typical nor as a special case for this type of communication. In [27], the channel is modeled stochastically using measurements collected in an experiment performed in the Narragansett Bay, situated in the USA coast. This work concludes that the channel path gains follow Ricean fading models. In [29], a channel model for high-frequency in warm shallow water is developed. This model is tested with experimental data collected in Singapore where it has been found that the channel path gains follow Rayleigh fading models. All of these results show that there is not a unique appropriate channel model, meaning that the channel models might be site-dependent.

3.2.1 Motivation

Arraial do Cabo has underwater monitoring station of Brazilian Navy, being an important communication and monitoring site in Brazil South East coast. Information about the channel frequency response might improve the experiments performed at this site.

The channel frequency response calculated in this section considers path loss and multipath fading. Notice that the multipath signals may arrive at close time instants such that the reflections can be unresolvable, and the combination of all these reflections gains compose the path gain. These phenomena will be reproduced in the channel model with the help of the Bellhop program [83], which provides as output all the rays that arrive at the receiver at all time instants.

3.2.2 Bellhop Program

There are several approaches for modeling wave propagation in literature. The wave propagation can be modeled using ray theory, Normal mode approach, Multipath expansion, Fast field, or parabolic equation [38]. As the ray theory approach is the only one applicable and/or practical for frequency ranges above 500 Hz for both shallow water and deep water environments [38], we employ this methodology for the evaluation of the channel frequency response.

Bellhop is a program that performs ray tracing for a given scenario. The scenario setup may include sound speed profile or sound speed field, bathymetric profile, and surface profile. Some possible outputs are amplitude and the time delay of each arriving ray. Thus, for computing the channel frequency response, we use the Bellhop program for each frequency of interest with the selected scenario. As we have as output the amplitude and the time delay of each ray, we perform the phasorial sum of amplitudes of the arriving rays as follows:

$$G(l,f) \;=\; \sum_{n=1}^{N_{\text{paths}}} G_n(l,f)\mathrm{e}^{\mathrm{j}2\pi f\xi_n}, \tag{3.30}$$

where $|G(l,f)|$ represents the channel gain of frequency f, considering a distance of l meters between transmitter and receiver. The variable N_{paths} denotes the number of channel paths with respect to the conditions described above, $G_n(l,f)$ is complex amplitude of the n-path, and ξ_n is the time delay of the n-path. This procedure is repeated for a frequency range. Notice that, using this simulator, both path loss and multipath fading effects are considered in the channel frequency response. As *ray theory*[2] has restrictive assumptions in shallow water for frequencies under

[2] *Ray theory* considers ray tracing for computing the transmission loss.

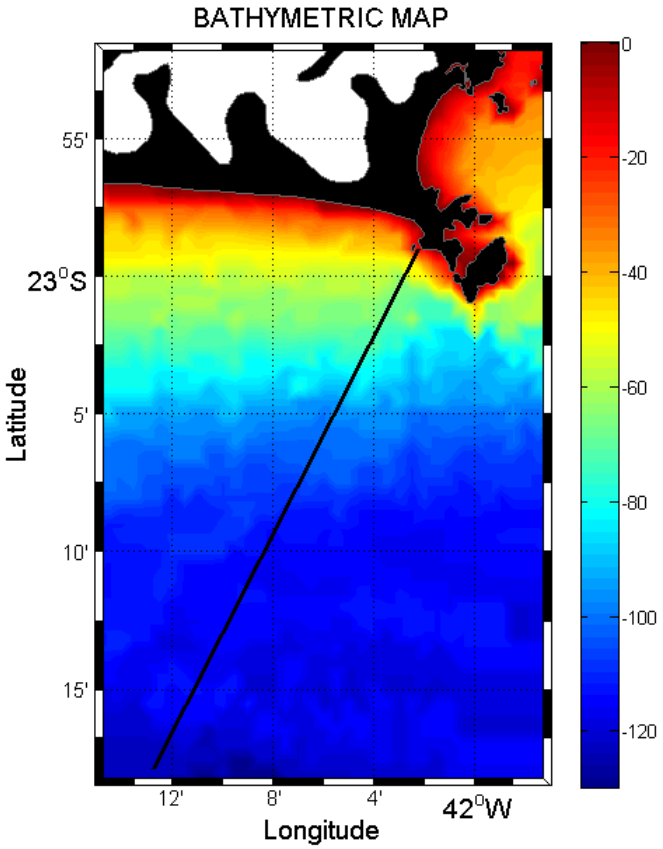

Figure 3.2: Arraial do Cabo coast bathymetric map (in meters).

500 Hz [38], the channel frequency response might not be accurate in this frequency range.

3.2.3 Scenario - Arraial do Cabo

The site we are interested is located in Arraial do Cabo coast, situated in Rio de Janeiro state, Brazil. For performing the calculation of the channel frequency response, we used a Bathymetric profile, a surface profile, and a sound speed propagation profile acquired in Arraial do Cabo. The bathymetric map[3] of Arraial do Cabo is shown in Figure 3.2. The bathymetric profile considered in this work is the black line in Figure 3.2. The maximum depth is about 130 meters, representing a shallow water environment.

As the sea bottom of the interested location is composed mostly by fine sand, the measured sound speed at this seafloor was 1684 m/s, the bottom density was 1.99 g/ cm^3 and the signal bottom attenuation was 0.6 dB/λ. These geoacoustics data were collected in a previous work [84].

[3]The bathymetric map shows the sea depth.

Table 3.1: Receiver depth × distance

Tx/Rx distance (km)	Receiver Depth (m)				
1	10	15	20	25	30
5	15	20	30	40	50
10	15	30	40	50	60
20	15	30	50	70	85
40	15	30	50	70	90

Noise Measurement

A measurement of the ambient noise was performed using the hydrophone ITC-8073C. These measurements were transmitted through a cable whose length is 700 meters. As the cable is modeled as a lowpass filter with cutoff frequency around 70 kHz, we consider that the frequency response is flat in the range $0 < f < 20$ kHz. Besides, the hydrophone sensitivity is approximated as flat, whose nominal value is considered to be the midband: -167 dB re $1V/\mu$ Pa[4].

3.2.4 Simulation Results

As our objective is to find the frequency range with the minimum channel attenuation, we analyzed the channel frequency response due to path loss according to [39] and also the channel frequency response provided by the Bellhop simulator. The knowledge of the channel frequency response enables the communication to be established with reasonable power, since the system might operate in the frequency range in which the channel has minimum attenuation.

The channel frequency response was calculated for the following transmitter/receiver distances: 1, 5, 10, 20 and 40 kilometers. For each distance, the receiver was placed at 5 different depths, and the channel gain $G(l, f)$ is obtained by averaging the results of these 5 experiments. The channel gain of each experiment is calculated using the Bellhop program. Table 3.1 shows the receiver depths for each transmitter/receiver distance. The transmitter is placed at 16 meters of depth and the source aperture was 90 degrees. The simulation setups are depicted in Figure 3.3.

Figure 3.4 shows the channel frequency response for all the distances between transmitter and receiver. This figure depicts the channel characterized only by the path loss (legend with subscript PL), as described in [39], and the channel obtained using Bellhop program. Considering the same frequency, the channel has higher attenuation for longer distances between transmitter and receiver. Also, for the same distance between transmitter and receiver, the channel attenuation is lower

[4]The unit of the hydrophone sensitivity is expressed as the sound field strength in dB relative (re) to 1 V/Pa.

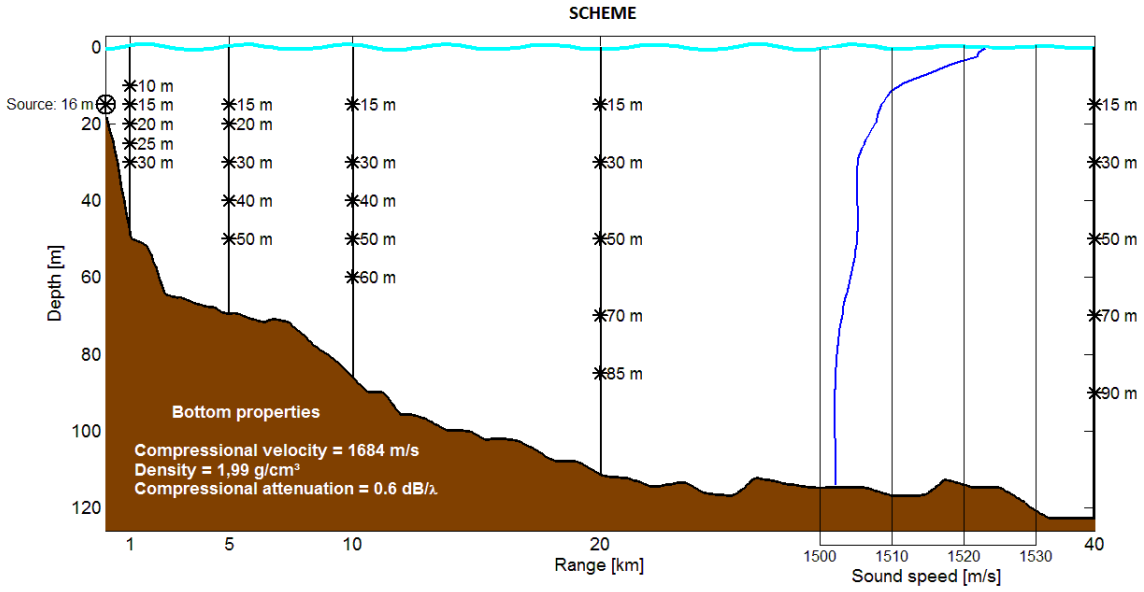

Figure 3.3: Simulation setup.

for lower frequencies. Besides, when considering the multipath effects, i.e., using Bellhop program, the channel gain is lower than the case where the channel is characterized with only path loss.

Figures 3.5, 3.6 show the channel frequency response for the case that the receiver is placed 10 kilometers ahead from the transmitter, and at 15 and 60 meters depth respectively. As observed from these figures, the channel frequency response presents distinct attenuations regarding the case in which the distance between transmitter and receiver is the same.

Besides the channel frequency response, we analyzed the signal-to-noise ratio (SNR) using the knowledge of the channel and of the ambient noise measured at the site probed. The SNR is given by

$$\mathrm{SNR}(l, f) = \frac{P\ |G(l, f)|^2}{N(f)}. \tag{3.31}$$

where P is the signal transmission power, that will be considered as unitary, and $N(f)$ is the noise power spectral density. Notice that the SNR depends on the signal frequency, and on the distance between transmitter and receiver.

Figure 3.7 depicts the SNR for each frequency considering the two characterization of the channel frequency response. For all cases, longer distances lead to higher attenuation. Once more, the SNR is greater if the channel is characterized with path loss only. We can notice that there is an attenuation near the frequency 19 kHz for all SNR curves. The noise around this frequency presents an unexpected characteristic in this region.

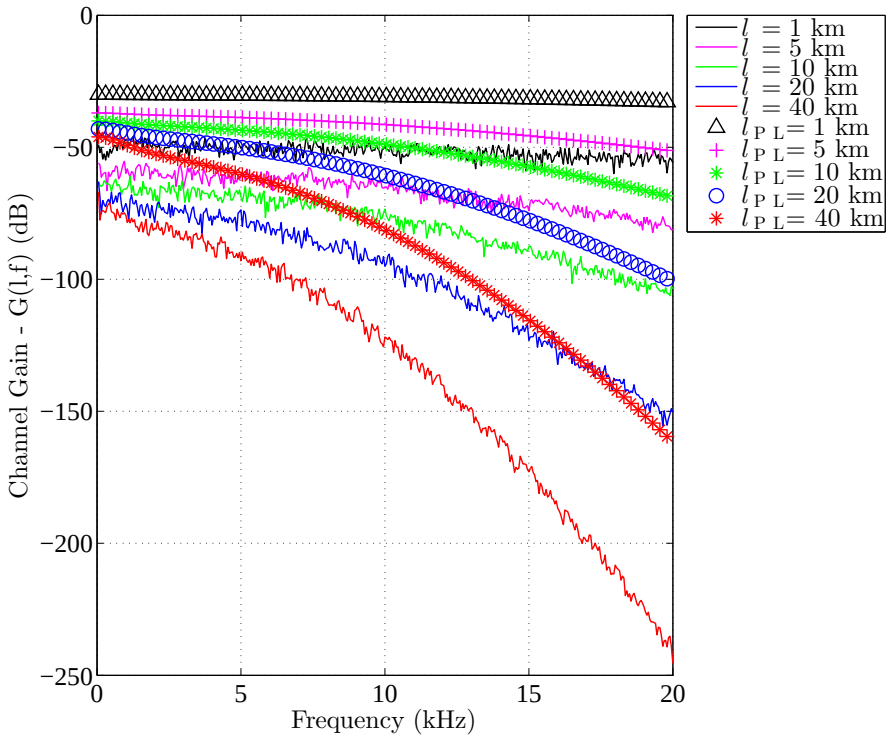

Figure 3.4: Channel frequency response for a channel characterized only by the path loss (legend with subscript PL) and for a channel obtained using Bellhop. Each curve corresponds to a distinct transmission distance, which is denoted by l.

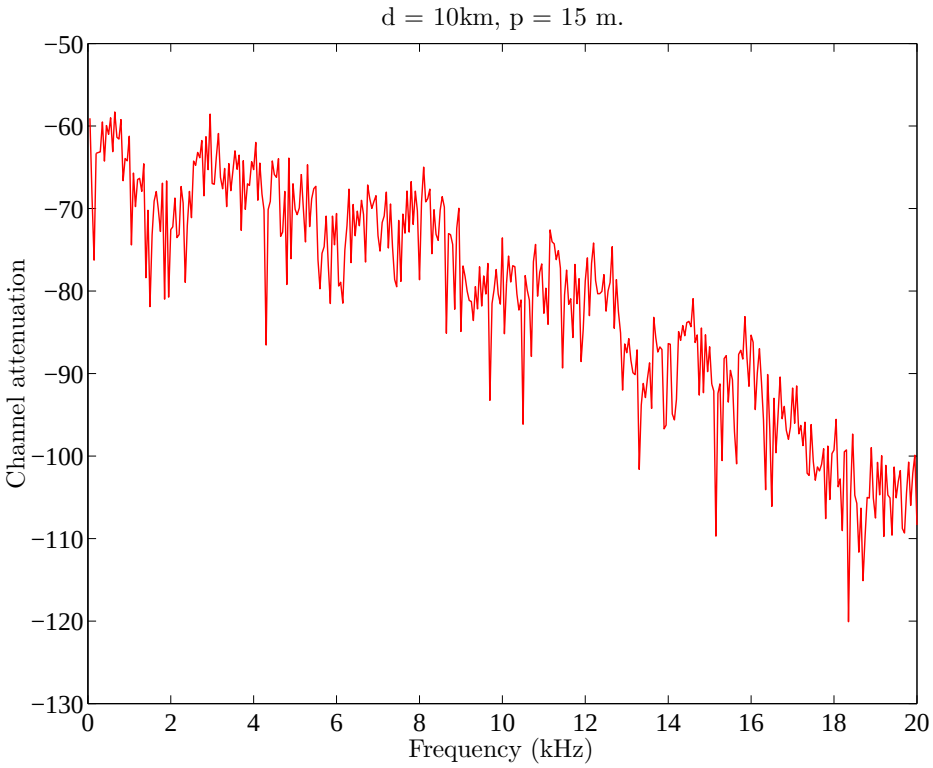

Figure 3.5: Channel frequency response obtained using Bellhop for a receiver placed at 15 meters depth, and 10 kilometers from the transmitter.

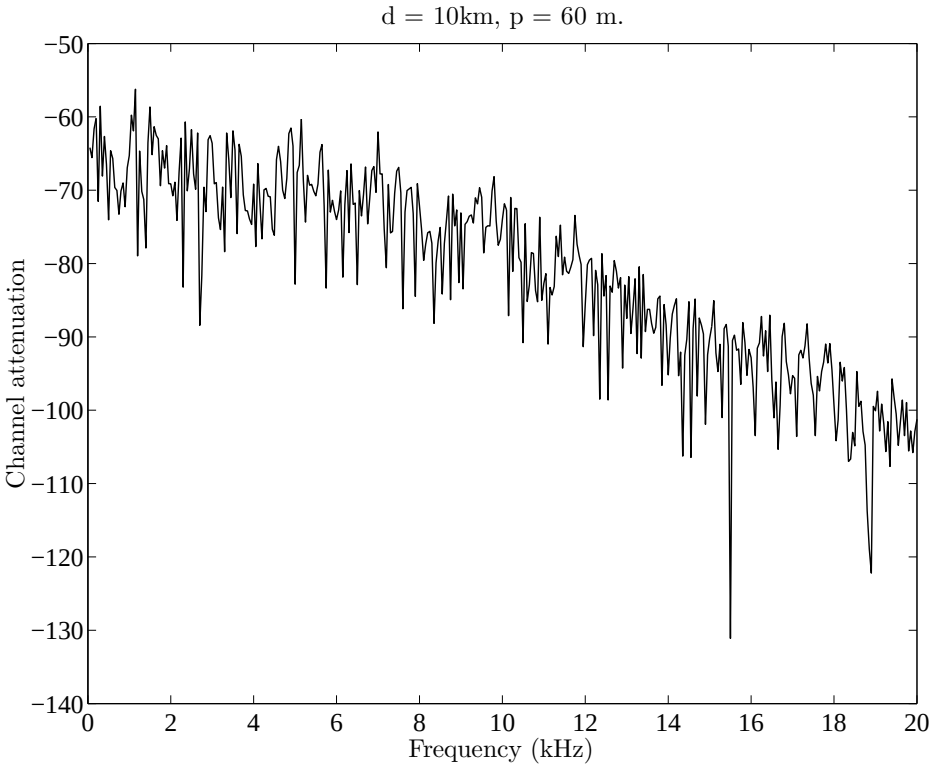

Figure 3.6: Channel frequency response obtained using Bellhop for a receiver placed at 60 meters depth, and 10 kilometers from the transmitter.

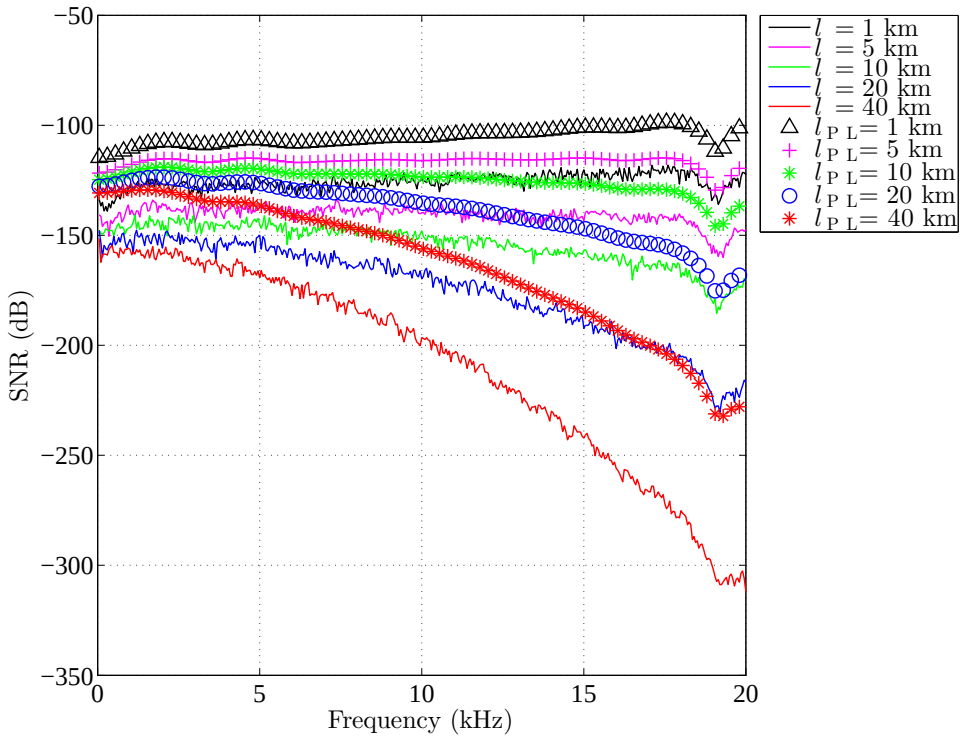

Figure 3.7: SNR for a channel characterized only by the path loss (legend with subscript PL) and for a channel obtained using Bellhop program. Each curve corresponds to a distinct transmission distance, which is denoted by l.

3.3 Summary

In this chapter we introduced the communication setup that will be further used in this thesis. As we will further analyze and discuss methods for processing Doppler effects, we omitted from this chapter its mathematical model. Chapters 4, 5 show studies and proposals of new solutions to overcome this problem.

Besides, we analyzed the channel frequency response and the SNR in Arraial do Cabo coast. The channel frequency response is characterized by the large-scale fading and small-scale fading, that were calculated using the Bellhop program. The simulated scenario considered measurements acquired at the site. As expected the results show that lower frequencies lead to lower attenuation when transmitting signals over longer distances. Besides that, we observed that a longer transmission distance leads to a higher signal attenuation. As this study provided channel parameters useful in the modeling of a real underwater acoustic environment, some obtained results are used in Chapter 6.

Chapter 4

Analysis of a Doppler Effect Compensation Technique

In this chapter we present, justify, analyze, and propose a simplified version of the algorithm developed by [43, 44] for estimating and compensating Doppler effects. The algorithm was originally proposed in an ad hoc manner, so that the justification and analysis conducted here are contributions of this work to the best of our knowledge.

The chapter is organized as follows: Section 4.1 presents assumptions regarding the channel characteristics that will be considered in the algorithm development. Section 4.2 states the problem of resampling estimate utilizing the aforementioned algorithm and analyzes its performance. Section 4.3 presents our algorithm simplification proposal for addressing the case whenever the transmitted pilot signal is not available at the receiver side. In addition, we propose a procedure to determine how often the algorithm should be trained, and verify the results through simulations. Section 4.4 presents the chapter conclusions.

4.1 Channel Assumptions

There are several available methods for estimating and compensating the Doppler effect. The adaptive feature of the algorithm proposed in [43, 44] is attractive to cope with the time-varying behavior of the Doppler effect. Since this algorithm considers a channel with a single path and unitary gain, we start our analysis with the same assumptions.

The system model employed in this chapter is the one shown in Section 3.1. Equation (3.18) represents the received signal after passing through the lowpass filter at the receiver end. Under the aforementioned hypothesis of a single path and

unitary gain channel, Equation (3.18) can be rewritten as

$$\begin{aligned} r(t) &= \mathrm{e}^{-\mathrm{j}2\pi f_c \tau(t)} x(t-\tau(t)) + \eta(t) \\ &= \mathrm{e}^{-\mathrm{j}2\pi f_c \tau(t)} r_b(t-\tau(t)) + \eta(t) \end{aligned} \tag{4.1}$$

where

$$r_b(t-\tau(t)) = x(t-\tau(t)). \tag{4.2}$$

Let us define

$$\varphi(t) = -2\pi f_c \frac{d(t)}{c} = 2\pi f_c(\alpha(t) - t), \tag{4.3}$$

where $d(t)$ is the distance between transmitter and receiver and $\alpha(t)$ represents the instant the signal left the transmitter. Using Eq. (3.8), which is repeated here for convenience,

$$\tau(t) = \frac{d(t)}{c} = t - \alpha(t), \tag{4.4}$$

then Eq. (4.1) can be rewritten as

$$\begin{aligned} r(t) &= r_b\left(t - \frac{d(t)}{c}\right) \mathrm{e}^{-\mathrm{j}2\pi f_c \frac{d(t)}{c}} + \eta(t) \\ &= r_b(\alpha(t)) \mathrm{e}^{\mathrm{j}\varphi(t)} + \eta(t). \end{aligned} \tag{4.5}$$

In order to recover the transmitted signal, we need to estimate and compensate the time warping caused by the factor $\alpha(t)$, which is related to the Doppler effect. A possible way of estimating and tracking the variation of this parameter is presented hereafter.

In [43, 44] is proposed an algorithm based on Kalman filter for Doppler estimation and compensation. Here, in this thesis, we re-interpret, introduce, and analyze the algorithms under a distinct perspective.

4.2 Resampling Estimate

Our aim is to recover equally spaced samples of $r_b(t)$ from the observation described by Eq. (4.5). This goal can be achieved if the received signal is discretized by replacing t with a function $\beta(nT)$. In this case the received signal can be described

in the discrete-time domain as

$$\begin{aligned} r(\beta(nT)) &= r_b\left(\beta(nT) - \frac{d(\beta(nT))}{c}\right) \mathrm{e}^{-\mathrm{j}2\pi f_c \frac{d(\beta(nT))}{c}} + \eta(\beta(nT)) \\ &= r_b(\alpha(\beta(nT)))\mathrm{e}^{\mathrm{j}\varphi(\beta(nT))} + \eta(\beta(nT)) \\ &= r_b(\alpha(\beta(nT)))\mathrm{e}^{\mathrm{j}2\pi f_c(\alpha(\beta(nT))-\beta(nT))} + \eta(\beta(nT)). \end{aligned} \tag{4.6}$$

The key issue is to obtain a function $\beta(t)$, or a set of sampling moments at the receiver $\beta(nT)$ such that the samples of $r(t)$ we are collecting are a direct function of the equally spaced sampled version of $r_b(t)$, i.e., $r_b(\alpha(\beta(nT))) = x(nT)$. We therefore need to find the function $\beta(t)$ such that

$$\alpha(\beta(nT)) = nT. \tag{4.7}$$

In the next section, two distinct models for estimating $\beta(\cdot)$ are presented. These two methods estimate the function $\beta(\cdot)$ that represents the inverse of $\alpha(\cdot)$.

4.2.1 Estimation of Doppler Effect

In this subsection, we describe and justify the method for estimating the function $\beta(\cdot)$, which is related to the Doppler effect.

Estimation of the Sampling Function based on [44]

Within a sample period, we define the rate of disturbance in the function $\beta(\cdot)$ with the parameter $\gamma(n)$ as

$$\beta((n+1)T) = \beta((n)T) + \gamma(n+1)T \tag{4.8}$$

where $\gamma(n+1)$ caused a variation in $\beta(\cdot)$. This means that $\gamma(n+1)$ modified the symbol period T to a new value. Since the functions[1] $\beta(\cdot)$, $\gamma(\cdot)$ related to the time variable distortions are system states, we have to estimate them from observations.

The idea of this algorithm is to find a function $\beta(\cdot)$ for both selecting the sampling moment as well as for performing the phase correction. After removing the phase-shift caused by Doppler effect, through a multiplication by $\mathrm{e}^{\mathrm{j}2\pi f_c(\beta(nT)-nT)}$ in Eq. (4.6), we get the following signal

$$\begin{aligned} \hat{r}(\beta(nT)) &= r_b(\alpha(\beta(nT)))\mathrm{e}^{-\mathrm{j}2\pi f_c(\beta(nT)-\alpha(\beta(nT)))}\mathrm{e}^{\mathrm{j}2\pi f_c(\beta(nT)-nT)} \\ &\quad +\eta(\beta(nT))\mathrm{e}^{\mathrm{j}2\pi f_c(\beta(nT)-nT)} \\ &= r_b(\alpha(\beta(nT)))\mathrm{e}^{\mathrm{j}2\pi f_c[\alpha(\beta(nT))-nT]} + \eta(\beta(nT))\mathrm{e}^{\mathrm{j}2\pi f_c(\beta(nT)-nT)}. \end{aligned} \tag{4.9}$$

[1] In some variables such as $\gamma(\cdot)$, $\beta(\cdot)$, the sampling period is omitted for simplicity.

Considering that $\beta(n)$ for $n = 1$ is available from the synchronization step, we can use the angle between the actual transmitted signal[2] $x(nT)$ and its estimate $\hat{r}(\beta(nT))$ as a measure of disturbance, since under the aforementioned channel assumptions, $\hat{r}(\beta(nT))$ is an estimation of the signal $x(nT)$. Thus,

$$\theta(n) = \arg(\hat{r}(\beta(nT))x^*(nT)) \tag{4.10}$$

represents the disturbance over a period T. As such, the computed argument disturbs $\gamma(n)$ so that

$$\gamma(n+1) \;=\; \gamma(n) - \mu\theta(n) \tag{4.11}$$

and

$$\beta(n+1) \;=\; \beta(n) + \gamma(n+1)T. \tag{4.12}$$

With these expressions, we can reach an expression for the phase distortion defined in Eq. (4.3) as follows:

$$\varphi(\beta(nT+T)) = \varphi(\beta(nT)) + 2\pi f_c T(1 - \gamma(n+1)), \tag{4.13}$$

where $\gamma(n+1)$ is the random term, and a proof of Eq. (4.13) is given below. Notice that the value of the function $\varphi(t)$ must be estimated at the same time instant that the received signal will be sampled, i.e., at $t = \beta(nT)$.

Proof. The proof of Eq. (4.13) follows. According to Eq. (4.3), for $t_1 = \beta(nT)$:

$$\varphi(\beta(nT)) = -2\pi f_c \frac{d(\beta(nT))}{c} = 2\pi f_c(\alpha(\beta(nT)) - \beta(nT)) \tag{4.14}$$

and for $t_2 = \beta(nT+T)$:

$$\varphi(\beta(nT+T)) = -2\pi f_c \frac{d(\beta(nT+T))}{c} = 2\pi f_c(\alpha(\beta(nT+T)) - \beta(nT+T)). \tag{4.15}$$

Subtracting Eq. (4.15) from Eq. (4.14), we get

$$\begin{aligned}
\varphi(\beta(nT+T)) - \varphi(\beta(nT)) \;&=\; 2\pi f_c\left[\alpha(\beta(nT+T)) - \beta(nT+T)\right] \\
&\quad -2\pi f_c\left[\alpha(\beta(nT)) - \beta(nT)\right] \\
&=\; 2\pi f_c\left[-\beta(nT+T) + \beta(nT)\right] \\
&\quad +2\pi f_c\left[\alpha(\beta(nT+T)) - \alpha(\beta(nT))\right]. \qquad (4.16)
\end{aligned}$$

[2]We are assuming the use of a training signal.

If $\alpha(\beta(nT+T)) = nT+T$ and $\alpha(\beta(nT)) = nT$, then

$$\varphi(\beta(nT+T)) - \varphi(\beta(nT)) = 2\pi f_{\mathrm{c}}\left[-\beta(nT+T) + \beta(nT) + T\right] \tag{4.17}$$

so that using Eq. (4.12) justifies Eq. (4.13). □

Estimation of the Sampling Function based on [43]

Like in the first approach, the received signal model is given by Eq. (4.5), and a proper choice of sampling leads to Eq. (4.6). As before, $\beta(n)$ for $n = 0$ is known due to synchronization. Using Eq. (4.3), Eq. (4.6) can be rewritten as

$$r(\beta(nT)) = r_b(\alpha(\beta(nT)))\mathrm{e}^{-\mathrm{j}2\pi f_{\mathrm{c}}(\beta(nT)-\alpha(\beta(nT)))} + \eta(\beta(nT)). \tag{4.18}$$

In order to remove the phase-shift caused by the Doppler effect, we should multiply Eq. (4.18) by $\mathrm{e}^{\mathrm{j}2\pi f_{\mathrm{c}}(\beta(nT)-nT)}$, thus obtaining

$$\begin{aligned}\hat{r}(\beta(nT)) &= r_b(\alpha(\beta(nT)))\mathrm{e}^{-\mathrm{j}2\pi f_{\mathrm{c}}(\beta(nT)-\alpha(\beta(nT)))}\mathrm{e}^{\mathrm{j}2\pi f_{\mathrm{c}}(\beta(nT)-nT)} \\ &\quad +\eta(\beta(nT))\mathrm{e}^{\mathrm{j}2\pi f_{\mathrm{c}}(\beta(nT)-nT)} \\ &= r_b(\alpha(\beta(nT)))\mathrm{e}^{\mathrm{j}2\pi f_{\mathrm{c}}[\alpha(\beta(nT))-nT]} + \eta(\beta(nT))\mathrm{e}^{\mathrm{j}2\pi f_{\mathrm{c}}(\beta(nT)-nT)}\end{aligned} \tag{4.19}$$

resulting in the same equation as (4.9).

Defining $\epsilon_n = \alpha(\beta(nT)) - nT$, Eq. (4.19) can be rewritten as

$$\hat{r}(\beta(nT)) = r_b(nT+\epsilon_n)\mathrm{e}^{\mathrm{j}2\pi f_{\mathrm{c}}\epsilon_n} + \eta(\beta(nT))\mathrm{e}^{\mathrm{j}2\pi f_{\mathrm{c}}(\beta(nT)-nT)}. \tag{4.20}$$

Assuming $\epsilon_n \ll nT$, Eq. (4.20) can be rewritten as

$$\hat{r}(\beta(nT)) \approx r_b(nT)\mathrm{e}^{\mathrm{j}2\pi f_{\mathrm{c}}\epsilon_n} + \eta_{\mathrm{PB}}(\beta(nT))\mathrm{e}^{-\mathrm{j}2\pi f_{\mathrm{c}}nT}, \tag{4.21}$$

where we kept ϵ_n at the exponent while not in time index, given that it affects much more the received signal since it is multiplied by $2\pi f_{\mathrm{c}}$ and the overall product determines the angle in the exponential. An analysis regarding the approximation utilized in Eq. (4.21) is performed in Section 4.3.1.

Assuming that the noise is negligible and $r_b(nT) = x(nT)$, we obtain the angle between the transmitted and received signals as

$$\theta(n) = \arg(\hat{r}(\beta(nT))x^*(nT)) \approx 2\pi f_{\mathrm{c}}\epsilon_n. \tag{4.22}$$

Knowing that the desired value for $\alpha(\beta(nT))$ is nT, we should attempt to derive a model to quantify how ϵ_n contributes to a change in the time warping $\beta(nT)$.

In the continuous time domain, since the ideal solution is $\alpha(\beta(t)) = t$, we can infer that $\beta(t) = \alpha^{-1}(t)$, as such it is possible to show that[3]

$$\frac{d\alpha^{-1}(t)}{dt} = \frac{d\beta(t)}{dt} = \frac{1}{\alpha'(\alpha^{-1}(t))} = \frac{1}{\alpha'(\beta(t))} \approx \frac{1}{\frac{\alpha(\beta(t)+\Delta t)-\alpha(\beta(t))}{\Delta t}} \quad \text{for} \quad \Delta t \to 0. \tag{4.23}$$

Defining the error caused by not properly estimating $\beta(t)$ at time instant t as $\epsilon_t = \alpha(\beta(t)) - t$, we can infer that

$$\dot{\beta}(t) = \frac{d\beta(t)}{dt} \approx \frac{1}{\frac{\alpha(\beta(t)+\Delta t)-\epsilon_t - t}{\Delta t}}. \tag{4.24}$$

Since $\dot{\beta}(t)$ includes ϵ_t at its denominator we can justify an update to $\dot{\beta}(t)$ as follows

$$\dot{\beta}(n+1) = \dot{\beta}(n) - \mu\epsilon_n \tag{4.25}$$

where μ is a small step size and use this estimate to update $\beta(n+1)$ as follows:

$$\beta(n+1) = \beta(n) + \dot{\beta}(n+1)T \tag{4.26}$$

where T is the sampling period.

In works [43, 44], the aim is to estimate the inverse of $\alpha(t)$ at $t = nT$, so that we can get the value of $r(\beta(nT))$ that is directly proportional to $r_b(nT)$ which in turn is a function of $x(nT)$. Thus for a frequency selective channel, after proper equalization applied to $r_b(nT)$ we can recover the transmitted sample $s(nT)$.

Relation between Models

The algorithms described above compensate the Doppler effect in the same way, although the derivation of each algorithm was performed in distinct manners as previously shown. The objective here is to understand the similarities and differences of the two alternative recursive update equations.

The algorithm of [44] is given by the following equations:

$$\gamma(n+1) = \gamma(n) - \mu_1\theta(n) \tag{4.27}$$

$$\beta(n+1) = \beta(n) + \gamma(n+1)T \tag{4.28}$$

$$\varphi(n+1) = \varphi(n) + 2\pi f_c T(1 - \gamma(n+1)), \tag{4.29}$$

where the variable $\beta(nT)$ is employed for sampling the received signal, and $\varphi(n)$ for

[3]We use the property of the derivative of an inverse function where $\frac{d[f^{-1}](t)}{dt} = \frac{1}{f'(f^{-1}(t))}$, which applies in the case the inverse exists in the neighborhood of the given point and the derivative is non-zero.

correcting the phase as follows:

$$\begin{aligned}\hat{r}(\beta(nT)) &= r(\beta(nT))\mathrm{e}^{-\mathrm{j}\varphi(n)} \\ &= x(\alpha(\beta(nT)))\mathrm{e}^{-\mathrm{j}2\pi f_\mathrm{c}(\beta(nT)-\alpha(\beta(nT)))}\mathrm{e}^{-\mathrm{j}\varphi(n)} \\ &\quad +\eta(\beta(nT))\mathrm{e}^{-\mathrm{j}\varphi(n)}. \end{aligned} \tag{4.30}$$

The algorithm of [43] is described as

$$\dot{\beta}(n+1) = \dot{\beta}(n) - \mu_2\epsilon_n \tag{4.31}$$

$$\beta(n+1) = \beta(n) + \dot{\beta}(n+1)T. \tag{4.32}$$

Notice that this algorithm does not include an equation for estimating the parameter $\varphi(n)$ employed in the phase correction. Instead, the variable $\beta(nT)$ is used for both time sampling and phase correction as follows:

$$\begin{aligned}\hat{r}(\beta(nT)) &= r(\beta(nT))\mathrm{e}^{-\mathrm{j}2\pi f_\mathrm{c}[nT-\beta(nT)]} \\ &= x(\alpha(\beta(nT)))\mathrm{e}^{-\mathrm{j}2\pi f_\mathrm{c}(\beta(nT)-\alpha(\beta(nT)))}\mathrm{e}^{-\mathrm{j}2\pi f_\mathrm{c}[nT-\beta(nT)]} \\ &\quad +\eta(\beta(nT))\mathrm{e}^{-\mathrm{j}2\pi f_\mathrm{c}[nT-\beta(nT)]}. \end{aligned} \tag{4.33}$$

As both algorithms perform a similar estimation and compensation of the Doppler effect, the time instant that each algorithm samples the received signal must be the same, i.e., the variable $\beta(nT)$ must have the same interpretation, and thus equal values in both algorithms. Also, the variables $\gamma(n)$ and $\dot{\beta}(nT)$ should have equal values and interpretations, because the symbol period is the same for both cases. As the definition of the parameters $\theta(n)$ and ϵ follows the relationship

$$\theta(n) = \arg(\hat{r}(\beta(nT))x^*(nT)) \approx 2\pi f_\mathrm{c}\epsilon_n, \tag{4.34}$$

we can conclude that in each case, the algorithms step sizes represented by μ_1 and μ_2 are related as:

$$\mu_1 = \frac{\mu_2}{2\pi f_\mathrm{c}} \tag{4.35}$$

where μ_1 is from [44] and μ_2 from [43]. Hence, in order to obtain the same Doppler estimation values in both cases, the relationship between the algorithms step sizes must follow Eq. (4.35).

4.2.2 Doppler Compensation

The estimated value of $\beta(nT)$ is employed in the sampling operation, as well as in the phase correction as follows. The received signal in baseband from Eq. (4.5) is sampled at $t = \beta(nT)$:

$$\begin{aligned} r(\beta(nT)) &= r_b(\alpha(\beta(nT)))\mathrm{e}^{\mathrm{j}\varphi(\beta(nT))} + \eta(\beta(nT)), \\ &= r_b(\alpha(\beta(nT)))\mathrm{e}^{-\mathrm{j}2\pi f_c(\beta(nT)-\alpha(\beta(nT)))} + \eta(\beta(nT)), \\ &= r_b\left(\beta(nT) - \frac{d(\beta(nT))}{c}\right)\mathrm{e}^{-\mathrm{j}2\pi f_c(\beta(nT)-\alpha(\beta(nT)))} \\ &\quad +\eta(\beta(nT)). \end{aligned} \tag{4.36}$$

In the next step, the phase distortion is compensated through the multiplication by $\mathrm{e}^{-\mathrm{j}2\pi f_c(nT-\beta(nT))}$:

$$\begin{aligned} \hat{r}(\beta(nT)) &= r_b\left(\beta(nT) - \frac{d(\beta(nT))}{c}\right)\mathrm{e}^{-\mathrm{j}2\pi f_c(nT-\alpha(\beta(nT)))} \\ &\quad +\eta(\beta(nT))\mathrm{e}^{-\mathrm{j}2\pi f_c(nT-\beta(nT))} \\ &= r_b\left(nT+\epsilon_n\right)\mathrm{e}^{\mathrm{j}2\pi f_c\epsilon_n} + \eta(\beta(nT))\mathrm{e}^{-\mathrm{j}2\pi f_c(nT-\beta(nT))}. \end{aligned} \tag{4.37}$$

4.3 A New Simplified Algorithm

As shown in the previous subsection, the algorithms from [44], [43] require the knowledge of all transmitted symbols for calculating the value of ϵ_n, in order to obtain an estimation for $\beta((n+1)T)$. However, for achieving high data throughput, the amount of pilot symbols must be as low as possible, implying that the number of pilot symbols should be minimized.

Besides the aforementioned motivation, the transmitted symbol might not be available at the receiver side for any other cause. Thus, we propose an algorithm simplification in order to address this issue.

Considering that we just have access to the value of ϵ_0, and that any other information regarding the other symbols are not available, we might employ $\epsilon_n = \epsilon_0$, leading to:

$$\dot{\beta}(n+1) = \dot{\beta}(n) - \mu\epsilon_0 \tag{4.38}$$

$$\beta(n+1) = \beta(n) + \dot{\beta}(n+1)T. \tag{4.39}$$

In the next subsection, we perform some analysis in order to check this algorithm feasibility.

4.3.1 Tracking Analysis

The objective of this section is to evaluate the previous proposed algorithm simplification. With this aim, we want to identify whether the estimated signal $\hat{r}(\beta(nT))$ actually represents the signal transmitted at time instant nT, and to calculate the maximum block length not incurring in errors in order to employ the lowest amount of pilot symbols as possible. To achieve this goal we consider that just the first symbol of the block is known, or equivalently that the value of ϵ_0 is given. In addition, we will assume an oversimplified situation where $\epsilon_n = \epsilon_0$ is kept constant in order to derive an upper bound to the number of iterations in which no extra pilot symbol is required to estimate ϵ_n. This way we can access the performance of this algorithm version in the estimation of the sampling instant.

Therefore, the previous shown algorithm update will be used:

$$\dot{\beta}(n+1) \;=\; \dot{\beta}(n) - \mu\epsilon_0 \tag{4.40}$$

$$\beta(n+1) \;=\; \beta(n) + \dot{\beta}(n+1)T. \tag{4.41}$$

In order to evaluate the algorithm performance under this assumption, it is required to check if the algorithm provides a good estimation of the function $\beta(nT)$. We consider that the symbol that is represented by $x(nT)$ is valid from the time instant $(2n-1)T/2$ up to $(2n+1)T/2$. Notice that $\hat{r}(\beta(nT))$ is a representation of the signal transmitted at nT if two constraints are satisfied. The first constraint is related to the signal phase. Considering a single-carrier system and a QPSK constellation, the remaining phase distortion must lie inside the interval:

$$\begin{array}{rcl} \theta - \dfrac{\pi}{4} & < 2\pi f_c \hat{\epsilon}_n + \theta < & \theta + \dfrac{\pi}{4}, \\ \dfrac{-1}{8f_c} & < \hat{\epsilon}_n < & \dfrac{1}{8f_c}. \end{array} \tag{4.42}$$

The second constraint is related to the sampling instant:

$$\begin{array}{rcl} (2n-1)T/2 & < nT + \hat{\epsilon}_n < & (2n+1)T/2 \\ \dfrac{-T}{2} & < \hat{\epsilon}_n < & \dfrac{T}{2} \end{array} \tag{4.43}$$

where $\hat{\epsilon}_n$ represents a measurement of ϵ_n obtained after the estimation of $\hat{r}(\beta(nT))$. It is important to highlight that in this discussion the value of $\hat{\epsilon}_n$ will be used only for analyzing the algorithm performance, and not for algorithm updating. As shown in Appendix D, the phase constraint prevails over the sampling constraint.

If the value of the error $\hat{\epsilon}_n$ is outside the bounds described by Eqs. (4.42), (4.43),

then the receiver missed the desired symbol and retained a sample representing another symbol, indicating that the algorithm is not producing a good estimate of $\beta(nT)$. Therefore, in order to keep the algorithm tracking accurately the sampling instant of the received signal, the algorithm must be restarted. This implies that a new set of pilot symbols should be transmitted in order to restart the algorithm. To address this issue, we determine the points in which the algorithm starts to estimate a value for $\beta(nT)$, such that the received signal $\hat{r}(\beta(nT))$ does not originate from the signal transmitted at time instant nT. According to Eqs. (4.40), (4.41), after deriving the evolution of $\beta(n+1|n)$ over time n and considering the knowledge of ϵ_0, $\beta(nT)$ can be written as

$$\beta(nT) = \beta(0) + \dot{\beta}(0)nT - \mu\epsilon_0 Tn\frac{(n+1)}{2}. \tag{4.44}$$

It is worth recalling that this expression represents the oversimplified case where $\epsilon_n = \epsilon_0$.

Without loss of generality, the transmitter is considered to be static, and just the receiver is moving. It is important to highlight that the case in which both transmitter and receiver are in movement can be mapped into the previous case, where just the receiver is in movement.

The receiver movement can be described as:

$$d(t) = d_0 + v_0 t + \frac{1}{2}m_0 t^2 + \frac{1}{6}b_0 t^3, \tag{4.45}$$

where d_0 is the initial distance between transmitter and receiver, v_0 is the initial velocity of the receiver, m_0 is the initial acceleration, and b_0 is a coefficient related to the acceleration. As

$$\epsilon_n = \alpha(\beta(nT)) - nT = \beta(nT) - \frac{d(\beta(nT))}{c} - nT, \tag{4.46}$$

and considering that just the estimation of ϵ_0 is available, a value for $\hat{\epsilon}_n$ can be obtained using Eq. (4.44). So, Eq. (4.46) can be rewritten as

$$\begin{aligned}\hat{\epsilon}_n \;=\; & \beta(0) + \dot{\beta}(0)nT - \mu\epsilon_0 Tn\frac{(n+1)}{2} - \frac{d_0}{c} \\ & - \frac{v_0\,[\beta(0) + \dot{\beta}(0)nT - \mu\epsilon_0 Tn\frac{(n+1)}{2}]}{c} \\ & - \frac{m_0\,[\beta(0) + \dot{\beta}(0)nT - \mu\epsilon_0 Tn\frac{(n+1)}{2}]^2}{2c} \\ & - \frac{b_0\,[\beta(0) + \dot{\beta}(0)nT - \mu\epsilon_0 Tn\frac{(n+1)}{2}]^3}{6c} - nT\end{aligned} \tag{4.47}$$

The solution of interest is described by the problem

$$\begin{aligned} &\max && n \\ &\text{subject to} && \hat{\epsilon}_n > \max\left(\tfrac{-1}{8f_c}, \tfrac{-T}{2}\right) \\ &&& \hat{\epsilon}_n < \min\left(\tfrac{1}{8f_c}, \tfrac{T}{2}\right) \end{aligned} \tag{4.48}$$

The next subsection describes the simulation implemented for this evaluation. The objective is to analyze the algorithm performance in order to find the maximum data sequence length that can be employed, such that all transmitted symbols can be perfectly recovered. Thus, the required amount of pilot symbols is minimized under this criteria, possibly yielding higher system throughput.

4.3.2 Implemented Simulation

The simulated system is the SC-FD described in Section 3.1. As stated before, the channel has a single path, unitary gain, and Doppler effect. As the Doppler effect has to be simulated in a higher rate $1/T_h$, the signal rate is increased before transmission. We assume the signal is repeated p times before transmission (to emulate an upsampling) and no filtering operation is performed. Notice that the relationship between the symbol period and the sample period is $T = T_h \cdot p$. Since the received signal is given by

$$r(t) = x(\alpha(t))\mathrm{e}^{\mathrm{j}2\pi f_c(t-\alpha(t))} + \eta(t), \tag{4.49}$$

the Doppler effect can be modeled using the relationship of the time instant that each symbol was received, t, and the time instant that the signal was transmitted: $\alpha(t)$. For simulating the Doppler effect, the following relationship is considered [43]

$$(t - \alpha(t))c = \|z_t(\alpha(t)) - z_r(t)\|_2 \tag{4.50}$$

where $z_t(\alpha(t))$ is the transmitter position at instant $\alpha(t)$, $z_r(t)$ is the receiver position at instant t, and $d(t) = \|z_t(\alpha(t)) - z_r(t)\|_2$ is the distance between transmitter and receiver.

In addition, the receiver has a sampling period of T_h s, whose samples are equally spaced: $t \in \{t_0, t_0 + T_h, \cdots, t_0 + p(N-1)T_h\}$. Therefore, the Doppler simulator calculates for all t, the corresponding time instant $\alpha(t)$, picking the signal transmitted at $\alpha(t)$ and attributes to the signal received at t. Besides, the effect of phase distortion $\mathrm{e}^{\mathrm{j}2\pi f_c(t-\alpha(t))}$ is also included in the signal received at t.

The signal is downsampled to the lower rate while attempting to compensate the Doppler effect. This effect is compensated in the following manner: as the receiver

has equally spaced samples of the received signal at the higher rate, it must choose the signal sample whose time of arrival t is as close as possible to $\beta(t)$. The phase drift is also removed from this signal using the same estimated parameter $\beta(t)$.

Simulation Results

The algorithm performance is analyzed under two distinct approaches. In the first approach, Eq. (4.48) is evaluated using the proper initialization parameters.In the second approach, the system described in the previous section is emulated (the Doppler effect is generated according to Eq. (4.49)).

The following parameters are used: the carrier frequency is $f_c = 20 \cdot 10^3$ Hz, the symbol duration is $T = 10^{-4}$ s. The period of each sample is $T_h = 10^{-4}/p$ s, $p = 30$, $d_0 = 0$ m, $m_0 = 0$ m/s^2, $b_0 = 0$ m/s^3, and $\mu = 0.01$. The sound speed is considered to be constant and equal to $c = 1500$ m/s. Here we transmitted just one block of symbols, the channel is considered known, and the sequence is perfectly synchronized.

For both approaches, if a perfect knowledge of the algorithm initialization parameters $\beta(0)$, $\dot{\beta}(0)$ and ϵ_0 is available, the tracking is lost after hundreds of thousands of symbols. Notice that the parameter $\beta(0)$ represents the perfect sampling instant of the first symbol, and can be obtained from the synchronization process. The parameter $\dot{\beta}(0)$ might be estimated with the knowledge of the sampling instant of the second symbol, $\beta(1)$, and the parameter ϵ_0 is computed as the argument between the first received symbol and the actual transmitted symbol, as shown in Eq.(4.22).

In this first simulation, we would like to analyze the algorithm performance for the case in which the parameter $\dot{\beta}(0)$ was estimated with a percentual error ξ, and also the case where the parameter ϵ_0 was computed from a signal corrupted with noise.

In Figure 4.1, the maximum sequence length is calculated using Eq. (4.48), and with an error ξ in the estimation of $\dot{\beta}(0)$ modeled as $(1 + \xi)\dot{\beta}(0)$. Besides, no noise were added in the received signal. Considering the same percentage error ξ in the initialization parameter $\dot{\beta}(0)$, the maximum sequence length is equal for distinct relative movements.

Figs. 4.2 and 4.3 show the computed value for $\hat{\epsilon}_n$ (using Eq. (4.47)) for a relative movement of $v_0 = 1.5$ m/s and $v_0 = 7$ m/s, respectively, considering an error of $\xi = 10^{-4}$ in the estimation of $\dot{\beta}(0)$. As observed from these figures, since the percentual error in $\dot{\beta}(0)$ is equal for the experiments, $\hat{\epsilon}_n$ assumes the same value for distinct relative movements. In addition, $\hat{\epsilon}_n$ exceeds the phase constraint boundary at $n = 626$ in both figures.

In order to analyze the algorithm performance under a noisy estimation of ϵ_0, another evaluation of Eq. (4.48) was performed. In this case, the first symbol was

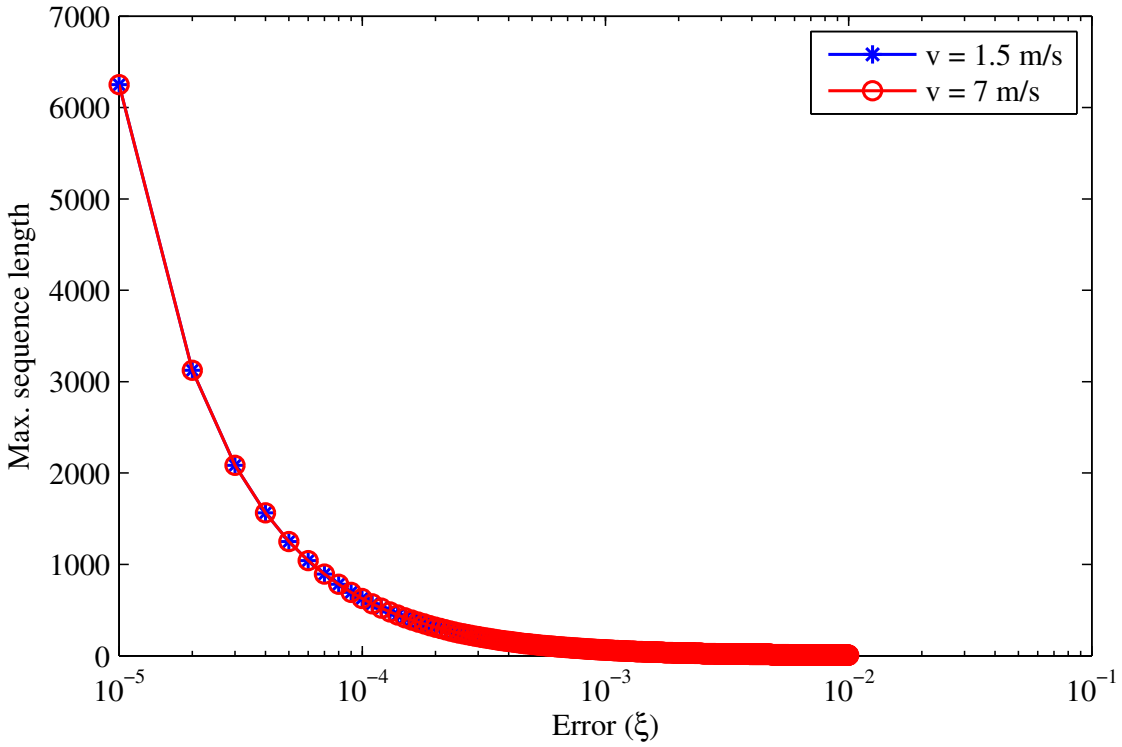

Figure 4.1: Maximum sequence length as a function of the error ξ.

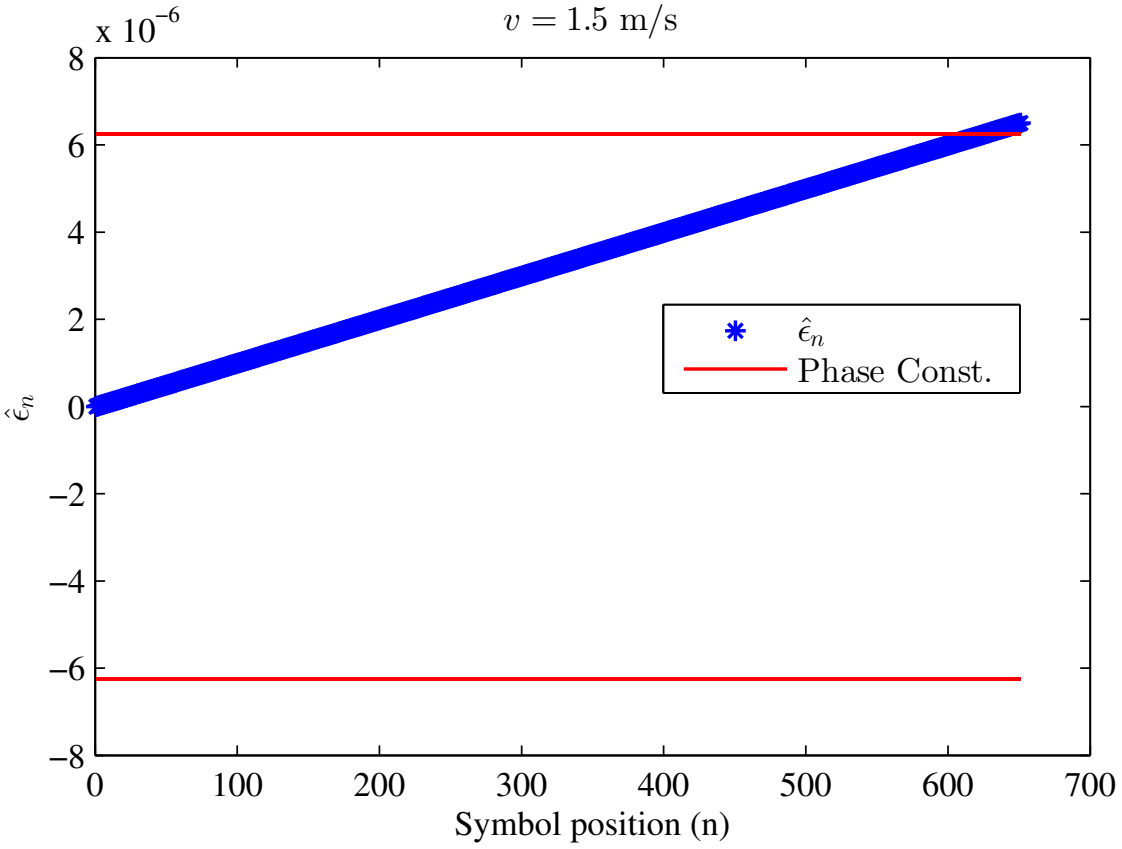

Figure 4.2: Measured value for $\hat{\epsilon}$ for each signal position n in a block for a relative movement of $v = 1.5$ m/s.

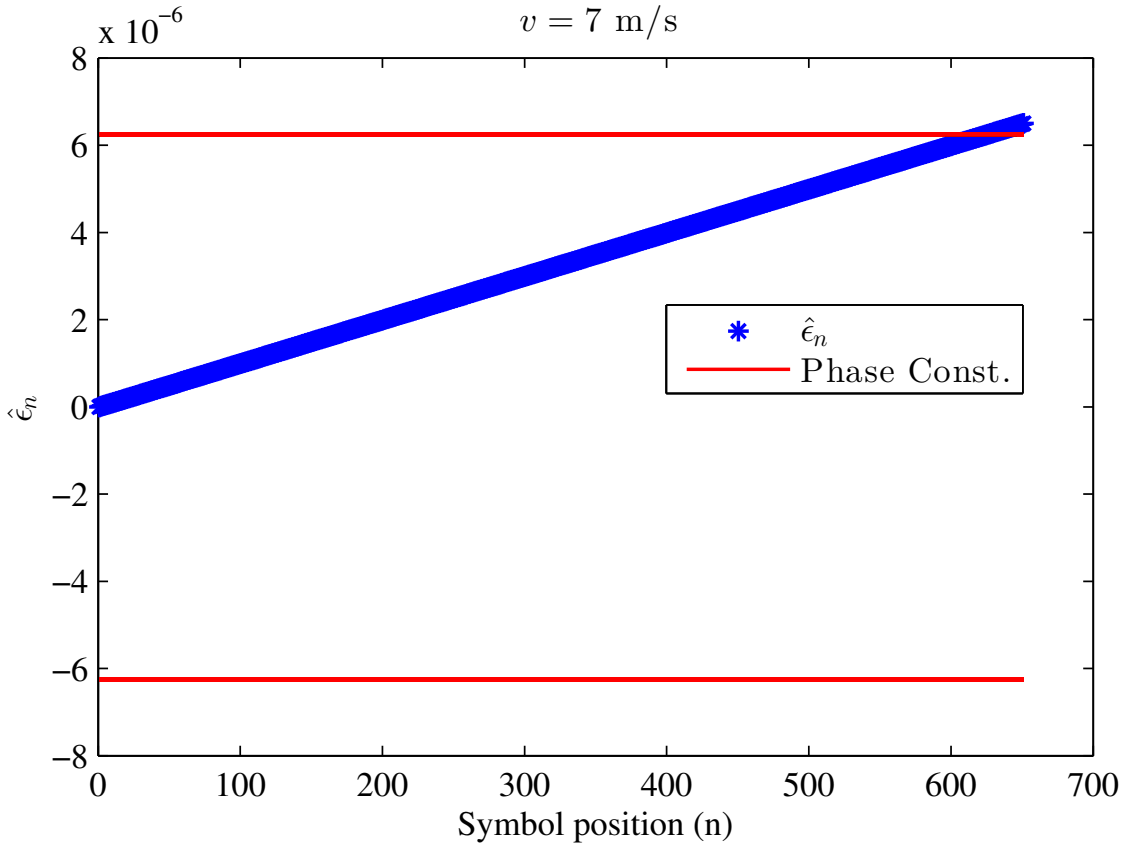

Figure 4.3: Measured value for $\hat{\epsilon}$ for each signal position n in a block for a relative movement of $v = 7$ m/s.

Table 4.1: Mean sequence length

	Mean Seq. Length
SNR = 10 dB	≈ 4500
SNR = 20 dB	≈ 8000
SNR = 30 dB	≈ 14000

corrupted with noise, leading to an error in the estimation of ϵ_0. As the received signal was buried in white Gaussian noise, the symbol position such that the value of $\hat{\epsilon}_n$ exceeds the phase boundary constraint is distinct in all simulation runs. The average sequence length was calculated with 1000 simulation runs. For a relative velocity $v \in \{0.5, 1, \cdots, 20\}$ m/s, the mean sequence length is nearly the same, whereas its values for distinct SNR's are shown in Table 4.1. From Table 4.1 one can infer that a higher SNR provides a more accurate estimation of ϵ_0, and consequently a higher average sequence length.

Another simulation considering both the error ξ in $\dot{\beta}(0)$ and the noisy estimation of ϵ_0 was implemented. Figure 4.4 shows the mean sequence length as a function of the error ξ for 10^5 simulation runs. As observed in Figure 4.4, a lower error in the initialization parameter $\dot{\beta}(0)$ leads to a higher average value for the sequence length. Once more, the average sequence length is approximately the same for all relative velocities. One can notice that in Figure 4.4 for certain range of values of ξ ($\xi \in \{3 \cdot 10^{-5}, 9 \cdot 10^{-5}\}$) the average sequence length is higher for a lower SNR. This behavior is justified through Eq. (4.47) rewritten here for convenience

$$\begin{aligned}\hat{\epsilon}_n &= \beta(0) + \dot{\beta}(0)nT - \mu\epsilon_0 Tn\frac{(n+1)}{2} - \frac{d_0}{c} \\ &\quad - \frac{v_0\ [\beta(0) + \dot{\beta}(0)nT - \mu\epsilon_0 Tn\frac{(n+1)}{2}]}{c} \\ &\quad - \frac{m_0\ [\beta(0) + \dot{\beta}(0)nT - \mu\epsilon_0 Tn\frac{(n+1)}{2}]^2}{2c} \\ &\quad - \frac{b_0\ [\beta(0) + \dot{\beta}(0)nT - \mu\epsilon_0 Tn\frac{(n+1)}{2}]^3}{6c} - nT. \end{aligned} \tag{4.51}$$

In order to understand the influence of the error in $\dot{\beta}(0)$ and in ϵ_0, we can write the

term related to these parameters as

$$\begin{aligned}
\chi &= (1+\xi)\dot{\beta}(0)nT - \mu\hat{\epsilon}_0 Tn\frac{(n+1)}{2} \\
&= (1+\xi)\dot{\beta}(0)nT - \mu(\epsilon_0+\tilde{\epsilon}_0)Tn\frac{(n+1)}{2} \\
&= \left[(1+\xi)\dot{\beta}(0) - \mu(\epsilon_0+\tilde{\epsilon}_0)\frac{(n+1)}{2}\right]nT \\
&= \left[\dot{\beta}(0) - \mu\epsilon_0\frac{(n+1)}{2} + \underbrace{\xi\dot{\beta}(0) - \mu\tilde{\epsilon}_0\frac{(n+1)}{2}}_{\chi_e}\right]nT+
\end{aligned} \tag{4.52}$$

whereas the symbol position such that the algorithm fails depends on the following term

$$\chi_e = \xi\,\dot{\beta}(0) - \mu\tilde{\epsilon}_0\frac{(n+1)}{2}. \tag{4.53}$$

As the mean value of $\tilde{\epsilon}_0$ (representing an angle) is lower for a higher signal-to-noise ratio, so for a certain range of values of ξ we might have

$$\chi_{e,\text{SNR=10dB}} < \chi_{e,\text{SNR=20dB}} \tag{4.54}$$

resulting in a higher average sequence length for the case where a lower SNR is employed.

A simulation considering the second approach[4] was implemented in order to verify the influence of the error ξ, of the noisy estimation of ϵ_0, and of the noise added to all the received symbols (not only on the first symbol as in Figure 4.4). Figure 4.5 shows the mean sequence length as a function of the error ξ in $\dot{\beta}(0)$ for 200 simulation runs. Comparing Figure 4.5 with Figure 4.4, one can note that the mean sequence length is lower for the case that all received symbols are embedded in noise. Besides, a higher SNR seems to influence more the mean sequence length for lower values of the error ξ. The mean sequence length is around the same for the cases in which the relative movements are distinct.

In the same simulation, the bit error rate was measured for each sequence length. The result for 1000 simulation runs is in Figure 4.6. From this figure, one can observe that higher SNR and lower ξ lead to higher mean sequence length. In addition, considering the same parameters ξ and SNR, the algorithm performance is approximately the same for both relative velocities.

From all these results, one can note that the algorithm initialization appears to be a crucial issue for system performance.

[4]In this approach, the Doppler effect is generated according to Eq. (4.49).

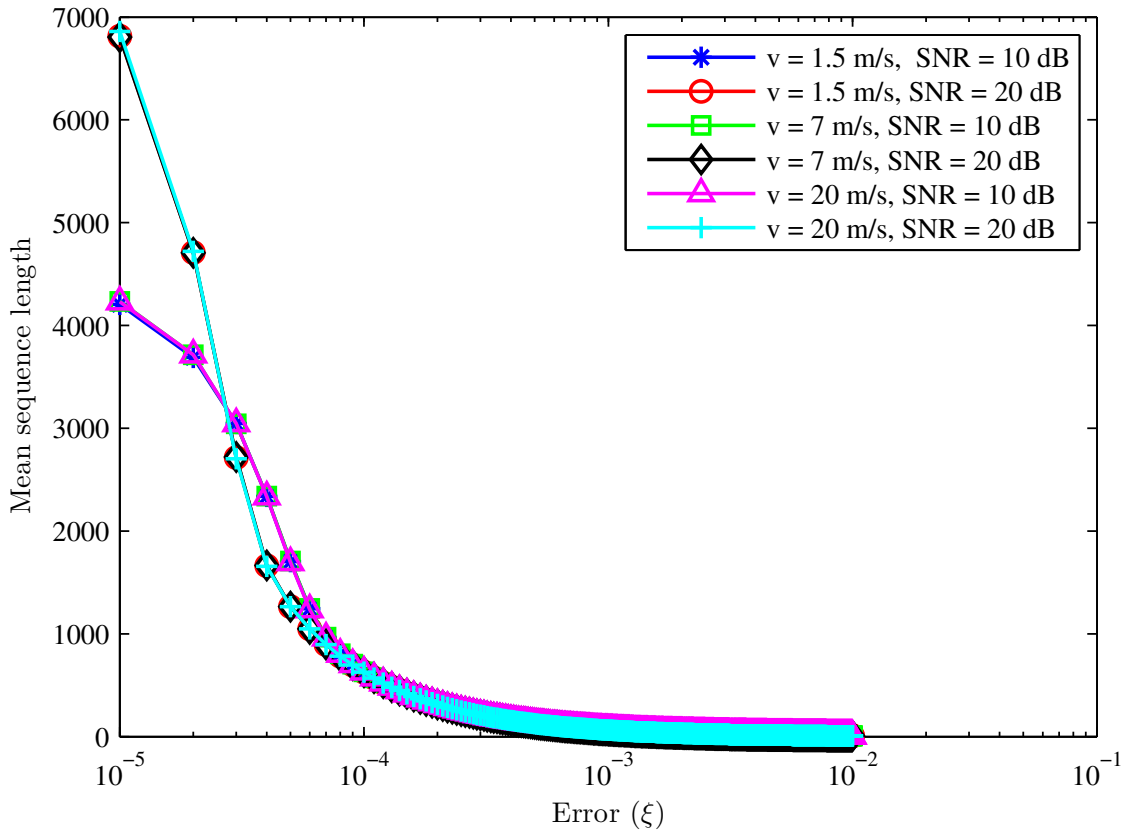

Figure 4.4: Mean sequence length as a function of the error ξ in $\dot{\beta}(0)$.

4.4 Conclusion

This chapter presented some analyses and discussions related to online algorithms to estimate the time warping function, inherent to communications systems facing high Doppler effect. We proposed a simplified version of an algorithm in order to reduce the amount of transmitted pilot symbols. It is observed that this algorithm version requires careful parameter initialization.

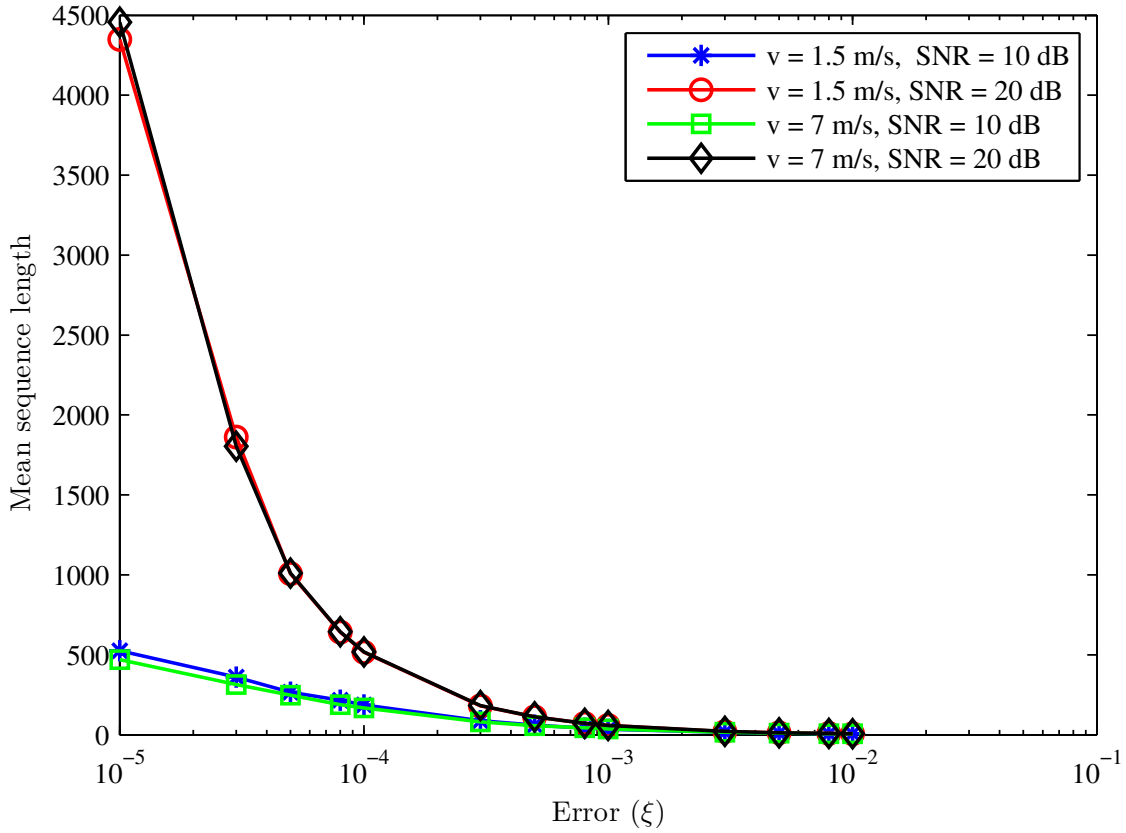

Figure 4.5: Mean sequence length as a function of the error ξ in $\dot{\beta}(0)$.

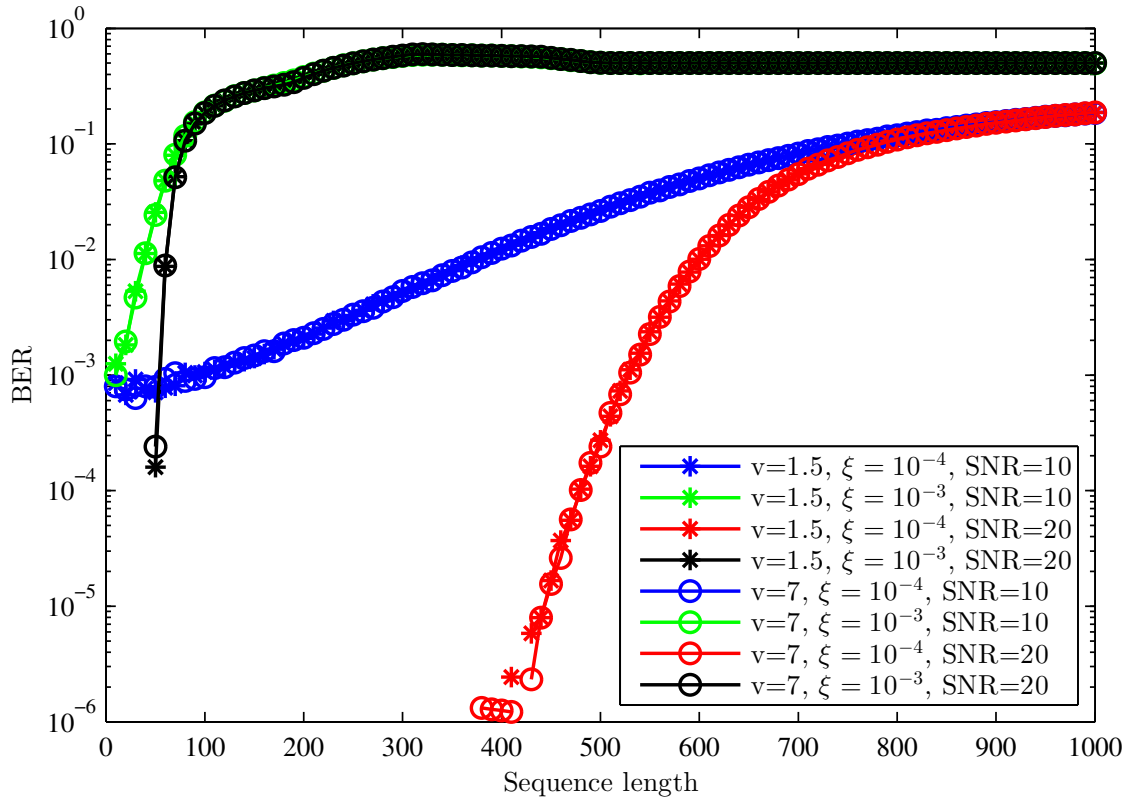

Figure 4.6: BER as a function of the sequence length.

Chapter 5

New Doppler Estimation and Compensation Techniques

In this chapter, we propose and present two distinct receivers along with their employed techniques to deal with Doppler effects. As our proposals merge the ideas of a cross-correlation filter bank with a tracking algorithm that resembles those in [43, 44], in addition to a redesign of some processing blocks, our approach is to describe step-by-step each proposed technique with simplified models.

In Section 5.1, we start our presentation with an analysis of how the Doppler effect distorts a baseband signal considering a single path channel without noise. Besides this analysis, we introduce the idea of iteratively adapting the correlator filter in order to reduce the intersymbol interference.

In Section 5.2, we consider a system model where the related signal is represented in passband, in order to evaluate how the signal is affected by Doppler effects. As the model of the received signal has time-dependent phase shift components, we propose to remove firstly its phase distortion. In Subsection 5.2.2, we show that this modification in the signal processing sequence blocks improves the symbol estimation.

In Section 5.3, we present a model that has a signal representation in passband, but with a multipath channel with Doppler effect equal in all paths. We provide an intuitive explanation showing that the previously proposed receiver modifications might work in this distinct environment. Section 5.4 summarizes the chapter.

5.1 Baseband System: Doppler Compensation for a Single Path Channel

In order to understand how the Doppler effect distorts the transmitted signal, we start our presentation with an analysis of a baseband system, which is depicted in

Figure 5.1. This system is composed of a pulse shaping block at the transmitter side, and of four distinct receiver types, that will be described afterwards.

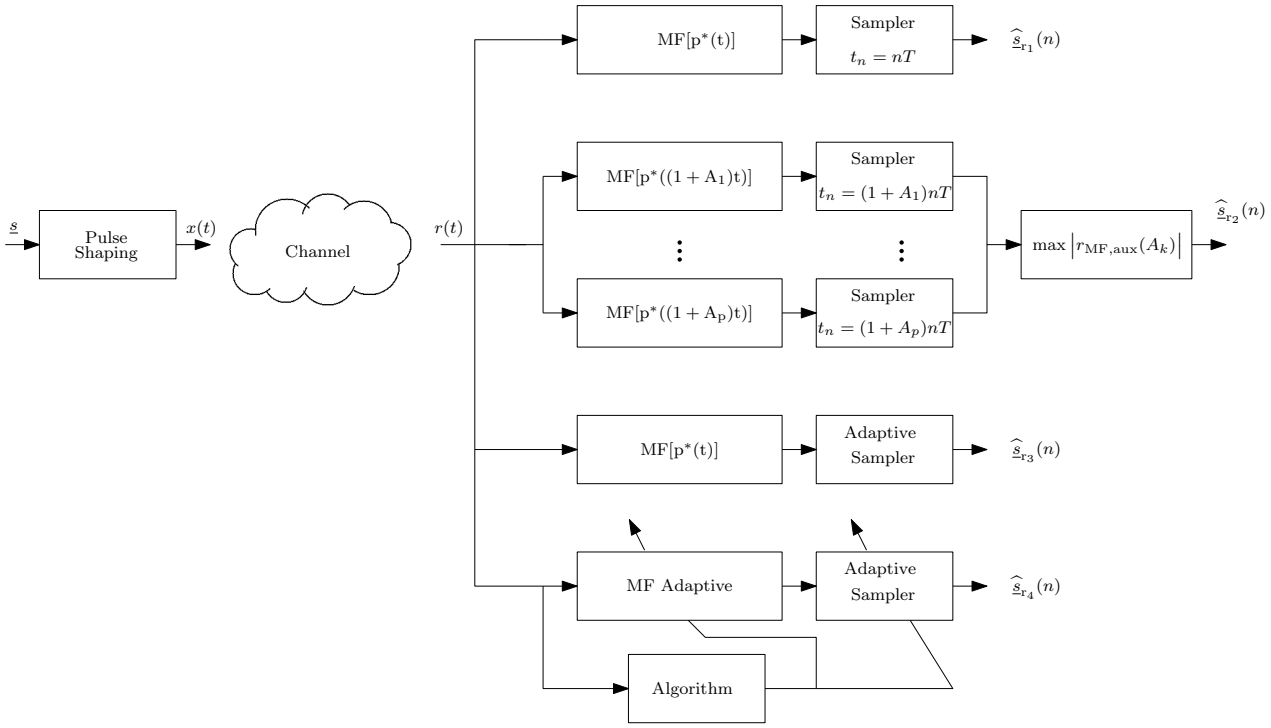

Figure 5.1: Baseband system model.

In Figure 5.1, $\underline{\boldsymbol{s}}$ represents a block with M symbols. Each symbol is mapped into a waveform

$$x(t) = \sum_{n=0}^{M-1} \underline{s}(n)p(t - nT), \tag{5.1}$$

where $p(t)$ is the basic pulse waveform, and T is the symbol period.

In case the signal is transmitted through a single-path and unitary channel, without noise, and is affected by the Doppler effect, it is described by the equation:

$$h(t, \tau) = 1 \cdot \delta(\tau - \tau(t)), \tag{5.2}$$

where the received signal assumes the model:

$$r(t) = x(t - \tau(t)) = \sum_{n=0}^{M-1} \underline{s}(n)p(t - \tau(t) - nT). \tag{5.3}$$

Notice that in this case, the equivalent received pulse suffered a time warping effect, generating change in the pulse duration.

5.1.1 Receiver Types

For analyzing the distortion of the received signal $r(t)$, we considered four distinct receiver types. Each receiver will be described and examined hereafter.

Receiver 1

The first receiver is a standard one, which is composed of a matched filter with the transmitted waveform, followed by an equally spaced sampler.

The signal at the matched filter output can be described by:

$$r_{\mathrm{MF,r_1}}(t) = r(t) * p_1(t), \tag{5.4}$$

with $p_1(t) = p^*(-t)$. After the filtering operation, the signal $r_{\mathrm{MF,r_1}}(t)$ passes through a sampler block, that performs the sampling operation: $t = nT$ for $n \in \{0, 1, \cdots, M-1\}$. The result is the estimated symbol:

$$\widehat{\underline{s}}_{\mathrm{r_1}}(n) \;\; = \;\; r_{\mathrm{MF,r_1}}(n) \tag{5.5}$$

Notice that the estimated symbol may suffer severe intersymbol interference (ISI) due to Doppler effect contained in the pulse waveform.

Receiver 2

The second receiver to be considered is a cross-correlator filter bank. Each branch of this bank is composed of a filter that is matched with a distinct warped version of the transmitted pulse. Each filter is followed by an equally spaced sampler, whose sample period is determined by the previous pulse distortion. The branch that yields the highest correlation is selected as having the desired parameters concerning the Doppler estimation effect.

The aforementioned processing is performed as follows. The operation performed by each matched filter can be described as

$$r_{\mathrm{MF,aux}}(A_k) = \int_0^{\frac{T}{(1+A_k)}} r(t)p^*((1+A_k)t)\mathrm{d}t, \tag{5.6}$$

where A_k is the pulse scaling factor. Eq. (5.6) is a modified version of the operation reported in [79], in which we modified the integration period from $t \in [0, T]$ to $t \in \left[0, \frac{T}{(1+A_k)}\right]$. Such a modification actually improves the related results.

The Doppler scale factor is chosen according to the criteria:

$$\hat{a} = \max_{1 \le k \le p} |r_{\mathrm{MF,aux}}(A_k)| \tag{5.7}$$

So, with this knowledge, the entire signal is processed with the selected time scaling:

$$r_{\mathrm{MF,r_2}}(t) = r(t) * p_2(t), \tag{5.8}$$

with $p_2(t) = p^*(-(1+\hat{a})t)$, and sampled at rate $t = (1/(1+\hat{a}))nT$, resulting in the estimated symbols:

$$\widehat{\underline{s}}_{\mathrm{r_2}}(n) \;=\; r_{\mathrm{MF,r_2}}((1/(1+\hat{a}))nT). \tag{5.9}$$

Receiver 3

The third receiver is an adaptation of the one in [43, 44]. It employs a filter that is matched with the transmitted pulse, and afterwards, it performs an adaptive sampling.

The signal at the matched filter output is the same as the one of Eq. (5.4)

$$r_{\mathrm{MF,r_3}}(t) = r_{\mathrm{MF,r_1}}(t). \tag{5.10}$$

The distinction of this receiver to Receiver 1, is related to the sampling strategy. This receiver employes an adaptive sampling, whose idea was discussed in Chapter 4. The sampling instant $t = \beta(n)$ is calculated for estimating each symbol using the idea of the algorithm of [43, 44] as

$$\dot{\beta}(n) \;=\; \dot{\beta}(n-1) - \mu\epsilon_{n-1} \tag{5.11}$$

$$\beta(n) \;=\; \beta(n-1) + \dot{\beta}(n)T. \tag{5.12}$$

It is important to highlight that in this case we do not update the parameter ϵ_{n-1}, because we consider that we do not have access in any iteration to the original transmitted signal, resulting in $\epsilon_{n-1} = 0$. This adaptation is a simplified version of the original algorithm, leading to

$$\dot{\beta}(n) \;=\; \dot{\beta}(n-1) \tag{5.13}$$

$$\beta(n) \;=\; \beta(n-1) + \dot{\beta}(n)T, \tag{5.14}$$

where the variable $\dot{\beta}(1)$ can be obtained from synchronization. The symbol estimation is given by

$$\widehat{\underline{s}}_{\mathrm{r_3}}(n) \;=\; r_{\mathrm{MF,r_3}}(\beta(n)). \tag{5.15}$$

Receiver 4

The fourth receiver, which is our proposal, employs an adaptive filter followed by an adaptive sampler, whereas both blocks utilize the same calculated parameters.

As the received signal $r(t)$ was distorted by the Doppler effect, the filter employed in Eq. (5.4) is not matched anymore with the received pulse. Knowing that the matched filter is the optimum receiver in the sense of maximizing the peak pulse signal-to-noise ratio [85] at time instant $t = nT$, it would be desirable to process the received signal with this filter. With this objective, the filter at the receiver side could be adapted taking into account the received pulse distortion. In other words, if we have an adaptive matched filter, proceeded by an adaptive sampler, we would have access to a better symbol estimation. This idea is depicted in Figure 5.2.

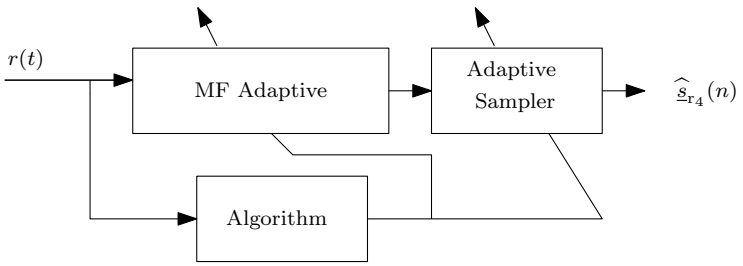

Figure 5.2: Receiver 4.

Notice that the algorithm of Eq. (5.11) is proposed to be an adaptive sampler. Hence, it would be desirable to use the same calculated parameters for adapting the filter at the receiver side. This algorithm is repeated here for convenience

$$\dot{\beta}(n+1) = \dot{\beta}(n) - \mu\epsilon_n \tag{5.16}$$

$$\beta(n+1) = \beta(n) + \dot{\beta}(n+1)T. \tag{5.17}$$

As mentioned before, $\beta(n+1)$ represents the sampling moment such that the $(n+1)$-th transmitted symbol should be sampled. By knowing that the previous symbol was sampled at $\beta(n)$, the new period of the $(n+1)$-th symbol is given by

$$T_{new} = \beta(n+1) - \beta(n) = \dot{\beta}(n+1)T. \tag{5.18}$$

With this knowledge, the filter at the receiver side can be adapted as

$$p((\beta(n+1) - \beta(n))T - t), \tag{5.19}$$

where this filter can be interpret as a warped version of the original pulse shaping $p(t)$. Notice that the pulse parameters have to be updated for processing each

symbol, that is

$$r_{\mathrm{MF,r_4}}(t) = r(t) * p_4(t) \tag{5.20}$$

with $p_4(t) = p^*((\beta(n+1) - \beta(n))T + t)$. At each algorithm iteration, the pulse is first adapted, then the signal is convolved with this adapted pulse, and then it is sampled at $t = \beta(n+1)$

$$\hat{r}_{\mathrm{MF,r_4}}(\beta(n+1)) = r_{\mathrm{MF,r_4}}(t = \beta(n+1)), \tag{5.21}$$

resulting in the estimated symbol

$$\widehat{\underline{s}}(n+1) = \hat{r}_{\mathrm{MF,r_4}}(\beta(n+1)) = \underline{s}(n+1) + \xi_{n+1}, \tag{5.22}$$

where ξ_{n+1} accounts for the adaptive filter inaccuracies.

The expected benefit of using this adaptive filter is to reduce the inter-symbol interference (ISI).

5.1.2 Practical Considerations

In order to implement a discrete processing version and evaluate the receiver strategies shown in the previous subsection, some practical considerations need to be mentioned. The transmitter and the receiver in Figure 5.1 operate at two distinct data rates. The first one is the symbol rate denoted by T, whereas the second is the sample rate t_s. The relationship between these two data rates is the following

$$T = sps \cdot t_s, \tag{5.23}$$

with *sps* stating for samples per symbol, i.e., the number of samples that represents one symbol[1]. The system block that performs the conversion between these two sample rates is the pulse shaping operation. In the process of pulse shaping, each symbol is transformed into another sequence of numbers. This operation requires a pulse (filter) that satisfies the Nyquist criterion to achieve a distortionless transmission [85].

The pulse squared root-raised cosine (SRRC) satisfies the Nyquist criterion, and

[1]The transmitter and receiver of underwater equipment might operate with this two distinct data rates.

is described by the equation

$$p(t) = \begin{cases} \frac{1}{T}\left(1+\alpha(\frac{4}{\pi}-1)\right), & t=0 \\ \frac{\alpha}{T\sqrt{2}}\left[\left(1+\frac{2}{\pi}\right)\sin\left(\frac{\pi}{4\alpha}\right)+\left(1-\frac{2}{\pi}\right)\cos\left(\frac{\pi}{4\alpha}\right)\right], & t=\pm\frac{T}{4\alpha} \\ \frac{1}{T}\dfrac{\sin\left[\pi\frac{t}{T}(1-\alpha)\right]+4\alpha\frac{t}{T}\cos\left[\pi\frac{t}{T}(1+\alpha)\right]}{\pi\frac{t}{T}\left[1-\left(4\alpha\frac{t}{T}\right)^2\right]}, & \text{otherwise} \end{cases}, \quad (5.24)$$

where α is the roll-off factor, and T is the symbol period. The SRRC has to be windowed in order to have a limited time support. Regarding this issue, there is a parameter called filter span (F_{span})

$$t \in \{-T\,F_{\text{span}}/2,\ \ T\,F_{\text{span}}/2\} \quad (5.25)$$

that establishes the duration of the pulse SRRC, through the windowing operation. Notice that the this parameter controls the amount of ISI that will be inserted in the signal. The usage of an SRRC at the transmitter and of an SRRC at the receiver, followed by a proper sampling strategy, enables a decoding without ISI for a non frequency-selective channel.

Thus, here we will represent the pulse as its discrete version $p(m)$

$$m \in \{-sps\,t_s\,F_{\text{span}}/2, \cdots, -t_s, 0, t_s, \cdots\ \ sps\,t_s\,F_{\text{span}}/2\}\,. \quad (5.26)$$

For the sake of clarity, the pulse SRRC will be shifted so that we can assume

$$m \in \{0, t_s, 2t_s, \cdots, sps\,t_s\,F_{\text{span}}\}\,. \quad (5.27)$$

Besides the selection of a proper pulse shaping function, the fourth receiver, which has an adaptive filter, requires special attention in the practical implementation because the received signal is at discrete domain. In other words, the new period of the adaptive filter described by Eq. (5.18) and the sampling point $t = \beta(n)$ were proposed considering a signal in the continuous domain. As we are dealing with discrete signals, this data might not be available. Knowing that the information contained in even closer time instant samples might contain ISI, we propose and investigate some rounding possibilities for the number of samples within a data period, and for the sampling point. For elucidating these problems, we will construct a toy example.

Illustrative Example:

In this example, we consider a signal transmitted in an SRRC pulse containing a filter span of 3 symbols ($F_{\text{span}} = 3$), and $sps = 20$, i.e., one pulse SRRC lasts for 61 samples. The Doppler effect induced an increment in the symbol period (T_{new}) of the received signal $r(t)$, leading to a duration of $sps_{\text{new}} = 20.2$ samples, and a new pulse duration of $T_{SRRC,\text{new}} = 20.3 \cdot 3 + 1 = 61.6$ samples.

The first problem that arises is: should we use 61 or 62 samples in the receiver pulse? For addressing this issue, we investigate these rounding possibilities.

The second problem is related to the sampling point. After convolving the received signal with the adapted pulse, just one sample of this signal is selected for representing the symbol. In this example, the calculated sample point of the first symbol has index 61.6. Once more, should we use the signal sample with index $k = 61$ or $k = 62$? Could we do a combination of these two samples for increasing precision and reducing ISI?

Besides the aforementioned aspects, could we perform another processing for improving system performance?

In order to address all these issues, we developed and evaluated four algorithms that have distinctions concerning the following aspects:

- Pulse shaping: as the new symbol period might not be a multiple of the sample period t_s, some rounding possibilities for the number of samples within a data period are investigated, as well as modifications in some pulse samples;
- Sampling point: once more, some rounding strategies for the number of samples within a data period are developed and applied in the signal $r_{\text{MF,r}_4}(t)$[2];
- Received signal $r(t)$: as we only have access to the samples of the signal $r(t)$ for $t \in \{0, t_s, 2t_s, \cdots\}$, some modifications might be performed in some of these samples[3]. We will refer to the received signal $r(t)$ sampled at rate $t = kt_s$, with $k \in \{0, 1, 2, \cdots\}$ as $r(k)$.

In order words, we propose and evaluate distinct algorithms, for understanding and for being able to gather the maximum amount of information as possible from the received signal $r(t)$, regarding the n-th symbol.

Algorithm 1

In the first algorithm, the number of samples which composes the pulse SRRC is rounded to the nearest integer number as

$$\text{m}_{\text{round}} = \lfloor F_{\text{span}}\, T_{new}/t_s \rceil = \lfloor F_{\text{span}}\, \left(\beta(n) - \beta(n-1)\right)/t_s \rceil\,, \tag{5.28}$$

[2] $r_{\text{MF,r}_4}(ts)$ is the signal at the output of the designed matched pulse filter.
[3] $r(t)$ is the signal at a previous stage of the adaptive correlation filtering block.

leading to the vector $\boldsymbol{p}_{\mathrm{r}}$, whereas each element can be expressed as $p_{\mathrm{r}}(m)$, with $m \in \{0, t_s, 2t_s, \cdots, \mathrm{m}_{\mathrm{round}} t_s\}$.

Besides, two sampling points representing the sampling position inside the vector $\boldsymbol{r}_{\mathrm{MF}}$ are selected according to the following criteria:

$$\begin{aligned} \hat{\beta}_{\mathrm{c}}(n) &= \lceil \beta(n)/ts \rceil \\ \hat{\beta}_{\mathrm{f}}(n) &= \lfloor \beta(n)/ts \rfloor, \end{aligned}$$

where $\lceil \beta(n)/ts \rceil$ rounds towards the nearest integer greater than or equal to $\beta(n)/ts$, while $\lfloor \beta(n)/ts \rfloor$ rounds towards the nearest integer lower than or equal to $\beta(n)/ts$.

The purpose of Algorithm 1 is estimate the symbol $\underline{\widehat{s}}(n)$ according to the following procedure

$$\begin{aligned} \boldsymbol{r}_{\mathrm{MF}} &= \boldsymbol{r} * \boldsymbol{p}_{\mathrm{r}} \\ \underline{\widehat{s}}_{\mathrm{alg_1}}(n) &= w_{\mathrm{c}}(n) \cdot r_{\mathrm{MF}}(\hat{\beta}_{\mathrm{c}}(n)) + w_{\mathrm{f}}(n) \cdot r_{\mathrm{MF}}(\hat{\beta}_{\mathrm{f}}(n)), \end{aligned} \tag{5.29}$$

where $w_{\mathrm{c}}(n)$ and $w_{\mathrm{f}}(n)$ are weights. Notice that we would like to have access to the information of the time instant $\beta(n)/ts$. Although, as we are dealing with discrete signals, this data might not be available. Knowing that the information contained in the previous time instant and in the following time instant contains ISI, we select the two closest time instant data. We perform a weighted average on them in order to minimize the ISI effects contained in each sampling points. In this algorithm, we select the information whose time instant is immediately bellow ($\hat{\beta}_{\mathrm{f}}(n)$) and above ($\hat{\beta}_{\mathrm{c}}(n)$) the perfect time instant $\beta(n)/ts$. As these two data are related to the desired information, we perform an weighted average of these two data. Each data will receive a weight that is proportional to the time distance between the original sampling point and the sampling point of the other selected signal as

$$\begin{aligned} w_{\mathrm{c}}(n) &= \left| \beta(n)/ts - \hat{\beta}_{\mathrm{f}}(n) \right| \\ w_{\mathrm{f}}(n) &= \left| \beta(n)/ts - \hat{\beta}_{\mathrm{c}}(n) \right|. \end{aligned}$$

Notice that $w_{\mathrm{c}}(n) + w_{\mathrm{f}}(n) = 1$.

Illustrative Example:

For elucidating the idea of Algorithm 1, and to clarify the distinction between this algorithm and the other ones that will be proposed further ahead, we will construct a toy example.

Considering a SRRC pulse with a filter span of 3 symbols ($F_{\mathrm{span}} = 3$), and $sps = 20$, i.e., one pulse SRRC lasts for 61 samples. The Doppler effect induced an increase in the symbol period (T_{new}), leading to a symbol duration of $sps_{\mathrm{new}} = 20.2$

samples, and a new pulse duration of $T_{SRRC,\text{new}} = 20.3 \cdot 3 + 1 = 61.6$.

Running the above algorithm, we obtain $\text{m}_{\text{round}} = 61$, what leads to a pulse duration of 62 samples. For illustrating the algorithm procedure, we will show the calculus of the second symbol. Notice that the perfect initial time instant that the SRRC pulse should gather information from the signal $r(k)$, would be $r(20.2)$, while the perfect last time instant would be the signal sample with index $k = 81.8$. As the receiver does not have access to those samples, one should decide how to proceed.

In case of Algorithm 1, this procedure is depicted in Figure 5.3. In this figure, we illustrate the calculus of $r_{\text{MF}}(\hat{\beta}_{\text{c}}(n))$ and $r_{\text{MF}}(\hat{\beta}_{\text{f}}(n))$. The received signal $r(\cdot)$ is convolved with an SRRC pulse whose length is 62 ($\text{m}_{\text{round}} = 61$), leading to the signal $r_{\text{MF}}(\cdot)$. From this signal, we selected the samples $r_{\text{MF}}(\hat{\beta}_{\text{f}}(n)) = r_{\text{MF}}(81)$ and $r_{\text{MF}}(\hat{\beta}_{\text{c}}(n)) = r_{\text{MF}}(82)$. Pursuing these values, the symbol is estimated with Eq. (5.29). The weights $w_{\text{f}}(2)$ and $w_{\text{c}}(2)$ are calculated as

$$\begin{aligned} w_{\text{c}}(2) &= |81.8 - 81| = 0.8 \\ w_{\text{f}}(2) &= |81.8 - 82| = 0.2. \end{aligned}$$

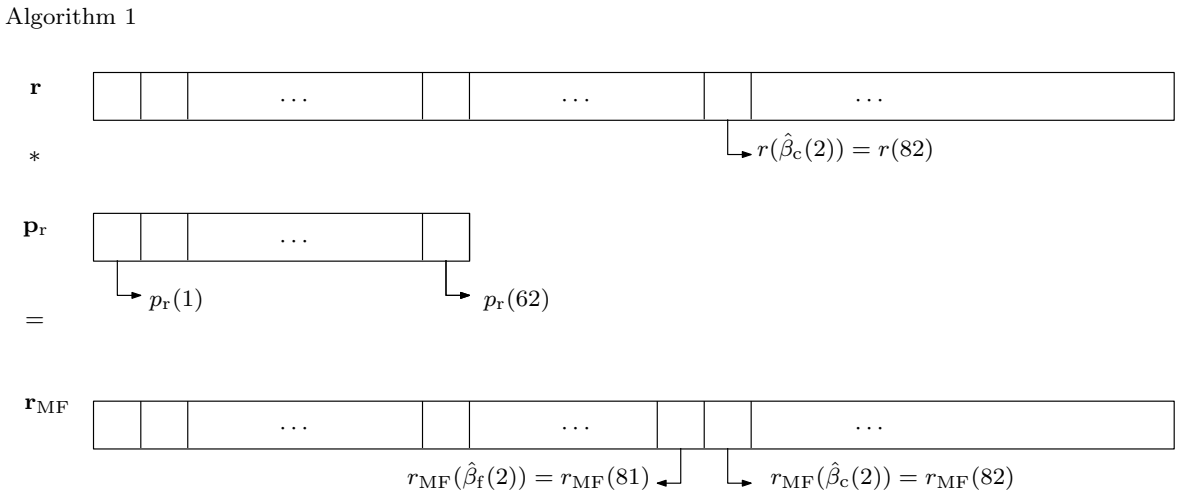

Figure 5.3: Procedure for performing the estimation of the second symbol with Algorithm 1.

Algorithm 2

In this second algorithm, the pulse SRRC is designed twice, whereas each pulse assumes a distinct length according to the criteria

$$\text{m}_{\text{ceil}} = \lceil F_{\text{span}}\, T_{new}/t_s \rceil = \lceil F_{\text{span}}\, (\beta(n) - \beta(n-1))\, /t_s \rceil\,, \tag{5.30}$$

$$\text{m}_{\text{floor}} = \lfloor F_{\text{span}}\, T_{new}/t_s \rfloor = \lfloor F_{\text{span}}\, (\beta(n) - \beta(n-1))\, /t_s \rfloor\,, \tag{5.31}$$

leading respectively to the vectors $\boldsymbol{p}_{\rm c}$, $\boldsymbol{p}_{\rm f}$ whereas each element is expressed as $p_{\rm c}(m)$, with $m \in \{0, t_s, 2t_s, \cdots, {\rm m}_{\rm ceil} t_s\}$, and as $p_{\rm f}(m)$, with $m \in \{0, t_s, 2t_s, \cdots, {\rm m}_{\rm floor} t_s\}$.

The selection of the sampling points follows the same criteria of the previous algorithm

$$\begin{aligned} \hat{\beta}_{\rm c}(n) &= \lceil \beta(n)/ts \rceil \\ \hat{\beta}_{\rm f}(n) &= \lfloor \beta(n)/ts \rfloor , \end{aligned}$$

whereas the sampling $\hat{\beta}_{\rm c}(n)$ is selected at the output of the filter $p_{\rm c}(m)$, and the point $\hat{\beta}_{\rm f}(n)$ from the filter $p_{\rm f}(m)$. In the next step, a weighted combination of these two signals is performed.

The algorithm 2 can be summarized as

$$\begin{aligned} \boldsymbol{r}_{\rm MF,c} &= \boldsymbol{r} * \boldsymbol{p}_{\rm c} \\ \boldsymbol{r}_{\rm MF,f} &= \boldsymbol{r} * \boldsymbol{p}_{\rm f} \\ \widehat{\underline{s}}_{\rm alg_2}(n) &= w_{\rm c}(n) \cdot r_{\rm MF,c}(\hat{\beta}_{\rm c}(n)) + w_{\rm f}(n) \cdot r_{\rm MF,f}(\hat{\beta}_{\rm f}(n)), \end{aligned} \tag{5.32}$$

where $w_{\rm c}(n)$ and $w_{\rm f}(n)$ are weights. Notice that in this algorithm, we employ two SRRC filters with distinct lengths, i.e. $\boldsymbol{p}_{\rm c}$ and $\boldsymbol{p}_{\rm f}$, in order to perform a combination of their output for obtaining a symbol estimation. The weights are calculated as

$$\begin{aligned} w_{\rm c}(n) &= \left| \beta(n)/ts - \hat{\beta}_{\rm f}(n) \right| \\ w_{\rm f}(n) &= \left| \beta(n)/ts - \hat{\beta}_{\rm c}(n) \right| . \end{aligned}$$

Observe that the weights are proportional to the time distance between the original sampling point ($\beta(n)/ts$) and the selected sampling point ($\hat{\beta}_{\rm f}(n)$ and $\hat{\beta}_{\rm f}(n)$).

Illustrative Example:

The goal of this example is to elucidate the idea of Algorithm 2. We consider the same parameters from the previous example, i.e., filter span of 3 symbols ($F_{\rm span} = 3$), and $sps = 20$, with a Doppler effect that induces a new pulse duration of $T_{SRRC,{\rm new}} = 20.3 \cdot 3 + 1 = 61.6$.

Evaluating Algorithm 2, we get ${\rm m}_{\rm ceil} = 61$, ${\rm m}_{\rm floor} = 60$, leading to two distinct pulses SRRC, whose duration are 62, 61 respectively. The procedure performed by Algorithm 2 for the calculation of the second symbol is shown in Figure 5.4.

In this figure, we first illustrate the calculus of the signal $r_{\rm MF,c}(\cdot)$, which is resulted from the convolution of the received signal $r(\cdot)$ with the pulse $\boldsymbol{p}_{\rm c}$, whose length is 62, following by the selection of the sampling point $r_{\rm MF,c}(\hat{\beta}_{\rm c}(n)) = r_{\rm MF,c}(82)$. At the same figure, we also illustrate the computation of the signal $r_{\rm MF,f}(\cdot)$ and the selection of the sampling point $r_{\rm MF,f}(\hat{\beta}_{\rm f}(n)) = r_{\rm MF,f}(81)$.

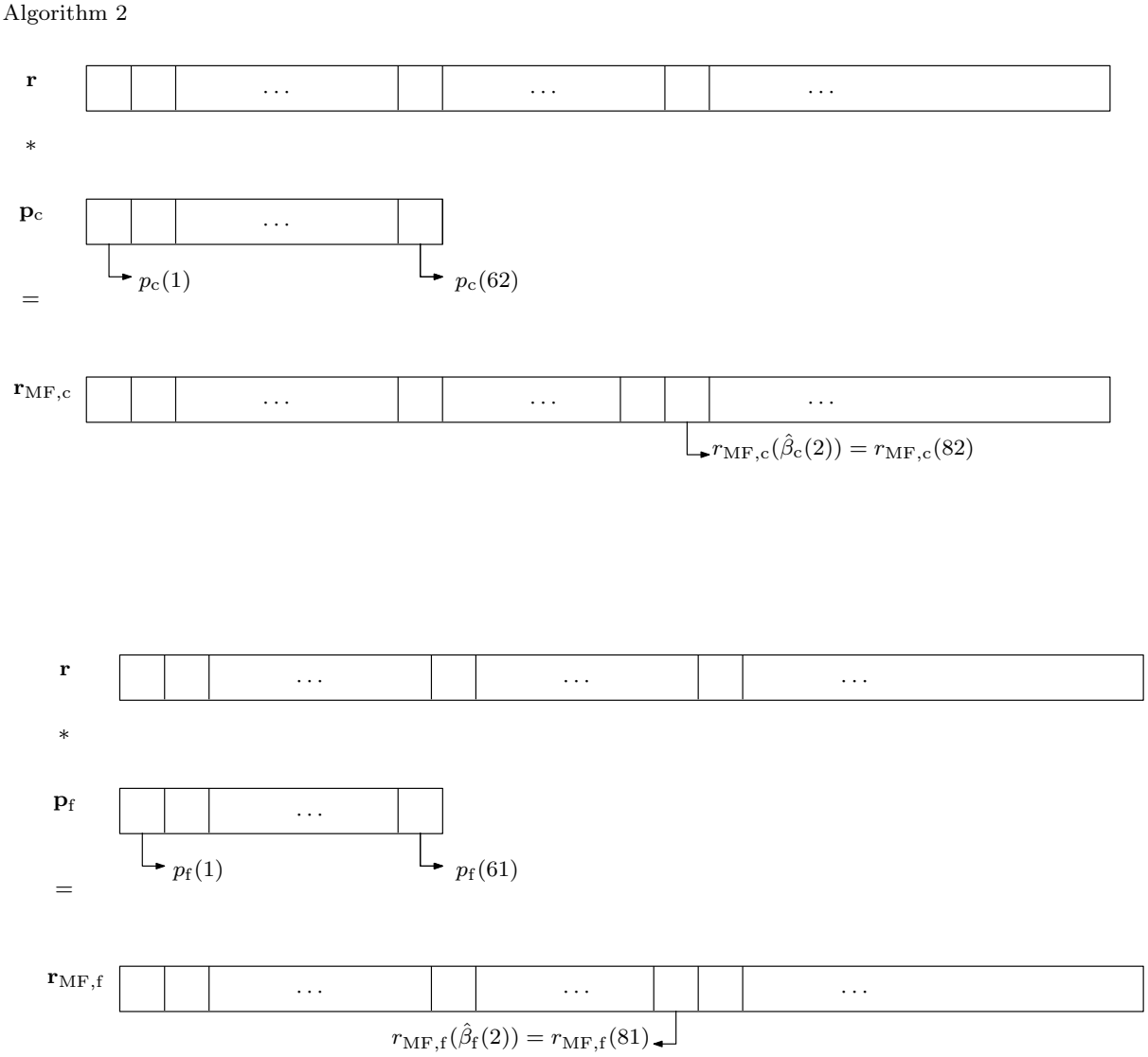

Figure 5.4: Procedure for performing the estimation of the second symbol with Algorithm 2.

Knowing the values of $r_{\mathrm{MF,c}}(\hat{\beta}_{\mathrm{c}}(n))$ and $r_{\mathrm{MF,f}}(\hat{\beta}_{\mathrm{f}}(n))$, the symbol estimation is performed with Eq. (5.32). The weights $w_{\mathrm{c}}(2)$ and $w_{\mathrm{f}}(2)$ employed in this case are calculated as

$$\begin{aligned} w_{\mathrm{c}}(2) &= |81.8 - 81| = 0.8 \\ w_{\mathrm{f}}(2) &= |81.8 - 82| = 0.2. \end{aligned}$$

Algorithm 3

In the third algorithm, another combination of the aforementioned 3 aspects is performed. In this case, the number of samples of the pulse SRRC is computed as

$$\begin{aligned} \mathrm{m}_{\mathrm{ceil}} &= \lceil F_{\mathrm{span}}\, T_{new}/t_s \rceil = \lceil F_{\mathrm{span}}\ (\beta(n) - \beta(n-1))\,/t_s \rceil\,, & (5.33)\\ \mathrm{m}_{\mathrm{floor}} &= \lfloor F_{\mathrm{span}}\, T_{new}/t_s \rfloor = \lfloor F_{\mathrm{span}}\ (\beta(n) - \beta(n-1))\,/t_s \rfloor\,, & (5.34) \end{aligned}$$

leading respectively to the vectors $\boldsymbol{p}_{\mathrm{c}}$, $\boldsymbol{p}_{\mathrm{f}}$ whereas each element is expressed as $p_{\mathrm{c}}(m)$, with $m \in \{0, t_s, 2t_s, \cdots, \mathrm{m}_{\mathrm{ceil}} t_s\}$, and to $p_{\mathrm{f}}(m)$, with $m \in \{0, t_s, 2t_s, \cdots, \mathrm{m}_{\mathrm{floor}} t_s\}$.

In this algorithm, we consider four distinct combinations of the parameters, which are shown into two parts. Each part contains the idea of having a pair of complementary signals. The algorithm of the first part is

$$\begin{aligned} \boldsymbol{r}_{\mathrm{MF,f}} &= \boldsymbol{r} * \boldsymbol{p}_{\mathrm{f}} & (5.35)\\ \underline{\widehat{s}}_{\mathrm{alg}_{3,1}}(n) &= w_{\mathrm{c},1}(n)\ \cdot r_{\mathrm{MF,f}}(\hat{\beta}_{\mathrm{c}}(n)) + w_{\mathrm{f},1}(n)\ \cdot r_{\mathrm{MF,f}}(\hat{\beta}_{\mathrm{f}}(n)), & (5.36) \end{aligned}$$

where $w_{\mathrm{c},1}(n)$, $w_{\mathrm{f},1}(n)$ are weights. In the first part of this algorithm, we use a pulse whose length is strictly lower than the original value, in order to be able to gather an edge sample (the first one or the last one) that has no information of the adjacent symbol. Notice that this first part performs a weighted average of the sampling point $r_{\mathrm{MF,f}}(\hat{\beta}_{\mathrm{f}}(n))$ and $r_{\mathrm{MF,f}}(\hat{\beta}_{\mathrm{c}}(n))$, and these sampling points correspond to the convolution of the pulse $\boldsymbol{p}_{\mathrm{f}}$ with a signal whose first and last points are respectively $\hat{\beta}_{\mathrm{f}}(n - F_{\mathrm{span}} + 1)$ and $\hat{\beta}_{\mathrm{f}}(n)$, $\hat{\beta}_{\mathrm{c}}(n - F_{\mathrm{span}} + 1)$ and $\hat{\beta}_{\mathrm{c}}(n)$.

The weight $w_{\mathrm{c},1}(n)$ is calculated as

$$\begin{aligned} w_{\mathrm{c},1}(n) &= (w_{\mathrm{c},1,\mathrm{init}}(n) + w_{\mathrm{c},1,\mathrm{end}}(n))\,/2\\ w_{\mathrm{c},1,\mathrm{init}}(n) &= \left|\beta(n - F_{\mathrm{span}} + 1)/ts - \hat{\beta}_{\mathrm{f}}(n - F_{\mathrm{span}} + 1)\right|\\ w_{\mathrm{c},1,\mathrm{end}}(n) &= \left|\beta(n)/ts - \hat{\beta}_{\mathrm{f}}(n)\right|, \end{aligned}$$

and $w_{\mathrm{f},1}(n)$ as

$$\begin{aligned} w_{\mathrm{f},1}(n) &= (w_{\mathrm{f},1,\mathrm{init}}(n) + w_{\mathrm{f},1,\mathrm{end}}(n))\,/2\\ w_{\mathrm{f},1,\mathrm{init}}(n) &= \left|\beta(n - F_{\mathrm{span}} + 1)/ts - \hat{\beta}_{\mathrm{c}}(n - F_{\mathrm{span}} + 1)\right|\\ w_{\mathrm{f},1,\mathrm{end}}(n) &= \left|\beta(n)/ts - \hat{\beta}_{\mathrm{c}}(n)\right|. \end{aligned}$$

Notice that again, the weights are proportional to the time distance between the original initial and last sampling points.

In the second part of the algorithm, we calculate an SRRC pulse with another

length. The new length of the SRRC is calculated as

$$\begin{aligned} \mathrm{l}_{\mathrm{ceil,init}} &= \left\lceil \hat{\beta}_{\mathrm{c}}(n - F_{\mathrm{span}} + 1) \right\rceil, && (5.37) \\ \mathrm{l}_{\mathrm{floor,end}} &= \lfloor F_{\mathrm{span}}\, T_{new}/t_s \rfloor = \lfloor F_{\mathrm{span}}\, \left(\beta(n) - \beta(n-1)\right)/t_s \rfloor, && (5.38) \end{aligned}$$

resulting in a pulse $\boldsymbol{p}_{\mathrm{l}}$, where each element is expressed as $p_l(m)$ with $m \in \{0, t_s, 2t_s, \cdots, (\mathrm{l}_{\mathrm{floor,end}} - \mathrm{l}_{\mathrm{ceil,init}} + 1)t_s\}$. In this second part, we use a pulse $\boldsymbol{p}_{\mathrm{l}}$ whose length is as large as possible in order to be able to gather only the samples of the received signal $\boldsymbol{r}$ that have no information regarding the adjacent symbols, i.e., it does not take into account the edge samples (both the first and last).

So, the algorithm of the second part can be portrayed as

$$\begin{aligned} \boldsymbol{r}_{\mathrm{MF,l}} &= \boldsymbol{r} * \boldsymbol{p}_{\mathrm{l}} && (5.39) \\ \boldsymbol{r}_{\mathrm{MF,c}} &= \boldsymbol{r} * \boldsymbol{p}_{\mathrm{c}} && (5.40) \\ \widehat{\underline{s}}_{\mathrm{alg}_{3,2}}(n) &= w_{\mathrm{c},2}(n)\ \cdot r_{\mathrm{MF,c}}(\hat{\beta}_{\mathrm{c}}(n)) + w_{\mathrm{f},2}(n)\ \cdot r_{\mathrm{MF,l}}(\hat{\beta}_{\mathrm{f}}(n)), && (5.41) \end{aligned}$$

where $w_{\mathrm{c},2}(n)$, $w_{\mathrm{f},2}(n)$ are weights. The idea of this second part is to perform a weighted average of two distinct signals. The first signal is the result of the convolution of the received signal with the pulse $\boldsymbol{p}_{\mathrm{l}}$, and does not consider the edge samples. The second signal, which is the result of the convolution of the received signal with the pulse $\boldsymbol{p}_{\mathrm{c}}$, considers both edge samples.

The weight $w_{\mathrm{c},2}(n)$ is calculated as

$$\begin{aligned} w_{\mathrm{c},2}(n) &= \left(w_{\mathrm{c,2,init}}(n) + w_{\mathrm{c,2,end}}(n)\right)/2 \\ w_{\mathrm{c,2,init}}(n) &= \left|\beta(n - F_{\mathrm{span}} + 1)/ts - \hat{\beta}_{\mathrm{c}}(n - F_{\mathrm{span}} + 1)\right| \\ w_{\mathrm{c,2,end}}(n) &= \left|\beta(n)/ts - \hat{\beta}_{\mathrm{f}}(n)\right|, \end{aligned}$$

and $w_{\mathrm{f},2}(n)$ as

$$\begin{aligned} w_{\mathrm{f},2}(n) &= \left(w_{\mathrm{f,2,init}}(n) + w_{\mathrm{f,2,end}}(n)\right)/2 \\ w_{\mathrm{f,2,init}}(n) &= \left|\beta(n - F_{\mathrm{span}} + 1)/ts - \hat{\beta}_{\mathrm{f}}(n - F_{\mathrm{span}} + 1)\right| \\ w_{\mathrm{f,2,end}}(n) &= \left|\beta(n)/ts - \hat{\beta}_{\mathrm{c}}(n)\right|. \end{aligned}$$

As a result, the symbol is estimated using a combination of the two previous algorithms

$$\widehat{\underline{s}}_{\mathrm{alg}_3}(n) = \left(\widehat{\underline{s}}_{\mathrm{alg}_{3,1}}(n) + \widehat{\underline{s}}_{\mathrm{alg}_{3,2}}(n)\right)/2. \quad (5.42)$$

Illustrative Example:

In this example our aim is to show the procedure performed by Algorithm 3. Once more, we consider the same previous parameters: a filter span of 3 symbols ($F_{\text{span}} = 3$), and $sps = 20$, with a Doppler effect that induces a new pulse duration of $T_{SRRC,\text{new}} = 20.3 \cdot 3 + 1 = 61.6$.

The idea and the procedure performed in Algorithm 3 are shown in Figure 5.5. This figure illustrates the computation of the signals $r_{\text{MF,f}}(\hat{\beta}_{\text{c}}(n))$, $r_{\text{MF,f}}(\hat{\beta}_{\text{f}}(n))$, $r_{\text{MF,c}}(\hat{\beta}_{\text{c}}(n))$, and $r_{\text{MF,l}}(\hat{\beta}_{\text{f}}(n))$. A combination of these signals (Eq. (5.42)) provides the symbol estimation.

It is important to perceive that we are trying to perform distinct signal combinations, in order to gather the maximum amount of information regarding the n-th symbol.

Algorithm 4

In the fourth algorithm, the pulse SRRC is computed as

$$\text{m}_{\text{ceil}} = \lceil F_{\text{span}}\, T_{new}/t_s \rceil = \lceil F_{\text{span}}\ (\beta(n) - \beta(n-1))\,/t_s \rceil\,, \tag{5.43}$$

leading to the vector $\boldsymbol{p}_{\text{c}}$, whose elements are defined as $p_{\text{c}}(m)$, with $m \in \{0, t_s, 2t_s, \cdots, \text{m}_{\text{ceil}} t_s\}$.

In this algorithm, we replace some samples of the received signal $\boldsymbol{r}$ (samples of time instant $\hat{\beta}_{\text{c}}(n - F_{\text{span}} + 1)$ and $\hat{\beta}_{\text{c}}(n)$), with an estimation of the signal that could have been received at time instant $\beta(n - F_{\text{span}} + 1)$ and $\beta(n)$ respectively. That is, the following procedure is performed:

$$\begin{aligned} \hat{r}(\hat{\beta}_{\text{f}}(n - F_{\text{span}} + 1)) &= w_{\text{f,init}}(n) r(\hat{\beta}_{\text{f}}(n - F_{\text{span}} + 1)) + w_{\text{c,init}}(n) r(\hat{\beta}_{\text{c}}(n - F_{\text{span}} + 1)) \\ \hat{r}(\hat{\beta}_{\text{c}}(n) + 1) &= w_{\text{f,end}}(n) r(\hat{\beta}_{\text{f}}(n) + 1) + w_{\text{c,end}}(n) r(\hat{\beta}_{\text{c}}(n) + 1) \end{aligned} \tag{5.44}$$

where $w_{\text{f,init}}(n)$, $w_{\text{c,init}}(n)$, $w_{\text{f,end}}(n)$, and $w_{\text{c,end}}(n)$ are given by:

$$\begin{aligned} w_{\text{c,init}}(n) &= \left| \beta(n - F_{\text{span}} + 1)/ts - \hat{\beta}_{\text{f}}(n - F_{\text{span}} + 1) \right| \\ w_{\text{f,init}}(n) &= \left| \beta(n - F_{\text{span}} + 1)/ts - \hat{\beta}_{\text{c}}(n - F_{\text{span}} + 1) \right| \\ w_{\text{c,end}}(n) &= \left| \beta(n)/ts - \hat{\beta}_{\text{f}}(n) \right| \\ w_{\text{f,end}}(n) &= \left| \beta(n)/ts - \hat{\beta}_{\text{c}}(n) \right|. \end{aligned}$$

Therefore, algorithm 4 can be implemented as

$$\boldsymbol{r}_{\text{MF,c}} = \hat{\boldsymbol{r}} * \boldsymbol{p}_{\text{c}} \tag{5.45}$$

$$\widehat{\underline{s}}_{\text{alg}_4}(n) = r_{\text{MF,c}}(\hat{\beta}_{\text{c}}(n)). \tag{5.46}$$

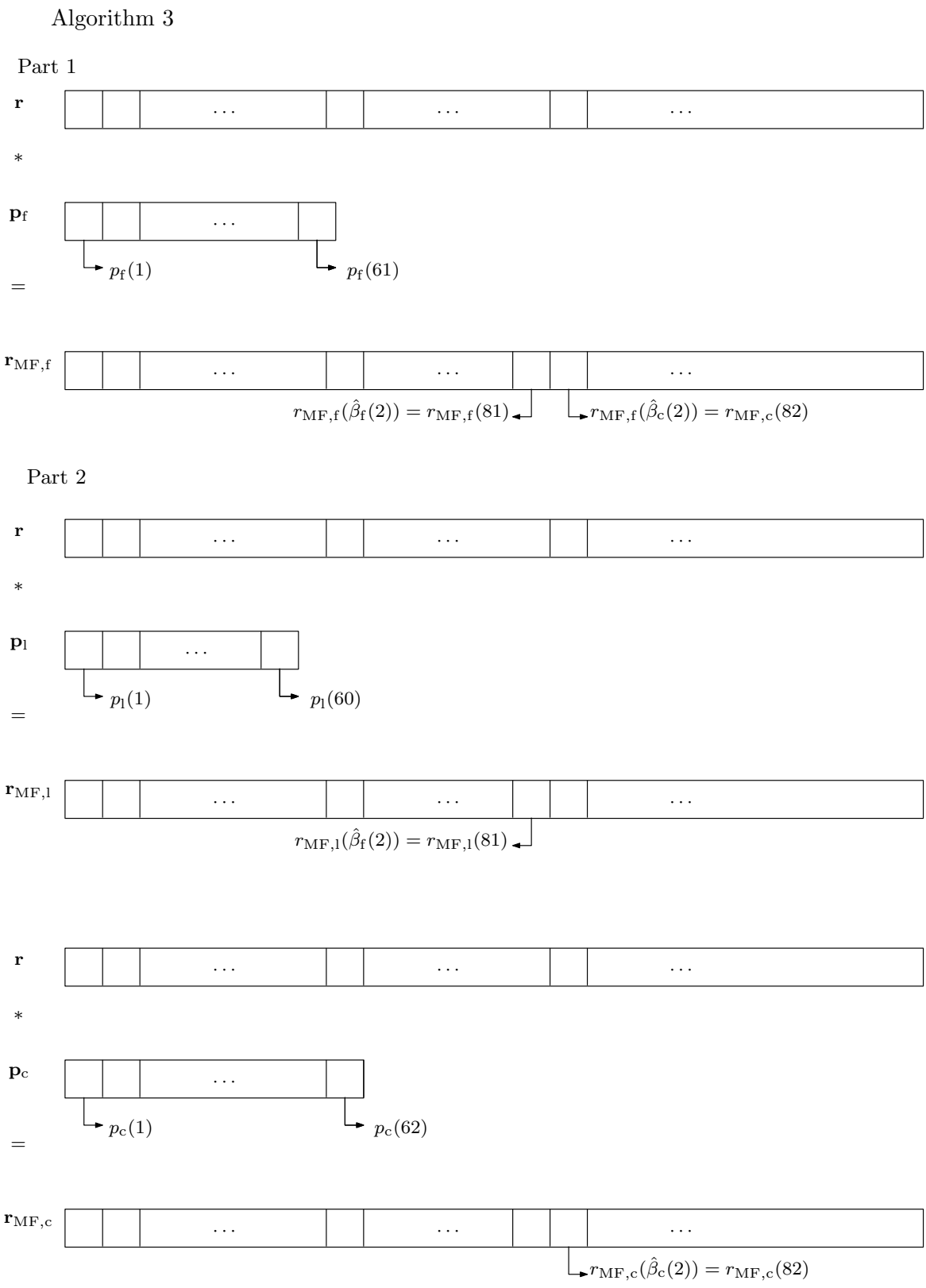

Figure 5.5: Procedure for performing the estimation of the second symbol with Algorithm 3.

Illustrative Example:

Once more, we consider the same parameters for showing the idea of Algorithm 4: a filter span of 3 symbols ($F_{\text{span}} = 3$), and $sps = 20$, with a Doppler effect that induces a new pulse duration of $T_{SRRC,\text{new}} = 20.3 \cdot 3 + 1 = 61.6$.

Figure 5.6 elucidates the computation of the replacement of some samples of the signal $\boldsymbol{r}$. These new sample values are designated as $\hat{r}(\hat{\beta}_{\text{f}}(n - F_{\text{span}} + 1))$ and $\hat{r}(\hat{\beta}_{\text{c}}(n) + 1)$. This figure also shows the calculus of $\boldsymbol{r}_{\text{MF,c}}$. The symbol is estimated with Eq. (5.45).

Algorithm 4

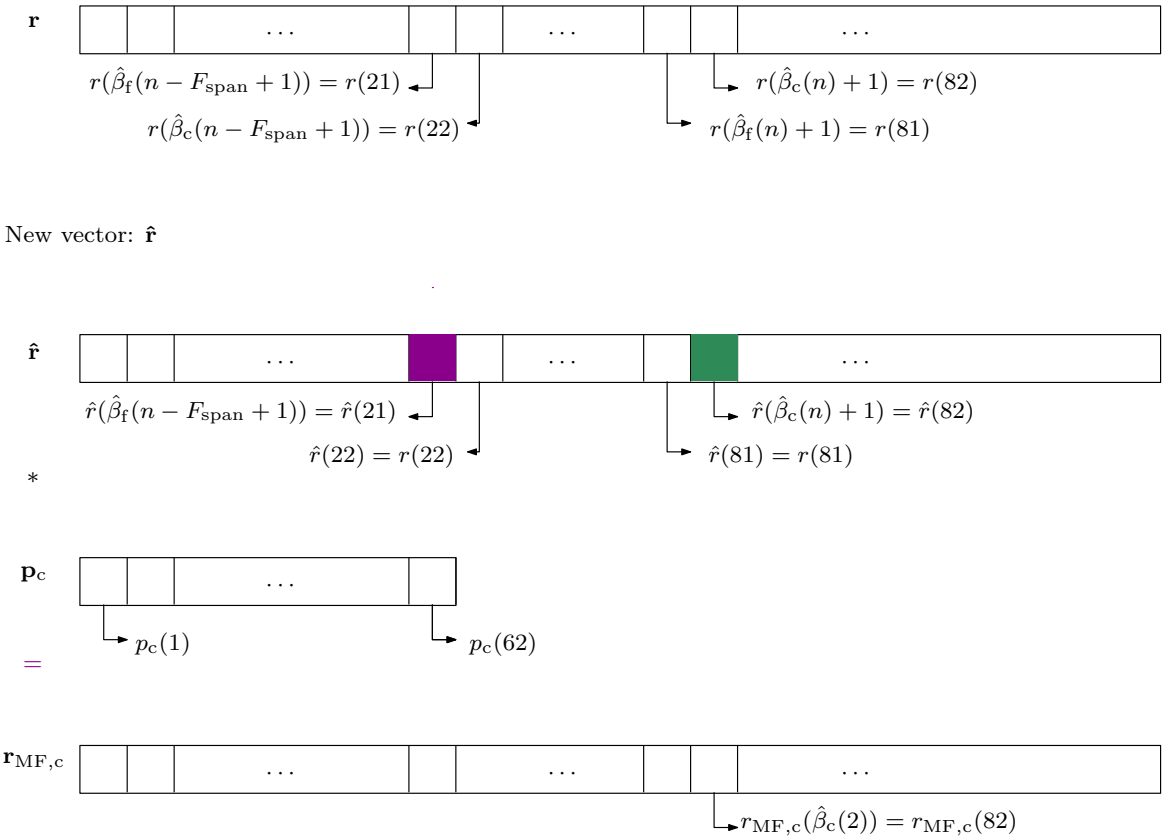

Figure 5.6: Procedure for performing the estimation of the second symbol with Algorithm 4.

Notice that the idea in replacing some signal samples of the received signal $\boldsymbol{r}$, is to minimize the amount of information from the adjacent symbols.

5.1.3 Simulation Results

The simulation purpose is to measure the mean square error (MSE) of the estimated symbols considering the aforementioned receiver types. The MSE is computed ac-

Table 5.1: MSE per symbol

Velocity	Rec. 1	Rec. 2	Rec. 2 (branch)	Rec. 3	Rec. 4 (alg. 1)
$v = 20$ m/s	1.86	4.68×10^{-4}	20	9.37×10^{-4}	1.92×10^{-4}
$v = 15$ m/s	1.90	3.47×10^{-4}	15	7.10×10^{-4}	0.76×10^{-4}
$v = 12$ m/s	1.86	1.83	15	5.91×10^{-4}	1.00×10^{-4}
$v = 10$ m/s	1.86	1.81	8	5.39×10^{-4}	1.55×10^{-4}
$v = 8$ m/s	1.84	5.20×10^{-4}	8	4.59×10^{-4}	2.43×10^{-4}
$v = 5$ m/s	1.82	4.53×10^{-4}	5	3.98×10^{-4}	1.83×10^{-4}
$v = 1$ m/s	1.72	3.54×10^{-4}	1	3.50×10^{-4}	0.82×10^{-4}
$v = 0.5$ m/s	1.57	1.57	1	3.58×10^{-4}	0.78×10^{-4}
$v = 0$ m/s	0.76×10^{-4}	0.76×10^{-4}	0	0.76×10^{-4}	0.76×10^{-4}
$v = -15$ m/s	1.88	3.59×10^{-4}	-15	6.54×10^{-4}	0.76×10^{-4}

cording to the equation:

$$\text{MSE} = \frac{1}{M} \sum_{n=0}^{M-1} \left| \underline{\widehat{s}}(n) - \underline{s}(n) \right|^2 . \tag{5.47}$$

In order to evaluate the MSE of each receiver type, the following parameters were considered. We generated 10 blocks of symbols, where each block contains 1000 symbols random generated ($\underline{s} \in \{-1, +1\}$), and each symbol was mapped to a SRRC waveform. The SRRC is characterized by a roll-off factor of $\alpha = 0.5$, a filter span of 5 symbols ($F_{\text{span}} = 5$), and $sps = 20$, meaning that one pulse SRRC lasts for 101 samples. For the bank of cross-correlators receiver, 11 branches were considered, whereas each branch corresponds to one of these relative velocity (in m/s): $v \in \{-20, -15, -8, -5, -1, 0, 1, 5, 8, 15, 20\}$. As the pulse SRRC might not assume an integer value, we rounded towards the nearest integer. Likewise, the equally spaced sampling points of each branch might not assume integer values, so we rounded again towards the nearest integer. The first block of symbols is used to select the branch with the highest correlation. The sound speed was $c = 1500$ m/s.

Tables 5.1 and 5.2 show the MSE values for each receiver type, for a fixed relative velocity. It is important to highlight that the estimated symbols $\underline{\widehat{s}}(n)$ are not quantized, and in the case with $v = 0$ m/s, the estimated symbols were supposed to have unitary energy, what would result in a zero MSE. In fact, this behavior is not observed in Tables 5.1, 5.2 due to finite time support of the pulses SRRC, and to numerical imprecision in Matlab.

From Table 5.1, it is possible to observe that the standard receiver (Rec. 1) had a high MSE value for any relative velocity, meaning this receiver block was not able to efficiently deal with Doppler effect, requiring other additional processing techniques. The bank of cross-correlator receiver (Rec. 2) was able to obtain lower MSE values for cases in which one branch matches perfectly with the induced Doppler effects.

However, if there is no "perfect match", the MSE values are similar to the first receiver.

The third receiver managed better Doppler effects than the first receiver type. Although, as the relative velocity between transmitter and receiver increased, the MSE value per symbol also raised, probably because the ISI was increased.

The fourth receiver, which is our proposal, got better MSE values than the other receivers. Table 5.2 shows the MSE values regarding all the algorithm types proposed for the fourth receiver. In most cases, the first algorithm reached the best performance values among all proposed algorithms.

Table 5.2: MSE ($\times 10^{-4}$) per symbol for algorithms of receiver 4

Velocity	Alg. 1	Alg. 2	Alg. 3,1	Alg. 3,2	Alg. 3	Alg. 4
$v = 20$ m/s	1.92	1.63	3.93	3.73	4.61	4.36
$v = 15$ m/s	0.76	3.38	1.47	0.83	3.43	3.44
$v = 12$ m/s	1.00	2.39	8.74	8.42	9.82	8.66
$v = 10$ m/s	1.55	1.84	6.76	6.46	7.55	7.16
$v = 8$ m/s	2.43	1.51	5.60	5.45	6.14	5.84
$v = 5$ m/s	1.83	1.66	3.86	3.65	4.58	4.35
$v = 1$ m/s	0.82	2.90	1.85	1.30	3.55	3.50
$v = 0.5$ m/s	0.78	3.17	1.61	1.00	3.47	3.45
$v = 0$ m/s	0.76	0.76	1.39	0.76	3.05	0.76
$v = -15$ m/s	0.76	3.44	1.51	0.85	3.52	3.55

Considering the performance of Receiver 4, we observe that some MSE values are lower for some higher velocities. In order to investigate further the relationship between the MSE and the velocity, we calculated the MSE standard deviation, which is denoted by σ. The obtained results are shown in Tables 5.3 and 5.4.

As can be observed from Tables 5.3, 5.4, all algorithms of Receiver 4 have high standard deviation for all relative velocities. This behavior might be explained by Matlab numerical imprecision, by the finite time support of the pulse SRRC, and by rounding operations performed by each algorithm. Notice that the same rounding operation will probably lead to distinct MSE results when different relative velocities are considered. Despite that, some rounding operations might be more beneficial for certain numbers of relative velocity, while for other numbers of relative velocity, the same operation will not provide the same benefit. As discussed in Subsection 5.1.2, this receiver type is very sensitive to round operations and to numerical imprecision. With these results, we are not able to induce any straight relationship between the relative velocity and the MSE values of Receiver 4.

In order to investigate further how the above the effects might influence the MSE value, we ran another simulation. In this simulation, we modified only one parameter: $sps = 100$, meaning that one pulse SRRC will last for 501 samples. We

Table 5.3: MSE ($\times 10^{-4}$) and standard deviation represented by σ ($\times 10^{-4}$).

Velocity	Rec. 3		Rec. 4 (alg. 1)	
	MSE	σ	MSE	σ
$v = 20$ m/s	9.37	14.78	1.92	2.39
$v = 15$ m/s	7.10	11.82	0.76	0.89
$v = 12$ m/s	5.91	9.91	1.00	1.23
$v = 10$ m/s	5.39	8.98	1.55	1.87
$v = 8$ m/s	4.59	7.76	2.43	2.75
$v = 5$ m/s	3.98	6.43	1.83	2.29
$v = 1$ m/s	3.50	5.43	0.82	0.97
$v = 0.5$ m/s	3.58	5.52	0.78	0.92
$v = 0$ m/s	0.76	0.89	0.76	0.89
$v = -15$ m/s	6.54	11.39	0.76	0.89

Table 5.4: MSE ($\times 10^{-4}$) per symbol for algorithms of receiver 4

Velocity	Rec. 4 (alg. 2)		Rec. 4 (alg. 3,1)		Rec. 4 (alg. 3,2)		Rec. 4 (alg. 3)		Rec. 4 (alg. 4)	
	MSE	σ	MSE	σ	MSE	σ	MSE	σ	MSE	σ
$v = 20$ m/s	1.63	2.32	3.93	7.44	3.73	7.13	4.61	8.17	4.36	7.63
$v = 15$ m/s	3.38	5.01	1.47	2.27	0.83	1.44	3.43	5.37	3.44	4.97
$v = 12$ m/s	2.39	3.85	8.74	44.67	8.42	44.61	9.82	45.52	8.66	15.12
$v = 10$ m/s	1.84	2.88	6.76	10.50	6.46	9.26	7.55	13.29	7.16	12.92
$v = 8$ m/s	1.51	2.13	5.60	9.25	5.45	8.60	6.14	10.87	5.84	10.48
$v = 5$ m/s	1.66	2.38	3.86	7.36	3.65	7.05	4.58	8.09	4.35	7.53
$v = 1$ m/s	2.90	4.37	1.85	3.60	1.30	3.24	3.55	5.51	3.50	5.04
$v = 0.5$ m/s	3.17	4.74	1.61	2.83	1.00	2.27	3.47	5.44	3.45	5.01
$v = 0$ m/s	0.76	0.89	1.39	1.75	0.76	0.89	3.05	3.68	0.76	0.89
$v = -15$ m/s	3.44	5.11	1.51	2.42	0.85	1.66	3.53	5.56	3.55	5.16

kept the other parameter values.

Table 5.5 shows the MSE and the MSE standard deviation for Receiver 3 and Receiver 4 (alg. 1). The first aspect to be analyzed is that when there is no Doppler effect ($v = 0$ m/s), the MSE value is higher than the one obtained in the previous simulation scenario (see Table 5.1). A possible explanation for this behavior is that the finite time support of the pulse SRRC combined with Matlab numerical imprecision were a bit higher in this scenario.

When comparing this scenario with the previous simulation, it was expected that the augment in the number of samples representing one symbol could reduce the MSE and the MSE standard deviation. As expected, this phenomena was observed in Receiver 3, and for almost all relative movements of Receiver 4 (alg. 1). For the other relative movements, the MSE of Receiver 4 was higher (than Table 5.3) due to the minimal expected MSE error (as observed with $v = 0$ m/s), which could be combined with an unfavorable rounding operation.

Table 5.5: MSE ($\times 10^{-4}$) and standard deviation σ ($\times 10^{-4}$) for $sps = 100$

Velocity	Rec. 3		Rec. 4 (alg. 1)	
	MSE	σ	MSE	σ
$v = 20$ m/s	7.21	8.08	0.80	0.91
$v = 15$ m/s	4.63	5.47	0.81	0.92
$v = 12$ m/s	3.38	4.17	0.81	0.91
$v = 10$ m/s	2.71	3.37	0.88	1.02
$v = 8$ m/s	2.11	2.68	0.80	0.93
$v = 5$ m/s	1.45	1.87	0.81	0.93
$v = 1$ m/s	0.97	1.17	0.87	1.01
$v = 0.5$ m/s	0.94	1.13	0.83	0.94
$v = 0$ m/s	0.80	0.91	0.80	0.91
$v = -15$ m/s	3.86	4.23	0.81	0.92

5.2 Passband System: Doppler Compensation for a Single Path Channel

In this second system model, our objective is to evaluate and analyze the influence of Doppler effect in a passband signal. In other words, we would like to comprehend how this effect may distort a signal modulated by a carrier wave. The considered system is illustrated in Figure 5.7. As observed from Figure 5.7, this system model comprises more processing blocks than the model presented in the previous section. A mathematical description of each processing block will be presented hereafter.

The signal $\underline{\boldsymbol{s}}$ is a vector with M symbols. Each symbol is mapped into a pulse shaping format as

$$x(t) = \sum_{n=0}^{M-1} \underline{s}(n) p(t - nT), \tag{5.48}$$

where $p(t)$ is the pulse waveform, and T is the symbol period. This signal is modulated by the carrier leading to the passband signal

$$x_{\mathrm{PB}}(t) = 2\Re\left\{x(t)\mathrm{e}^{\mathrm{j}2\pi f_{\mathrm{c}} t}\right\} \tag{5.49}$$

where f_{c} is the carrier central frequency. Notice that only the real part of the signal was selected.

This signal is transmitted through a channel with a single and unitary path, but with Doppler effect

$$h(t, \tau) = 1 \cdot \delta(\tau - \tau(t)). \tag{5.50}$$

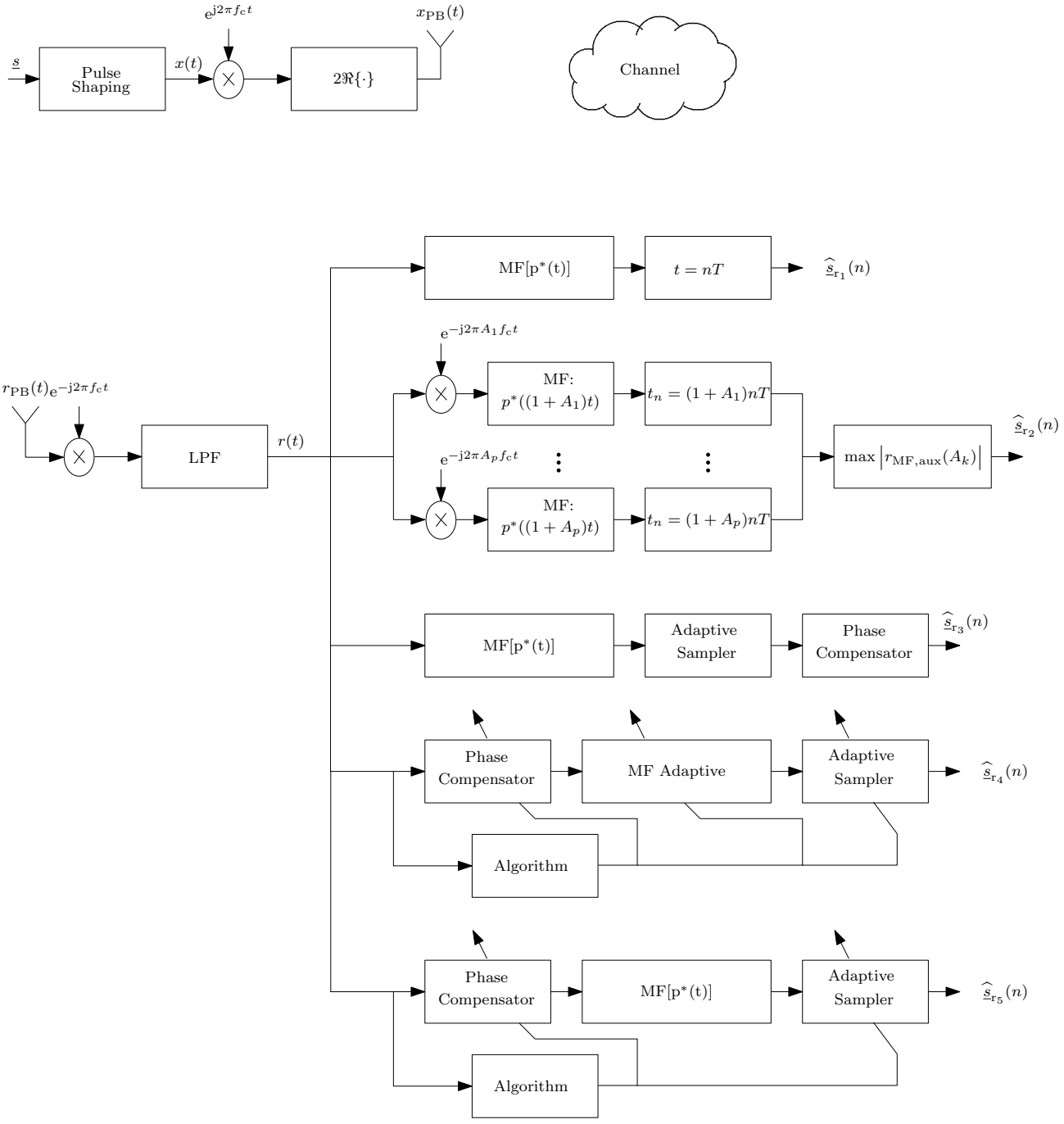

Figure 5.7: Passband system model.

The received signal is represented as

$$\begin{aligned} r_{\mathrm{PB}}(t) &= x_{\mathrm{PB}}(t-\tau(t)), \\ &= \left\{x(t-\tau(t))\mathrm{e}^{\mathrm{j}2\pi f_{\mathrm{c}}(t-\tau(t))} + x^*(t-\tau(t))\mathrm{e}^{-\mathrm{j}2\pi f_{\mathrm{c}}(t-\tau(t))}\right\}. \end{aligned} \quad (5.51)$$

At the receiver side, the first procedure is the removal of the carrier frequency through the multiplication by the exponential factor $\mathrm{e}^{-\mathrm{j}2\pi f_{\mathrm{c}}t}$

$$\begin{aligned} r_{\mathrm{BB}}(t) &= r_{\mathrm{PB}}(t)\mathrm{e}^{-\mathrm{j}2\pi f_{\mathrm{c}}t} \\ &= \left\{x(t-\tau(t))\mathrm{e}^{-\mathrm{j}2\pi f_{\mathrm{c}}\tau(t)} + x^*(t-\tau(t))\mathrm{e}^{-\mathrm{j}2\pi f_{\mathrm{c}}(2t-\tau(t))}\right\} \end{aligned} \quad (5.52)$$

The next block is a lowpass filter. The objective of this filter is to remove the signal components located at high frequency. The resulting signal can be represented as

$$\begin{aligned} r(t) &= \mathrm{LPF}\left\{r_{\mathrm{BB}}(t)\right\} \\ &= x(t-\tau(t))\mathrm{e}^{-\mathrm{j}2\pi f_{\mathrm{c}}\tau(t)} \\ &= \mathrm{e}^{-\mathrm{j}2\pi f_{\mathrm{c}}\tau(t)} \sum_{n=0}^{M-1} \underline{s}(n)p(t-\tau(t)-nT). \end{aligned} \quad (5.53)$$

It is important to note that the received signal suffered a time warping effect,[4] which can be seen in the variable $p(t-\tau(t)-nT)$, and a time-variable phase shift, expressed by $\mathrm{e}^{-\mathrm{j}2\pi f_{\mathrm{c}}\tau(t)}$. Notice that in the previous model (Section 5.1), the equivalent signal (Eq. (5.3)) just experienced a time warping effect. Therefore, in order to be able to recover this signal, some additional processing techniques might be necessary.

5.2.1 Receiver types

The considered receiver types are the same as presented in the previous section. The main difference lies in the additional treatment of the time-variable phase shift, that was not required in the previous section.

Receiver 1

This first receiver is a standard one. The objective of taking into account this receiver type is to quantify and to observe the performance gain in treating Doppler effect at an earlier stage at the receiver side.

The equations describing this receiver are the same as presented in the equivalent

[4]The time warping effect distorts the pulse duration.

previous subsection, and the signal at the matched filter output is given by

$$r_{\mathrm{MF,r_1}}(t) \;=\; \int p(T-t)\mathrm{e}^{-\mathrm{j}2\pi f_c\tau(t)}\sum_{n=0}^{M-1}\underline{s}(n)p(t-\tau(t)-nT)\mathrm{d}t \tag{5.54}$$

and the symbol estimation is performed after the sampling operation at $t = nT$ for $n \in \{0, 1, \cdots, M-1\}$, i.e.,

$$\widehat{\underline{s}}_{\mathrm{r_1}}(n) \;=\; r_{\mathrm{MF,r_1}}(n) \tag{5.55}$$

Once more, it is possible to infer that the symbol estimation of Eq. (5.55) was affected by ISI. The intersymbol interference might be perceived in Eq. (5.54). As the received pulse waveform suffered time-warping effect, i.e., the received pulse had its length expanded or shrinked, and the filter at the received side has the transmitted pulse length, this filtering process might induce severe ISI.

Receiver 2

The signal processing of the cross-correlator filter bank is similar to the one presented in the previous section. The main difference lies in an extra exponential factor in each filter.

Each filter of the bank performs the following procedure [79]

$$r_{\mathrm{MF,aux}}(A_k) = \int_0^{\frac{T}{(1+A_k)}} r(t)p^*((1+A_k)t)\mathrm{e}^{-\mathrm{j}2\pi A_k f_c t}\mathrm{d}t, \tag{5.56}$$

and the Doppler factor is selected using the same criteria as before

$$\hat{a} = \max_{1\leq k\leq p}\left|r_{\mathrm{MF,aux}}(A_k)\right|. \tag{5.57}$$

With the knowledge of the selected filter, the received signal is processed

$$r_{\mathrm{MF,r_2}}(t) = r(t)\mathrm{e}^{-\mathrm{j}2\pi\hat{a}f_c t} * p_2(t), \tag{5.58}$$

where $p_2(t) = p^*(-(1+\hat{a})t)$, and the signal is sampled at rate $t = (1/(1+\hat{a}))nT$, resulting in

$$\widehat{\underline{s}}_{\mathrm{r_2}}(n) \;=\; r_{\mathrm{MF,r_2}}((1/(1+\hat{a}))nT). \tag{5.59}$$

Receiver 3

The third receiver is quite similar to the one presented in Subsection 5.1.1. Once more, the main distinction is related to the compensation of the phase shift. In this

case, the phase shift induced by the Doppler effect is compensated at the symbol level. It is important to highlight that the employed block sequence processing is the one proposed by [43, 44], or in other words, first it is calculated the time instant such that the signal should be sampled, and then the phase of this unique sample is compensated.

In this receiver, the signal passes through a filter that is matched with the transmitted pulse resulting in:

$$r_{\mathrm{MF,r_3}}(t) = \int p(T-t)\left\{\sum_{n=0}^{M-1}\underline{s}(n)p(t-\tau(t)-nT)\mathrm{e}^{-\mathrm{j}2\pi f_c\tau(t)}\right\}\mathrm{d}t \quad (5.60)$$

The next stage is the selection of the sampling point of the signal $r_{\mathrm{MF,r_3}}(t)$. The sampling point is computed as before, and with the same assumptions: the parameter ϵ_{n-1} is not updated and is set to zero, because we do not have access to the original transmitted signal, leading to the following algorithm

$$\dot{\beta}(n) = \dot{\beta}(n-1) \quad (5.61)$$
$$\beta(n) = \beta(n-1)+\dot{\beta}(n)T. \quad (5.62)$$

So, the resulting signal is given by

$$\widehat{\underline{r}}_{\mathrm{r_3}}(n) = r_{\mathrm{MF,r_3}}(\beta(n)). \quad (5.63)$$

The signal phase induced by the Doppler effect is compensated through the multiplication by the exponential value $\mathrm{e}^{\mathrm{j}2\pi f_c(\beta(n)-nT)}$:

$$\widehat{\underline{s}}_{\mathrm{r_3}}(n) = \widehat{\underline{r}}_{\mathrm{r_3}}(n)\mathrm{e}^{\mathrm{j}2\pi f_c(\beta(n)-nT)}, \quad (5.64)$$

giving rise to the symbol estimation.

Receiver 4

As the received signal $r(t)$

$$r(t) = \sum_{n=0}^{M-1}\underline{s}(n)p(t-\tau(t)-nT)\mathrm{e}^{-\mathrm{j}2\pi f_c\tau(t)}, \quad (5.65)$$

possess a distinct model from the received signal presented in the previous section (Eq. (5.3)), one should take into account that the block processing sequence might improve or deteriorate the signal estimation.

As can be noticed, the phase component of Eq. (5.65) is time-dependent. So, if we could remove firstly its phase distortion, the resulting signal would be similar

to the one described in Eq. (5.3). On the other hand, if we first filter the signal of Eq. (5.65), the resulting signal would be a combination of distinct time-dependent exponential factors, yielding the process of signal recovering more challenging.

Considering the aforementioned analysis, we will estimate and compensate firstly the exponential factor of Eq. (5.65). The process of phase estimation and compensation might use the same algorithm of the adaptive filter (Eqs. (5.16)), with some modifications.

We can rewrite Eq. (5.65)

$$\begin{aligned} r(t) &= x(t-\tau(t))\mathrm{e}^{-\mathrm{j}2\pi f_c \tau(t)} \\ &= x(\alpha(t))\mathrm{e}^{-\mathrm{j}2\pi f_c (t-\alpha(t))}. \end{aligned} \tag{5.66}$$

As we have access to the signal sampled at a rate $t = mt_s$, the previous equation can be rewritten as

$$r(mt_s) = x(\alpha(mt_s))\mathrm{e}^{-\mathrm{j}2\pi f_c (mt_s - \alpha(mt_s))}. \tag{5.67}$$

We could multiply each signal sample $r(mt_s)$ by $\mathrm{e}^{\mathrm{j}2\pi f_c (mt_s - \alpha(mt_s))}$. However, we do need to estimate the function $\alpha(mt_s)$ for all time instants.

Considering that the number of samples per symbol (sps) is high enough, such that

$$\forall n,\ \exists\, m,\ \text{s.t. } \mathrm{mt_s} - \beta(\mathrm{nT}) < \epsilon \tag{5.68}$$

whereas $\beta(nT)$ is the sampling point of symbol n and that $\epsilon \approx 0$,

$$\beta(nT) \approx mt_s, \tag{5.69}$$

and

$$\alpha(mt_s) = nT, \tag{5.70}$$

because $\alpha(\beta(nT)) = nT$. Even so, it is important to notice that only for a few samples, the function $\alpha(\cdot)$ is available, that is, just for the m-values under the condition

$$\alpha(m_p t_s) = nT \tag{5.71}$$

$$\alpha(m_q t_s) = (n+1)T. \tag{5.72}$$

As we have the knowledge of m_p, m_q,[5] we can compute the number of points of $\hat{\alpha}(\cdot)$ to be estimated

$$\#\hat{\alpha}(\cdot) \quad = \quad m_q - m_p + 1. \tag{5.73}$$

Assuming that the difference between two $\hat{\alpha}(\cdot)$ is constant:

$$\hat{\alpha}(m_{p+1}t_s) - \alpha(m_p t_s) = \hat{\alpha}(m_{p+2}t_s) - \hat{\alpha}(m_{p+1}t_s) = \cdots = \alpha(m_q t_s) - \hat{\alpha}(m_{q-1}t_s), \tag{5.74}$$

we can calculate the interval between these two functions value as:

$$\Delta\hat{\alpha} = \frac{\alpha(m_q t_s) - \alpha(m_p t_s)}{\#\hat{\alpha}(\cdot)}. \tag{5.75}$$

With this interval, it is possible to compute the other values of $\hat{\alpha}(\cdot)$ as

$$\hat{\alpha}(m_{p+1}t_s) = \alpha(m_p t_s) + \Delta\hat{\alpha}. \tag{5.76}$$

So, the following procedure is performed in Receiver 4. Firstly, we run the algorithm of Eqs. (5.16) for calculating the value of $\beta(n+1)$. In the next step, we compensate the signal phase of the samples inside the interval $\{\beta(n), \beta(n+1)\}$ multiplying it by $\mathrm{e}^{\mathrm{j}2\pi f_c(mt_s - \hat{\alpha}(mt_s))}$

$$r_{\mathrm{p}}(m) \quad = \quad r(mt_s)\mathrm{e}^{\mathrm{j}2\pi f_c(mt_s - \hat{\alpha}(mt_s))} \tag{5.77}$$

$$\quad = \quad x(\alpha(mt_s))\mathrm{e}^{-\mathrm{j}2\pi f_c(mt_s - \alpha(mt_s))}\mathrm{e}^{\mathrm{j}2\pi f_c(mt_s - \hat{\alpha}(mt_s))}. \tag{5.78}$$

Using the parameters obtained in the algorithm iteration below

$$\dot{\beta}(n+1) \quad = \quad \dot{\beta}(n) \tag{5.79}$$

$$\beta(n+1) \quad = \quad \beta(n) + \dot{\beta}(n+1)T, \tag{5.80}$$

the filter is adapted according to one of the algorithms previously described in Subsection 5.1.2.

The signal of Eq. (5.77), passes through this filter and is sampled at the instant $m = \beta(n+1)$

$$\widehat{\underline{s}}_{\mathrm{r}_4}(n+1) = r_{\mathrm{MF,r_4}}(\beta(n+1)) = \underline{s}(n+1) + \xi_{n+1}, \tag{5.81}$$

where ξ_{n+1} accounts for the adaptive filter inaccuracies.

[5]Notice that the values of m_p, m_q are calculated with Eq. (5.69).

Receiver 5

The fifth receiver is a simplified version of Receiver 4. The main difference is that the pulse shape is not adapted at the receiver side, thus requiring a reduced amount of mathematical operations as compared to Receiver 4. This idea is illustrated in Fig. 5.8, and this procedure is described hereafter.

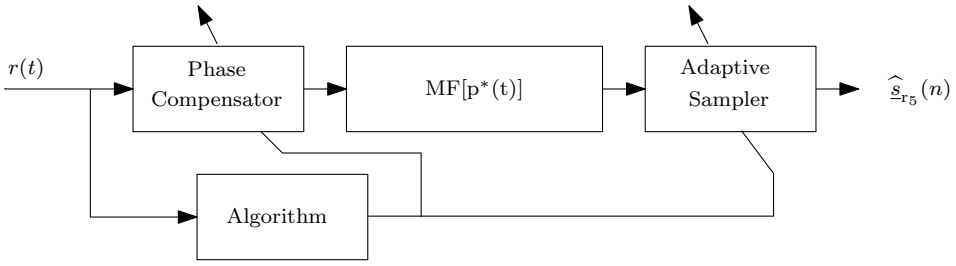

Figure 5.8: Receiver 5.

At the receiver, we only have access to a discrete version of the received signal $r(t)$, because this signal was acquired with a sample rate of $t = mt_s$. The signal $r(mt_s)$ is given by

$$r(mt_s) = x(\alpha(mt_s))\mathrm{e}^{-\mathrm{j}2\pi f_c(mt_s-\alpha(mt_s))}. \tag{5.82}$$

First we run the previously mentioned algorithm, which is rewritten here for convenience

$$\dot{\beta}(n+1) = \dot{\beta}(n) \tag{5.83}$$

$$\beta(n+1) = \beta(n) + \dot{\beta}(n+1)T. \tag{5.84}$$

In the next step, we compute the values of $\hat{\alpha}(\cdot)$ inside the interval $[\beta(n), \beta(n+1)]$, using the same method described in Receiver 4:

$$\hat{\alpha}(m_{p+1}t_s) = \alpha(m_p t_s) + \Delta\hat{\alpha}. \tag{5.85}$$

So, the signal samples whose time index lies inside the time interval $[\beta(n), \beta(n+1)]$ have its phase compensated through the multiplication by $\mathrm{e}^{\mathrm{j}2\pi f_c(mt_s-\hat{\alpha}(mt_s))}$, resulting in the following signal

$$r_{\mathrm{p}}(m) = r(mt_s)\mathrm{e}^{\mathrm{j}2\pi f_c(mt_s-\hat{\alpha}(mt_s))} \tag{5.86}$$

$$= x(\alpha(mt_s))\mathrm{e}^{-\mathrm{j}2\pi f_c(mt_s-\alpha(mt_s))}\mathrm{e}^{\mathrm{j}2\pi f_c(mt_s-\hat{\alpha}(mt_s))}. \tag{5.87}$$

In the following step, the signal $r_{\mathrm{p}}(\cdot)$ passes through the filter:

$$r_{\mathrm{MF,r_5}} = (r_{\mathrm{p}} * p_1)(m), \tag{5.88}$$

with $p_1(m) = p^*(-m)$. Notice that this filter possess the same shape as the pulse situated at the transmitter side.

After this filtering operation, one sample of the signal $r_{\mathrm{MF,r_5}}$ is selected using the estimated information of $\beta(n+1)$ as

$$\widehat{\underline{s}}_{\mathrm{r_5}}(n+1) \;\; = \;\; r_{\mathrm{MF,r_5}}(\beta(n+1)) \tag{5.89}$$

leading to the estimated symbol.

It should be emphasize in the codes for Receiver 5, we rounded the obtained variable values towards the nearest integer number. In future works, we might develop and explore distinct algorithms for a performance improvement of Receiver 5.

5.2.2 Simulation Results

We ran some simulations in order to measure de MSE of the estimated symbols considering all the aforementioned receiver types. The MSE was calculated according to Eq. (5.47).

In this set of simulations, the following parameters were used: the carrier frequency was $f_{\mathrm{c}} = 8$ kHz, the sampling period was $t_s = 0.02$ ms (or $f_s = 50$ kHz). We generated 10 blocks of symbols, with 1000 symbols each block, and each symbol was randomly generated as $\underline{s} \in \{-1, +1\}$. Each symbol was mapped to an SRRC pulse, whose parameters were: roll-off factor of $\alpha = 0.5$, a filter span of 5 symbols ($F_{\mathrm{span}} = 5$), and $sps = 20$, meaning one pulse SRRC lasts for 101 samples. The resulting signal bandwidth is $B = 2.5$ kHz, with an bandwidth excess of 1.25 kHz. In the case of the second receiver, 11 branches were assumed, whereas each branch corresponds to one of these relative velocity (in m/s): $v \in \{-20, -15, -8, -5, -1, 0, 1, 5, 8, 15, 20\}$. As the pulse SRRC might not assume an integer value, we rounded towards the nearest integer. Likewise, the equally spaced sampling points of each branch might not assume integer values, so we rounded again towards the nearest integer. Once more, the first block of symbols were used for choosing the branch with the highest correlation. As this system model has a phase component that is very sensible to numerical imprecision, we ran 100 simulations.

At the receiver side, we employed a lowpass filter with the following specifications. The filter order was set to 20, the filter cutoff frequency was set to 11.25 kHz,

and the filter was designed with a Hamming window.

The obtained MSE values are shown in Tables 5.6, 5.7 for a fixed relative velocity, and for a sound speed of $c = 1500$ m/s. As in the previous model, the estimated symbols $\widehat{\underline{s}}(n)$ are not quantized, and in the case with $v = 0$ m/s, the estimated symbols were supposed to have unitary energy, what would result in a zero MSE. However, once more, this behavior is not observed in Tables 5.6, 5.7 due to finite time support of the pulses SRRC, and to numerical imprecision in Matlab.

As observed from Table 5.6, the resulting MSE per symbol is higher for Receiver 1 for all relative velocities. Considering Receiver 2, if it has a branch that corresponds exactly to the experienced relative movement, it is capable of dealing with the Doppler effect, thus having small MSE values. Otherwise, if Receiver 2 does not have a "perfect" match branch, the MSE value is high. For Receiver 3, as the relative velocity decreases, the MSE also decreases. This behavior was expected because the phase distortion is lower for small velocities. Despite the velocity, Receiver 4 was able to manage the Doppler effect, what resulted in a lower value for the MSE for all cases. It was observed a small variation in MSE for this receiver, but it does not seem to have a relationship with the velocity. Receiver 5 also got small values for the MSE, although this values are a bit higher than the ones obtained by Receiver 4 (Algorith 1). Notice that Receiver 5 has strict lower computational complexity than Receiver 4, because the latter adapts the pulse shaping format.

Table 5.6: MSE per symbol

Velocity	Rec. 1	Rec. 2	Rec. 3	Rec. 4 (alg. 1)	Rec. 5
$v = 20$ m/s	1.87	4.61×10^{-4}	1.62×10^{-1}	3.70×10^{-4}	2.04×10^{-3}
$v = 15$ m/s	1.87	3.50×10^{-4}	0.92×10^{-1}	1.66×10^{-4}	1.31×10^{-3}
$v = 12$ m/s	1.88	1.88	5.89×10^{-2}	1.53×10^{-4}	9.63×10^{-4}
$v = 10$ m/s	1.88	1.88	4.11×10^{-2}	1.92×10^{-4}	7.81×10^{-4}
$v = 8$ m/s	1.88	5.26×10^{-4}	2.64×10^{-2}	2.67×10^{-4}	6.30×10^{-4}
$v = 5$ m/s	1.88	4.59×10^{-4}	1.05×10^{-2}	1.89×10^{-4}	4.65×10^{-4}
$v = 1$ m/s	1.88	3.62×10^{-4}	7.64×10^{-4}	0.83×10^{-4}	3.62×10^{-4}
$v = 0.5$ m/s	1.89	1.89	4.59×10^{-4}	0.79×10^{-4}	3.59×10^{-4}
$v = 0$ m/s	0.77×10^{-4}	0.77×10^{-4}	0.77×10^{-4}	0.77×10^{-4}	0.77×10^{-4}
$v = -15$ m/s	1.87	3.60×10^{-4}	8.99×10^{-2}	1.72×10^{-4}	1.32×10^{-3}

Table 5.7 shows the MSE for each algorithm type of Receiver 4. As noticed, the first algorithm achieved a better performance than the other for almost all cases. Besides that, we observe that some MSE values are lower for some higher velocities. The explanation of this behavior is similar to the one presented in Subsection 5.1.3. Matlab numerical imprecision, the finite time support of the pulse SRRC, and the rounding operations performed by each algorithm might cause variations in the MSE results.

Table 5.7: MSE ($\times 10^{-4}$) per symbol for algorithms of Receiver 4

Velocity	Alg. 1	Alg. 2	Alg. 3,1	Alg. 3,2	Alg. 3	Alg. 4
$v = 20$ m/s	3.70	3.43	5.70	5.50	6.37	6.21
$v = 15$ m/s	1.66	4.32	2.40	1.74	4.38	4.46
$v = 12$ m/s	1.53	2.85	9.17	8.87	10.22	9.16
$v = 10$ m/s	1.92	2.12	7.04	6.80	7.79	7.52
$v = 8$ m/s	2.67	1.71	5.70	5.53	6.28	6.05
$v = 5$ m/s	1.89	1.74	3.92	3.68	4.66	4.52
$v = 1$ m/s	0.83	2.99	1.90	1.34	3.59	3.64
$v = 0.5$ m/s	0.79	3.24	1.67	1.05	3.54	3.62
$v = 0$ m/s	0.77	0.77	1.38	0.77	3.04	0.77
$v = -15$ m/s	1.72	4.50	2.49	1.80	4.57	4.67

5.3 Passband System: Doppler Compensation for a Multipath Channel

The objective of this section is to show that the Doppler compensation and estimation can be performed independently of the number of channel paths (if the Doppler effect is equal in all paths). In order words, we would be able to employ the four previous mentioned receivers.

The signal modeling is the same from the previous section. Each symbol $\underline{s}$ is mapped into a waveform resulting in the signal of Eq. (5.48). This signal is modulated for being centered around the frequency f_c

$$x_{\mathrm{PB}}(t) = 2\Re\left\{x(t)\mathrm{e}^{\mathrm{j}2\pi f_c t}\right\}. \tag{5.90}$$

The signal is transmitted through the channel. The channel has multipath and Doppler effect

$$h(t,\tau) = \sum_{l=0}^{L} h_l(t)\delta(\tau - \tau_l(t)), \tag{5.91}$$

where $L+1$ is the channel length, and $\tau_l(t)$ is the time delay of path l.

The received signal is given by

$$r_{\mathrm{PB}}(t) \;=\; \sum_{l=0}^{L} h_l(t)x_{\mathrm{PB}}(t - \tau_l(t)). \tag{5.92}$$

The removal of the carrier frequency results in the signal:

$$\begin{aligned} r_{\mathrm{BB}}(t) &= r_{\mathrm{PB}}(t)\mathrm{e}^{-\mathrm{j}2\pi f_{\mathrm{c}}t} \\ &= \sum_{l=0}^{L} h_l(t)\left\{x(t-\tau_l(t))\mathrm{e}^{-\mathrm{j}2\pi f_{\mathrm{c}}\tau_l(t)}\right\} \\ &\quad + \sum_{l=0}^{L} h_l(t)\left\{x^*(t-\tau_l(t))\mathrm{e}^{-\mathrm{j}2\pi f_{\mathrm{c}}(2t-\tau_l(t))}\right\}. \end{aligned} \tag{5.93}$$

Removing the unwanted signal components of Eq. (5.93) with a lowpass filter, leads to the following signal:

$$r(t) = \sum_{l=0}^{L} h_l(t)x(t-\tau_l(t))\mathrm{e}^{-\mathrm{j}2\pi f_{\mathrm{c}}\tau_l(t)}. \tag{5.94}$$

So, if we consider that

$$\tau_l(t) = a_0^{(l)} - a_1 t + \frac{1}{2}a_2 t^2 - \frac{1}{6}a_3 t^3 + \cdots + \frac{(-1)^{N_{\mathrm{delay}}}}{N_{\mathrm{delay}}!}a_{N_{\mathrm{delay}}}t^{N_{\mathrm{delay}}}, \tag{5.95}$$

meaning that each path faces a distinct delay but an equal Doppler effect, we can partition into two independent stages the compensation of these two channel effects: multipath effect and Doppler effect. That is, the receiver might have two distinct and independent stages for reversing (and taking profit) of these two channel features. Notice that this processing division can be performed because the parameters that multiply the variable t are constants.

5.3.1 Illustrative case

In order to illustrate more intuitively the above-mentioned fact, we consider a two-path channel, whose gains are time-invariant, and that $\tau_l(t) = a_0^{(l)} - a_1 t$. So the signal of Eq. (5.94) can be rewritten as

$$r(t) = h_0 x(t - a_0^{(0)} + a_1 t)\mathrm{e}^{\mathrm{j}2\pi f_{\mathrm{c}}(a_0^{(0)} - a_1 t)} + h_1 x(t - a_0^{(1)} + a_1 t)\mathrm{e}^{\mathrm{j}2\pi f_{\mathrm{c}}(a_0^{(1)} - a_1 t)}. \tag{5.96}$$

Rewriting Eq. (5.96) as

$$r(t) = \left(h_0 x(t - a_0^{(0)} + a_1 t)\mathrm{e}^{\mathrm{j}2\pi f_c a_0^{(0)}} + h_1 x(t - a_0^{(1)} + a_1 t)\mathrm{e}^{\mathrm{j}2\pi f_c a_0^{(1)}}\right)\mathrm{e}^{-\mathrm{j}2\pi f_{\mathrm{c}} a_1 t},$$

where h_0 and h_1 are the time-invariant channel gains. If a good phase estimation and compensation be performed, that is $a = a_1$, we will have the following signal

$$\begin{aligned} r_1(t) &= r(t)\mathrm{e}^{\mathrm{j}2\pi f_c a t} \\ &= \left(h_0 x(t - a_0^{(0)} + a_1 t)\mathrm{e}^{\mathrm{j}2\pi f_c a_0^{(0)}} + h_1 x(t - a_0^{(1)} + a_1 t)\mathrm{e}^{\mathrm{j}2\pi f_c a_0^{(1)}}\right). \quad (5.97) \end{aligned}$$

Notice that this signal has only the time-warping effect, that can be compensated with an adaptive correlation filter. Considering a good estimation and compensation of this phenomena, the resulting signal will be

$$r_2(t) = \left(h_0 x(t - a_0^{(0)})\mathrm{e}^{\mathrm{j}2\pi f_c a_0^{(0)}} + h_1 x(t - a_0^{(1)})\mathrm{e}^{\mathrm{j}2\pi f_c a_0^{(1)}}\right). \quad (5.98)$$

It is important to observe that the signal described in Eq. (5.98) has a structure resembling the signal structure depicted in Eq. (C.6).

In order to clarify this relationship, we can rewrite Eq. (5.98) as

$$r_2(t) = \left(h_0 \mathrm{e}^{\mathrm{j}2\pi f_c a_0^{(0)}} x(t - a_0^{(0)}) + h_1 \mathrm{e}^{\mathrm{j}2\pi f_c a_0^{(1)}} x(t - a_0^{(1)})\right). \quad (5.99)$$

The signal described in Eq. (5.99) can be sampled at $t_m = mT$, resulting in

$$r_2(m) = \left(h_0 \mathrm{e}^{\mathrm{j}2\pi f_c a_0^{(0)}} x(m - l_0) + h_1 \mathrm{e}^{\mathrm{j}2\pi f_c a_0^{(1)}} x(m - l_1)\right), \quad (5.100)$$

whereas $l_0 = a_0^{(0)}$ and $l_1 = a_0^{(1)}$ can be interpreted as the channel delay of each path. Eq. (5.100) can be rewritten as

$$r_2(m) = \left(h_{\mathrm{l}_0} x(m - l_0) + h_{\mathrm{l}_1} x(m - l_1)\right), \quad (5.101)$$

with $h_{\mathrm{l}_0} = h_0 \mathrm{e}^{\mathrm{j}2\pi f_c a_0^{(0)}}$ and $h_{\mathrm{l}_1} = h_1 \mathrm{e}^{\mathrm{j}2\pi f_c a_0^{(1)}}$.

Notice that the signal described in Eq. (5.101) is similar to the signal depicted in Eq. (3.20). So, these signals might be estimated using the same techniques. As a possible signal estimation of Eq. (3.20) was previously presented, we can conclude that we might be able to divide in two independent steps the processing and removal of these two channel effects.

5.4 Summary

In this chapter we proposed two distinct receiver types for compensating Doppler effects. We showed that our proposed receiver achieves lower MSE results than the other receiver types considered. This improvement in the system performance was observed for all tested relative velocities.

Chapter 6

Simulation Results

The objective of this chapter is to evaluate and compare the performance of the receivers presented in Chapter 5. We consider the communication setup described in Chapter 3 for computing the BER of each distinct receiver type.

In Section 6.1, we present the implemented system and some possible configuration parameters. In Subsection 6.1.1, we describe the procedure performed for emulating an underwater acoustic channel. In Subsection 6.1.2, we present the signal processing tools employed for generating random noise samples, which follow a power spectral density (PSD) of an environmental noise data collected in situ.

In Section 6.2, we show some simulation results considering single carrier and multicarrier systems. We also analyze the receivers' performance for distinct relative velocities and digital modulation constellation parameters. Section 6.3 summarizes the main results and analyses performed in this chapter.

6.1 Implemented System

In order to evaluate the proposed technique for Doppler compensation and estimation in Chapter 5, we implemented a physical layer simulator. A block diagram containing all the implemented processing blocks is shown in Figure 6.1.

A mathematical model of all processing blocks of the transmitter side was presented in Chapter 3, while the blocks modeling at the receiver side were described in Chapter 5. A brief description of these processing blocks will be provided hereafter.

The channel encoder is the first processing block of Figure 6.1. This is an optional simulator feature. It was considered a convolutional code and a random interleaver. At the receiver side, we utilized a Viterbi decoder with a hard decision. Some codification parameters may be modified according to the simulation purpose.

The second block is a digital modulator. We considered a quadrature amplitude modulation (QAM) constellation, with an option of changing the number of bits needed to represent a QAM symbol.

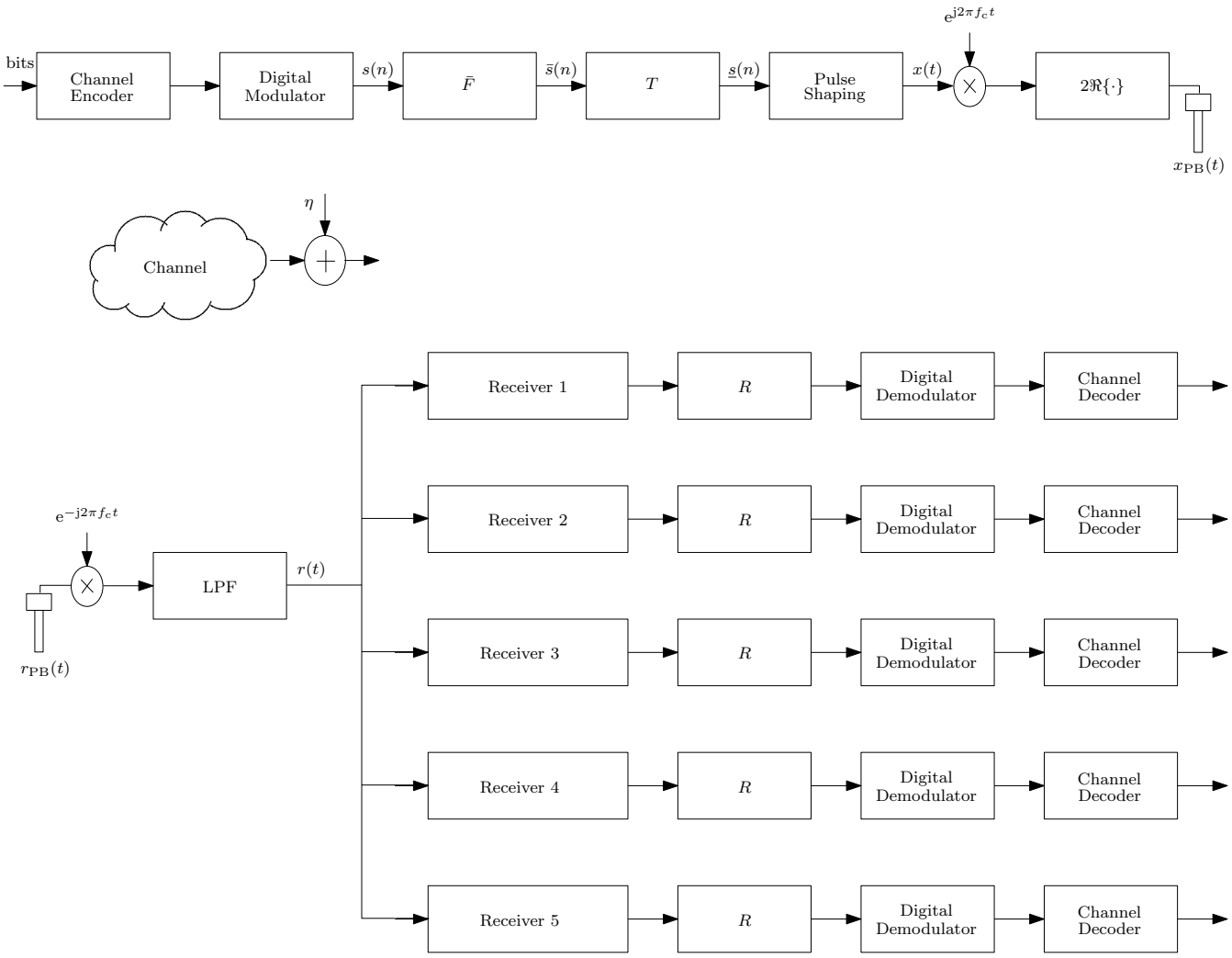

Figure 6.1: Implemented System.

The next block is called as a transmitter block. This block will perform an FFT or no processing at the input signal, determining if the transmission system will be Single Carrier or Multicarrier.

The next stage is the insertion of signal redundancy. The type of signal redundancy available at the moment is the zero padding. The amount of zeros to be added is a variable parameter, that may have any length between the channel length and half of the channel length. In other words, we consider systems that might pursue full, reduced or minimum redundancy guard interval.

The pulse shaping block increases the signal rate from the symbol rate to the sample rate. Before this stage, the signal period was T. After this processing, the signal period is $t_s = \frac{T}{sps}$, where sps stands for samples per symbol. We implemented an SRRC, whereas some parameters might be modified: the roll-off factor and the filter Span.

The signal that is at the higher rate is modulated to be around the specified carrier frequency f_c, and only the real part of this signal is extracted for transmission.

Any other possible system peculiarity will be reported in the respective simulation setup.

6.1.1 Emulated Channel

As the received signal is described by the equation

$$r_{\mathrm{PB}}(t) \quad = \quad \sum_{l=0}^{L} h_l x_{\mathrm{PB}}(t - \tau(t)) + \eta_{\mathrm{PB}}(t), \tag{6.1}$$

we first induce the Doppler effect in the transmitted signal $x_{\mathrm{PB}}(t)$, then we convolve this signal with the channel coefficient gains, that are time-invariant as will be described hereafter.

Multipath Channel

The multipath channel was calculated with Bellhop program as shown in Chapter 3 (Section 3.2). This channel impulse response was computed for a distance of one kilometer between transmitter and receiver. The transmitter was situated at a depth of 15 meters and the receiver at 10 meters. Figure 6.2 shows the channel impulse response.

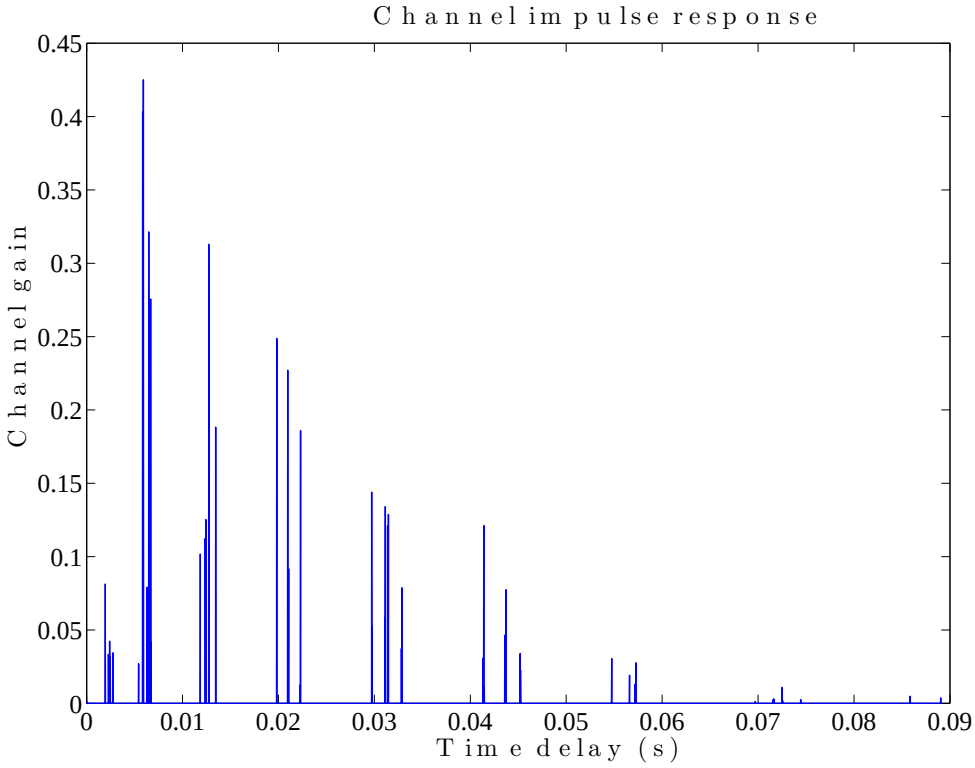

Figure 6.2: Channel impulse response.

As observed from Figure 6.2, this channel pursues characteristics of underwater acoustic channel. It has a large delay spread, the channel path are sparse, and the first path arrival is not the strongest path [79].

6.1.2 Acoustic Noise

The noise that is added to the signal in this simulator is generated as follows. With a recorded noise file, which was obtained from Brazilian Navy, we estimate its power spectral density (PSD). We employ the Yule-Walker method for calculating the equivalent autoregressive (AR) all-pole model reference.

We generate a white, Gaussian noise that is convolved with this AR filter coefficients, giving rise to a noise signal that has the same PSD as the original recorded noise. As the noise was recorded with a sample rate of $f_{\mathrm{n}} = 44.1$ kHz, we need modify the noise signal rate in order to match f_s. Distinct noise samples are generated at each simulation run.

6.2 Full Redundancy Case

Our objective in this set of simulations is to evaluate and compare the performance of the five receiver types with respect to distinct relative movements and digital constellation modulations.

In this first set of simulations, we utilized the following parameters: the carrier frequency was $f_{\mathrm{c}} = 8$ kHz, the sampling period was $t_s = 0.02$ ms (or $f_s = 50$ kHz). We generated 10 blocks of symbols, with 512 symbols each block, and each symbol was randomly generated. Each symbol was mapped to an SRRC pulse, whose parameters were: roll-off factor of $\alpha = 0.5$, a filter span of 5 symbols ($F_{\mathrm{span}} = 5$), and $sps = 20$, meaning one pulse SRRC lasts for 101 samples. The resulting signal bandwidth is $B = 2.5$ kHz, with an bandwidth excess of 1.25 kHz. As the channel is represented in the higher rate (f_s) with 4453 samples, we inserted 222 zeros[1] as a guard interval. The sound speed was considered to be $c = 1500$ m/s.

At the receiver side, we employed a lowpass filter with the following specifications. The filter order was set to 20, the filter cutoff frequency was set to 11.25 kHz, and the filter was designed with a Hamming window.

For the second receiver, 11 branches were employed, whereas each branch corresponds to the following relative velocity (in m/s): $v \in \{-20, -15, -8, -5, -1, 0, 1, 5, 8, 15, 20\}$. Besides that, as the pulse SRRC might not assume an integer value, we rounded towards the nearest integer. Likewise, the equally spaced sampling points of each branch might not assume integer values,

[1] These zeros are at the symbol rate: T

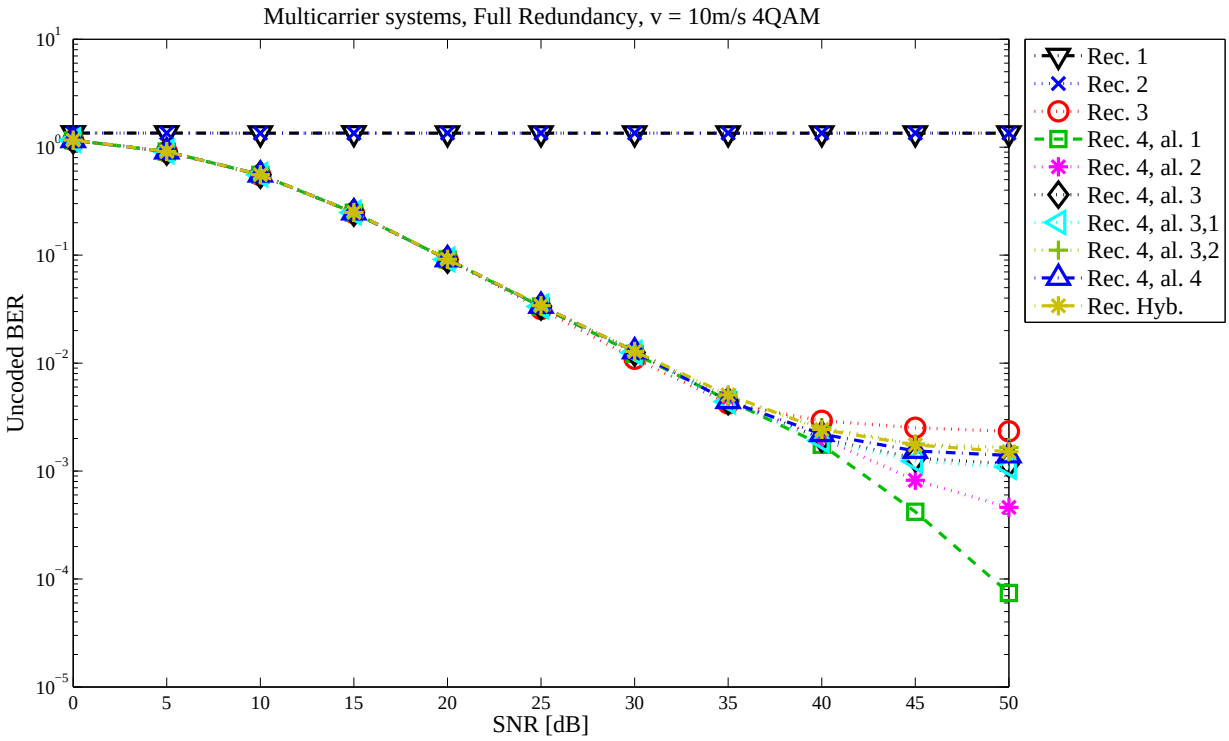

Figure 6.3: Multicarrier system with 4 QAM constellation and relative movement of $v = 10$ m/s.

so we rounded again towards the nearest integer. The first block of symbols was employed for selecting the branch with the highest correlation.

We performed 150 monte carlo runs. The first block is used for channel estimation. The channel equalization was performed at the frequency domain for the multicarrier system. As the equalization of the single carrier system faced a peculiar behavior in some scenario setups, we utilized the channel estimation performed for the multicarrier system in the single-carrier case. As our main objective is to evaluate the distinct Doppler effect techniques, this will not influence our analysis.

At the transmitter side we calculated the signal power, and in order to emulate a scenario with a certain SNR, the noise power was modified accordingly.

Multicarrier System

We implemented a multicarrier system for running this first set of simulations. Figures 6.3, 6.4 and 6.5 show the system performance of a multicarrier system with a 4QAM constellation considering $v = 10$ m/s, $v = 7$ m/s and $v = 0.1$ m/s, respectively.

From these figures, one can verify that Receivers 1 and 2 were not able to recover the transmitted information for all SNR values. The system performance obtained in Receiver 1 shows that, if no method for Doppler compensation and estimation be

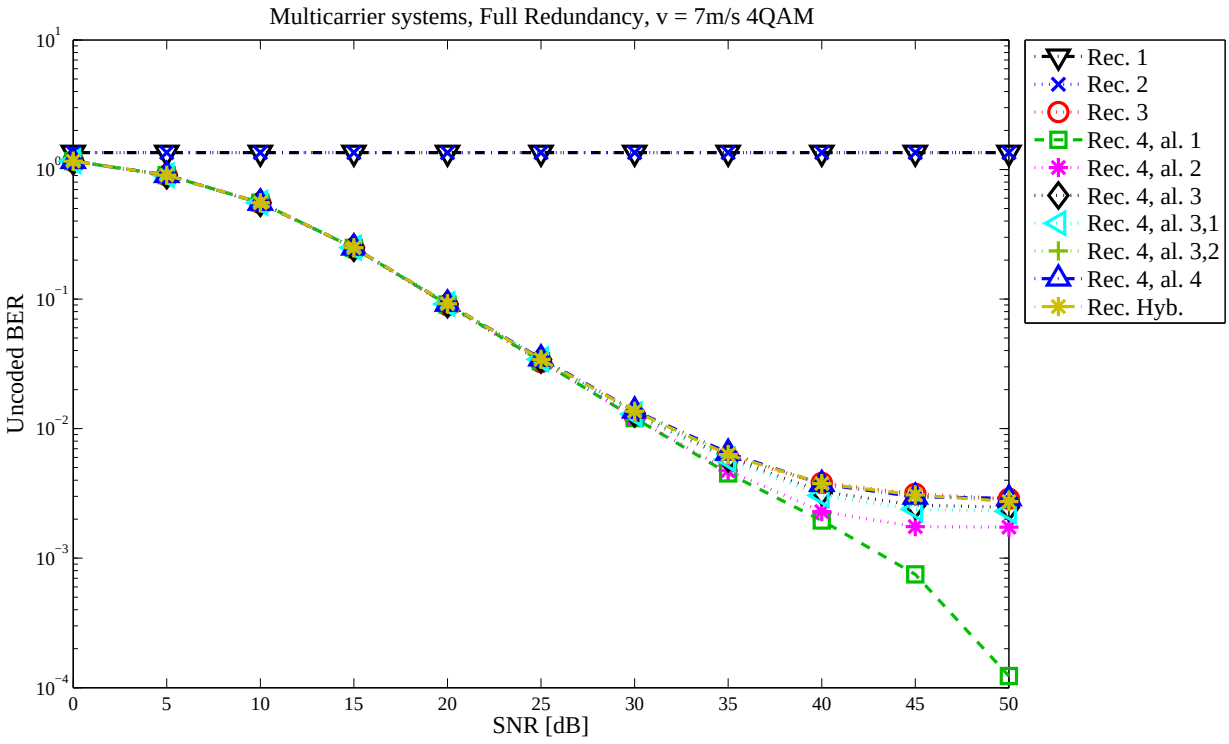

Figure 6.4: Multicarrier system with 4 QAM constellation and relative movement of $v = 7$ m/s.

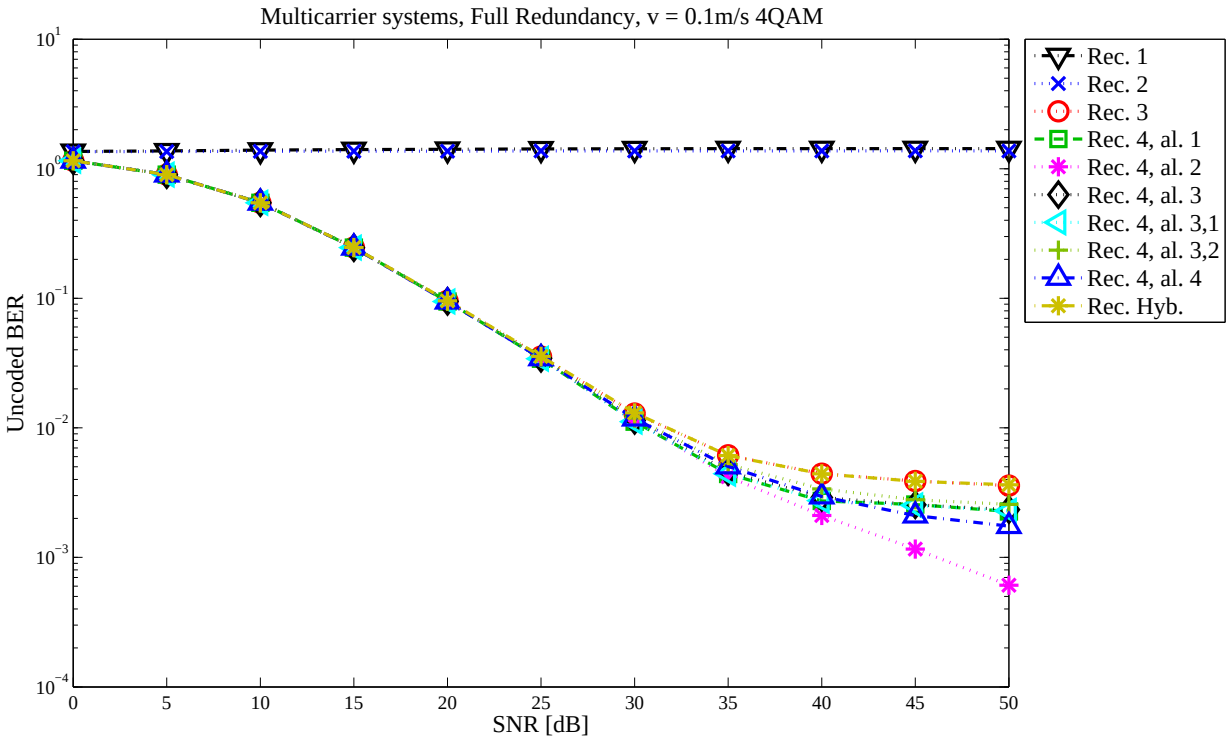

Figure 6.5: Multicarrier system with 4 QAM constellation and relative movement of $v = 0.1$ m/s.

employed, even for small relative movements (see Figure 6.5), the receiver will not be able to recover the transmitted information, and the communication can not be established.

The performance of Receiver 2 induces us to conclude that its employed technique for Doppler compensation and estimation is not effective if no receiver branch matches exactly the relative movement experienced. This requirement seems to limit the usage of this receiver type for very specific situations.

As seen from Figures 6.3, 6.4 and 6.5, Receiver 3 is able to recover the majority of the transmitted information. The BER obtained for this receiver decreases with the augmentation of the transmitter power, or equivalently with the increase of the SNR value. However, this receiver performance seems to be bounded (see Figures 6.3, 6.4 and 6.5), i.e., even if a higher SNR value be possible, this system performance will not get any improvement.

As observed in Figures 6.3, 6.4 and 6.5, all the proposed algorithms of Receiver 4 were able to deal with the Doppler effect. For high relative velocities, such as $v = 10$ m/s and $v = 7$ m/s, the first algorithm (Rec.4, alg. 1) reached a performance improvement of at least one order of magnitude[2] for high SNR values. Even for small value of the relative velocity (see Figure 6.5), the second proposed algorithm of Receiver 4 got a performance improvement over Receiver 3 for high SNR values. The difference in the performance improvement observed in Figs. 6.3, 6.4 and 6.5 are related to Matlab numerical imprecision, the finite time support of the pulse SRRC, and the rounding operations performed by each algorithm, as widely discussed in Subsection 5.1.3.

As can be noticed, at least one algorithm of receiver 4 achieves a better system performance than the other receiver types for high SNR values. One can notice that the performance gain obtained by Receiver 4 compared to Receiver 3, is higher when the relative movement is higher, or in other words, the gain provided by our proposal receivers can be further noticed in environments with higher Doppler effects. However, it is important to say that this performance improvement is accompanied by an augmentation in computational complexity.

Receiver 5, also called as hybrid receiver in Figures 6.3, 6.4 and 6.5, was also able to deal with Doppler effect. Only for the scenario with the higher relative velocity ($v = 10$ m/s), that it was possible to perceive a system improvement compared with Receiver 3. For the other cases, the system performance seemed to have the same performance of Receiver 3.

We also ran simulations for observing if the proposed receivers might also provide performance gains for applications requiring higher throughput rates. Figures 6.6, 6.7 and 6.8 illustrate the system that employ a 64 QAM constellation, and

[2]Comparing to the performance of Receiver 3.

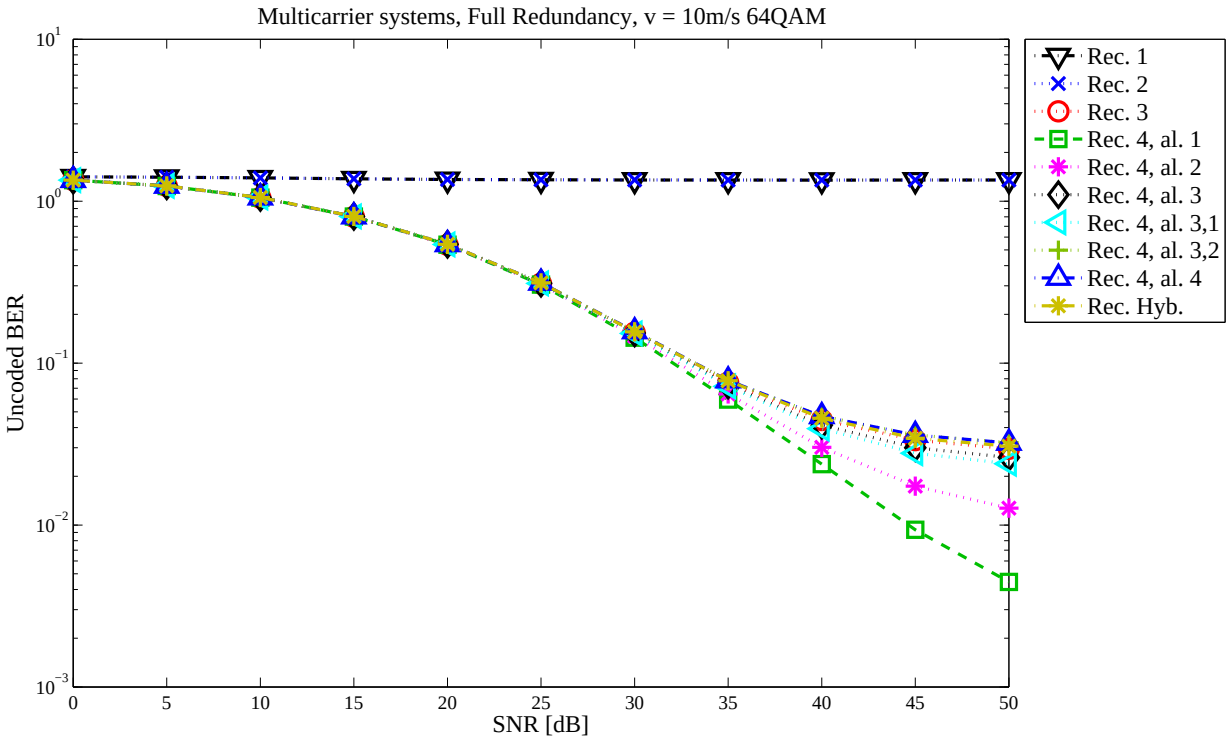

Figure 6.6: Multicarrier system with 64 QAM constellation and relative movement of $v = 10$ m/s.

with a relative movement of $v = 10$ m/s, $v = 7$ m/s and $v = 0.1$ m/s, respectively.

As observed in Figures 6.6, 6.7 and 6.8, all receivers reached similar performance ordering as before. However, as expected, for all receivers type the system performance was worse than the ones observed in Figures 6.3, 6.4 and 6.5. In order words, Receiver 1 and 3 were not able to recover the transmitted data. Receivers 3 and 5 managed to compensate Doppler effects showing similar performance. For the case of a richer constellation, algorithm 1 of Receiver 4 achieved the best system performance for high SNR values among the other algorithms and the other receiver types.

So, we can conclude the employment of Receiver 4 (with algorithm 1) in a multicarrier system provides a performance improvement for high SNR values, even for scenarios with high relative velocities and rich constellations.

Single-Carrier System

In this second set of simulations, we considered a single-carrier system. Figures 6.9, 6.10 and 6.11 show the single-carrier system performance employing 4QAM constellation for relative velocities of $v = 10$ m/s, $v = 7$ m/s and $v = 0.1$ m/s, respectively.

Just Receivers 1 and 2 were not able to deal with Doppler effect for these cases.

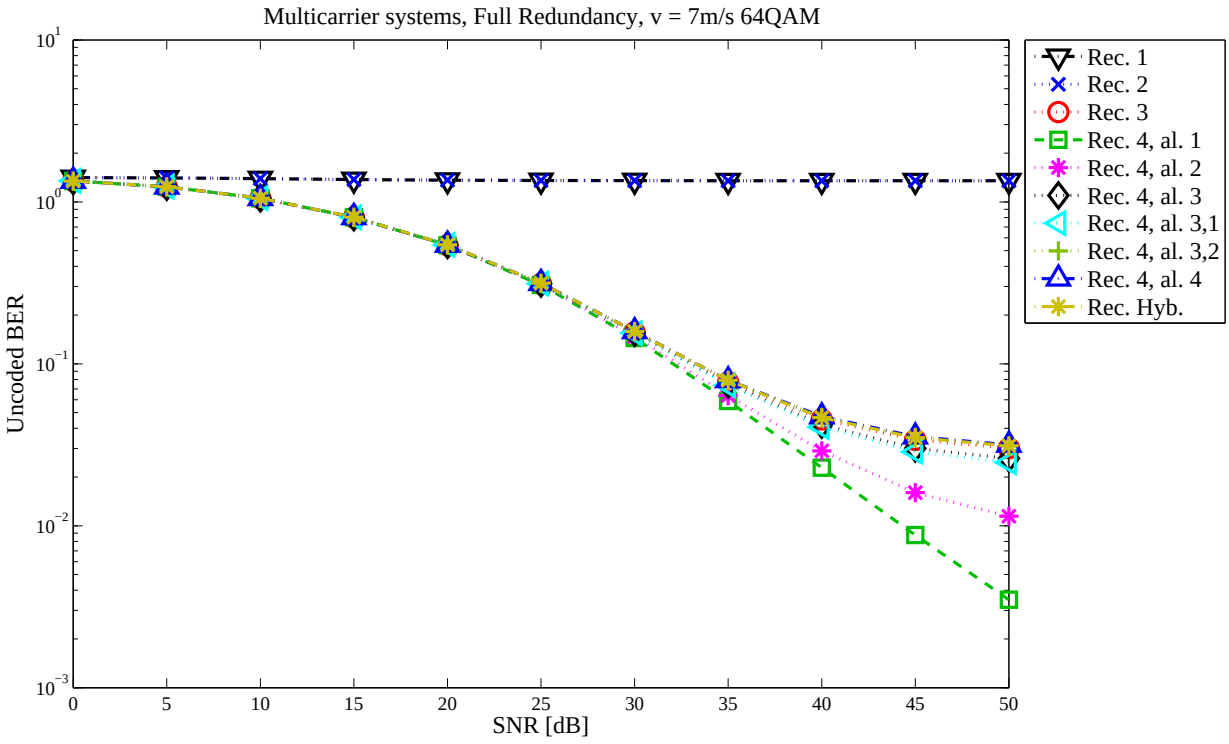

Figure 6.7: Multicarrier system with 64 QAM constellation and relative movement of $v = 7$ m/s.

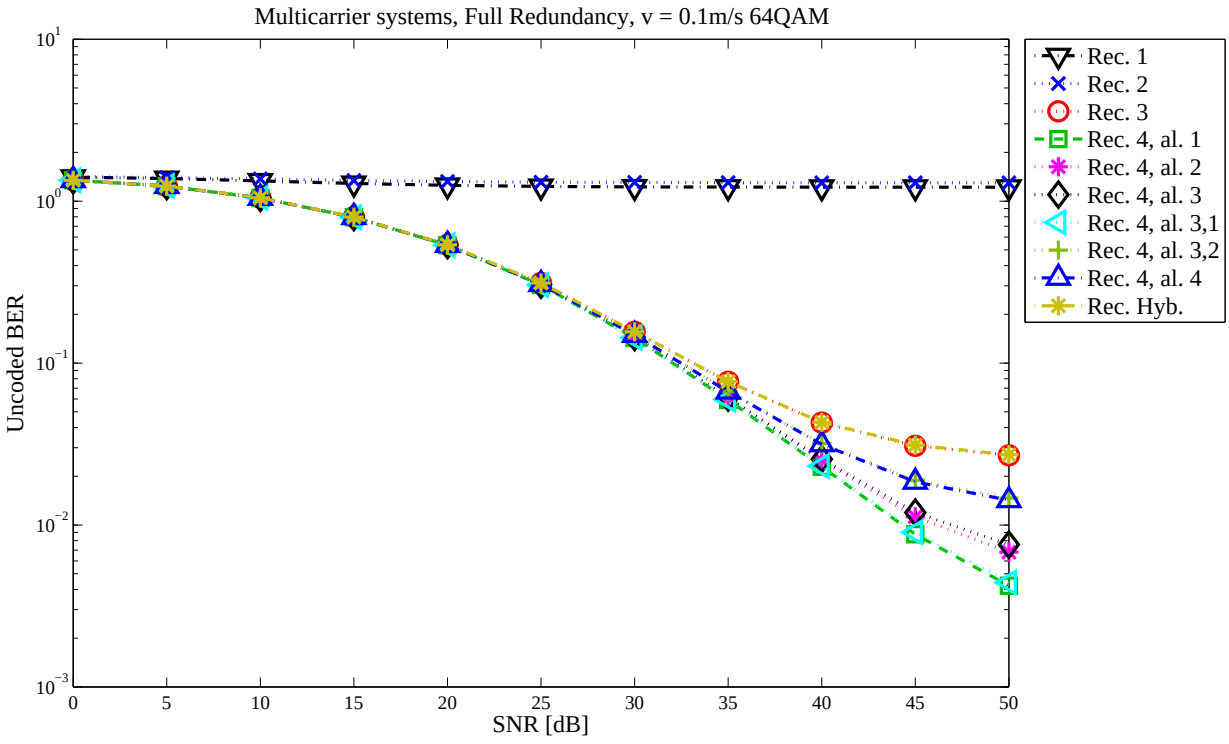

Figure 6.8: Multicarrier system with 64 QAM constellation and relative movement of $v = 0.1$ m/s.

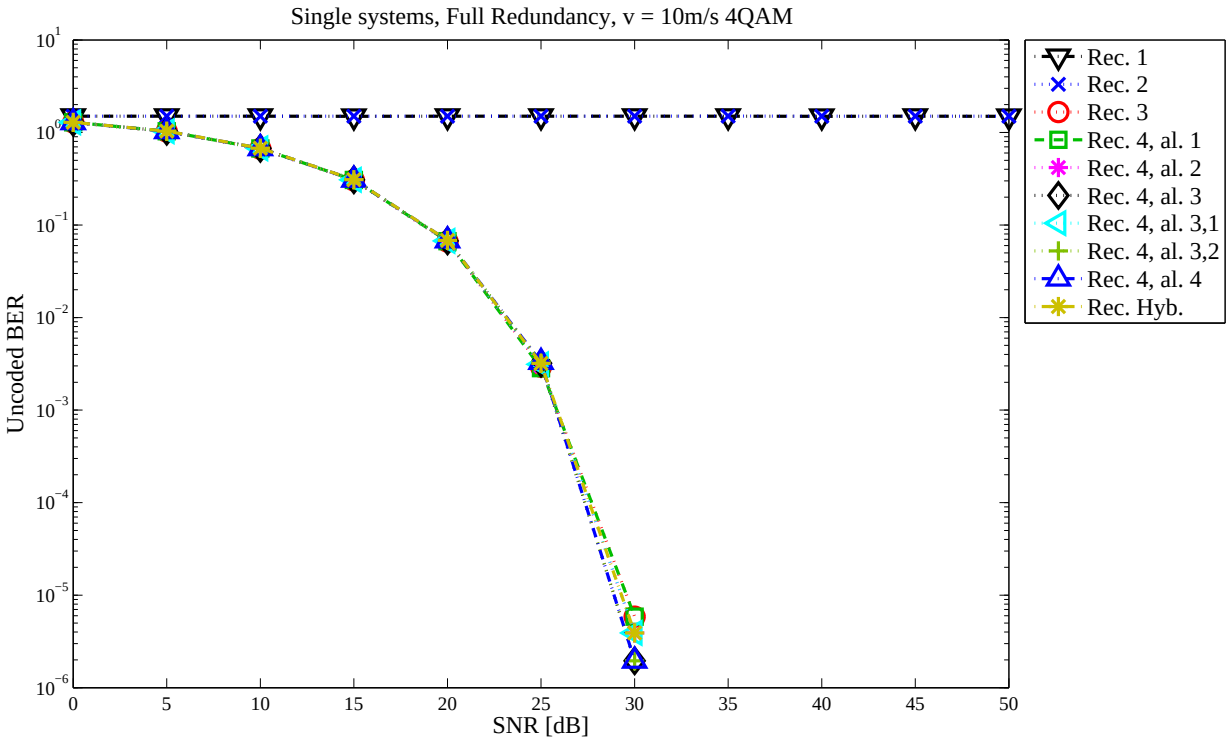

Figure 6.9: Single-carrier system with 4 QAM constellation and relative movement of $v = 10$ m/s.

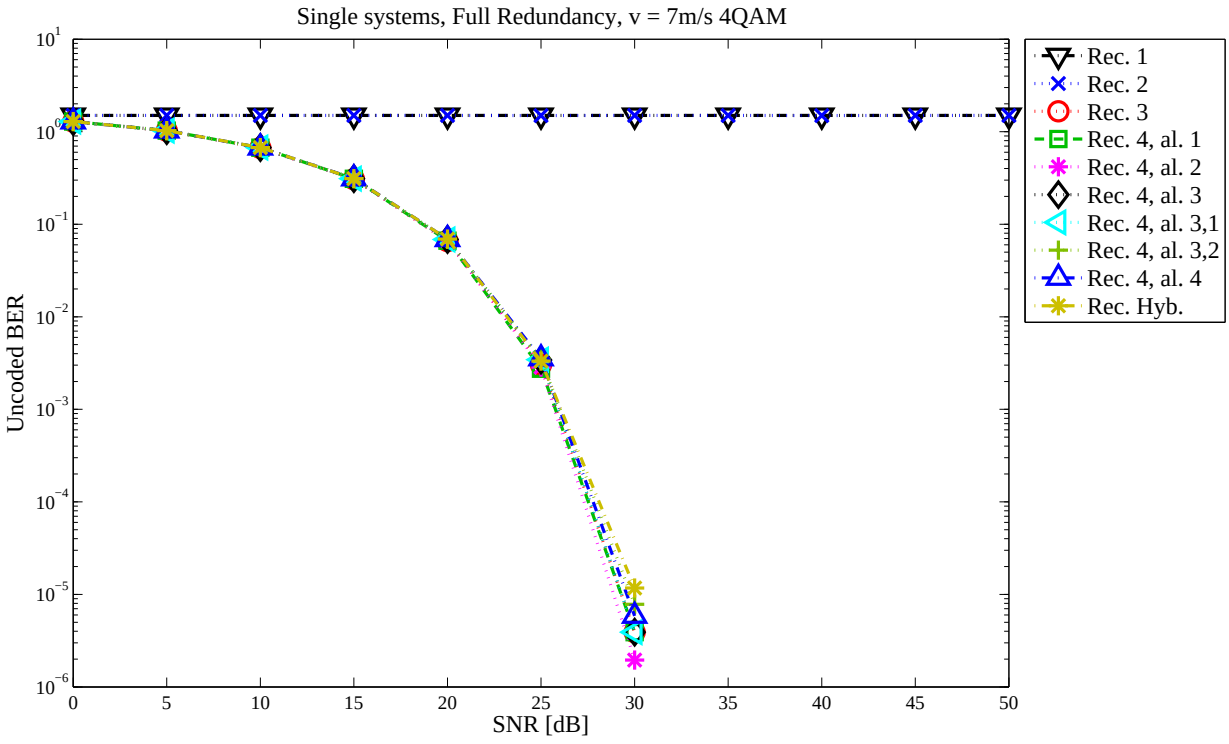

Figure 6.10: Single-carrier system with 4 QAM constellation and relative movement of $v = 7$ m/s.

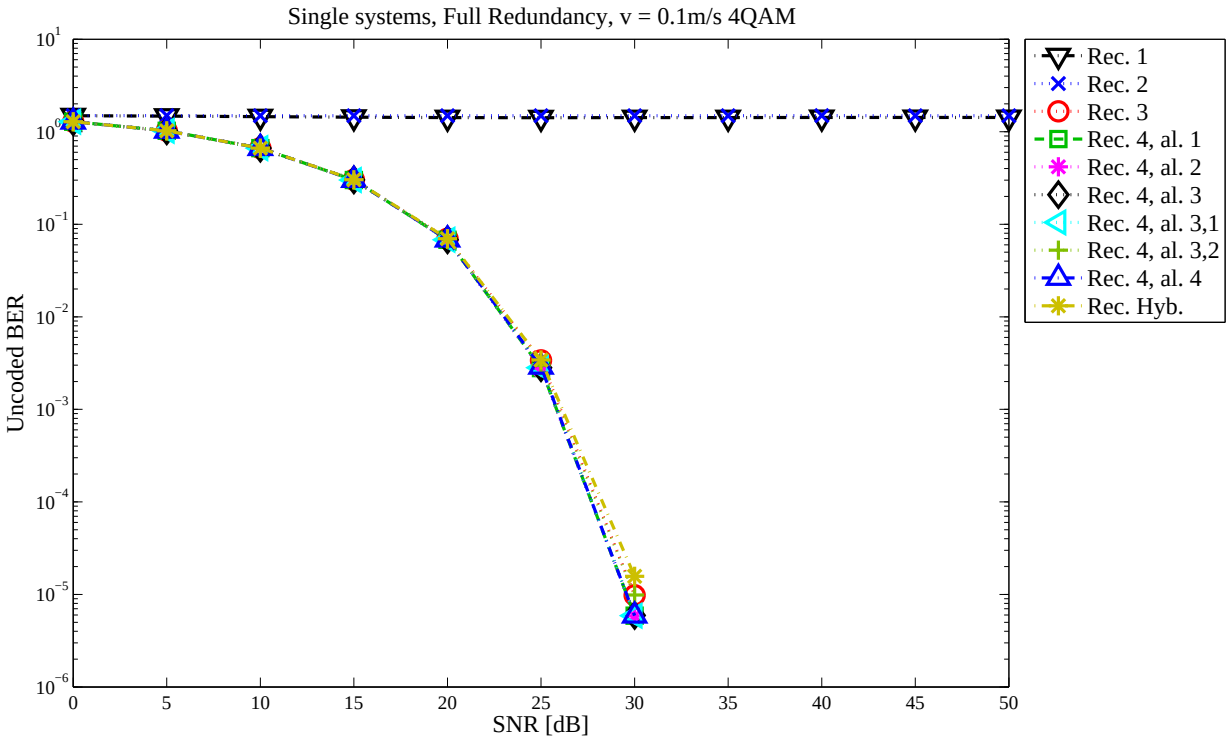

Figure 6.11: Single-carrier system with 4 QAM constellation and relative movement of $v = 0.1$ m/s.

The performance of Receivers 3, 4 and 5 seemed to be similar. It is possible to perceive that if the Doppler effect be appropriately compensated, the single-carrier system seems to be the better than multicarrier system when using a 4-QAM constellation.

We also ran simulations for single-carrier system with a 64-QAM constellation. Figures 6.12, 6.13 and 6.14 exhibit the SC system performance for a 64-QAM constellation for $v = 10$ m/s, $v = 7$ m/s and $v = 0.1$ m/s, respectively.

Once more, it is noticeable that Receivers 1 and 2 did not manage to recover the transmitted information, while the other receivers were capable of getting this data. The performance improvement of Receiver 4 (algorithm 1) is visible for high SNR values. For SNR = 50 dB, this receiver got a BER that is almost 2 order of magnitude lower than the BER obtained with Receiver 3 (see Figures 6.12, 6.13 and 6.14). Besides that, considering high SNR values, the other proposed algorithms for Receiver 4 reached a lower BER than the other receiver types.

Comparing single carrier and multicarrier systems, the first one seemed to got a better performance for high SNR values.

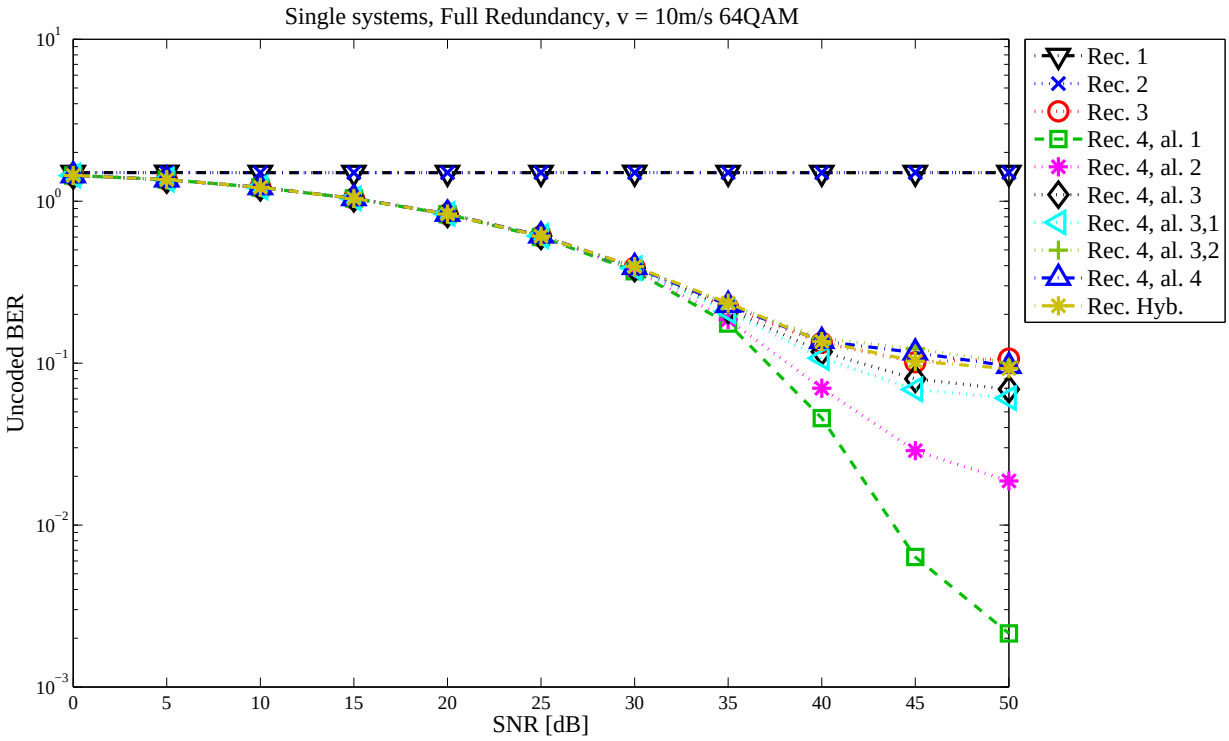

Figure 6.12: Single-carrier system with 64 QAM constellation and relative movement of $v = 10$ m/s.

6.3 Summary

As observed from simulations results, for Single Carrier and Multicarrier systems, our proposed receiver achieves a better system performance for high SNR values. We showed that the system improvement might be achieved with any relative velocity, and with dense digital signal constellation. Besides that, the performance gain in a single carrier system was higher than in multicarrier system considering the same parameters. However, one should be aware of inherent trade-off in Receiver 4: the computational cost is increased for achieving a lower bit error rate.

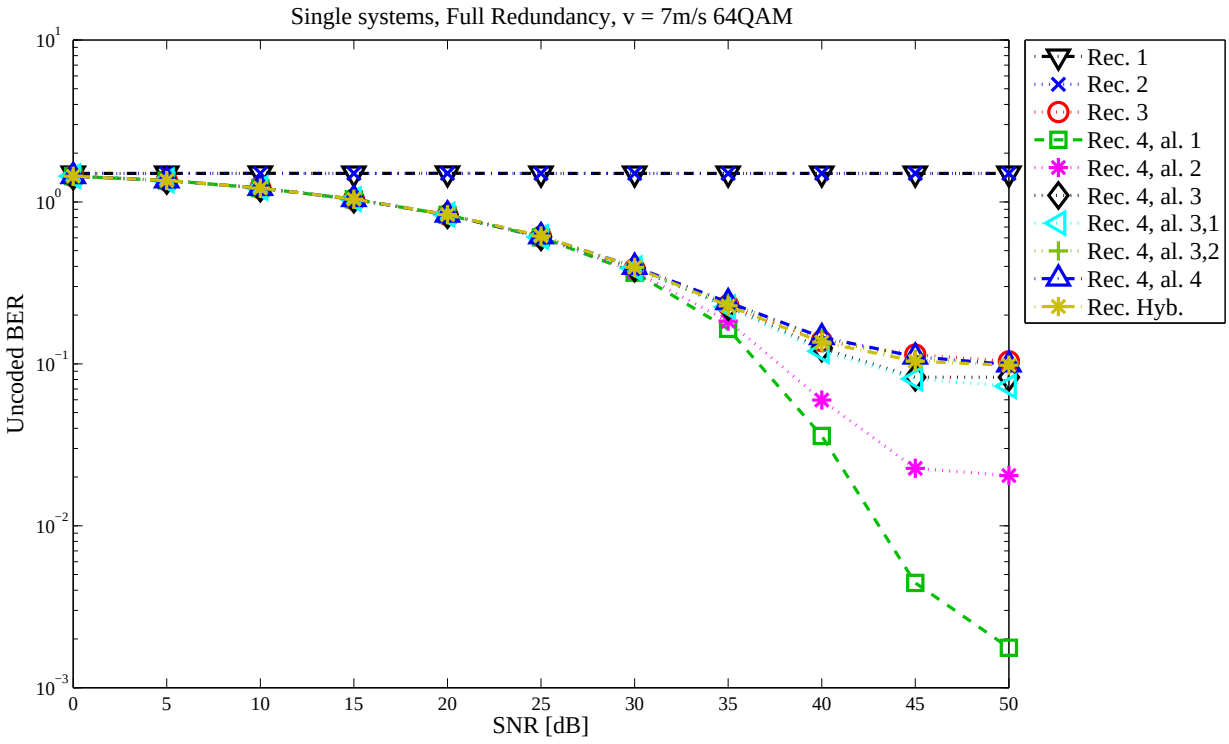

Figure 6.13: Single-carrier system with 64 QAM constellation and relative movement of $v = 7$ m/s.

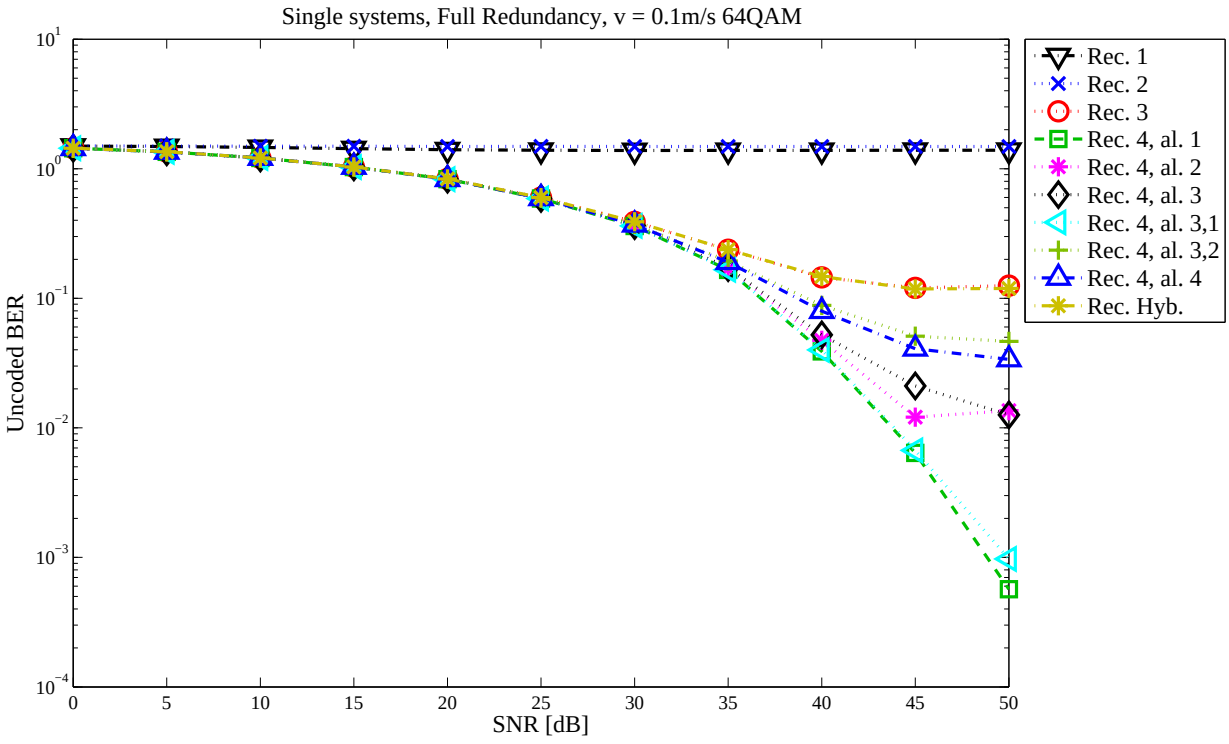

Figure 6.14: Single-carrier system with 64 QAM constellation and relative movement of $v = 0.1$ m/s.

Chapter 7

Conclusion

In this thesis, we presented a survey encompassing the three available technologies for underwater wireless communications: RF, optical and acoustics. We mapped the main features and drawbacks inherent to each technology, as well as their main challenges.

We proceeded by focusing on underwater acoustics communications. We showed an analyses and evaluation of the channel frequency response in the coast of Arraial do Cabo using data collected in situ. Following that, we presented the communication setup employed in this thesis.

As the Doppler effect is a significant hindrance for establishing an efficient acoustic communication link, we studied in detail this effect. We investigated some available solutions for overcoming this problem. Then, we performed an analysis of an existing Doppler compensation technique, and we proposed an algorithm simplification for addressing the case that no pilot symbol is available at the receiver side. Besides that, we proposed a simple strategy for determining how often this algorithm should be trained.

Our main contribution was the proposal of a new solution to deal with Doppler effects. We proposed to iteratively adapt the correlator filter situated at the receiver side. Besides that, we verified the requirement of removing the phase distortion of a signal that is at the higher sample rate, leading to an improvement in the signal estimation (despite its higher computational cost).

For testing and comparing our idea with other available techniques, we implemented a large communication setup. We performed some analysis of the impact of Doppler effect in Single Carrier and Multicarrier systems. We show that our proposed method might provide a reduction in the bit error rate under high values of signal-to-noise ratio, for any relative velocity between transmitter and receiver, and even for dense digital signal constellation.

7.1 Future work

Some possible future work are:

- Address how Doppler effect impacts Single Carrier and Multicarrier systems with reduced redundancy. The usage of reduced redundancy system might improve the system throughput;
- Develop other algorithms for updating the proposed adaptive correlator;
- Process the experimental data acquired in the experiment with Brazilian Navy for evaluating the distinct Doppler effect techniques;
- Study other pulse shapes that satisfy Nyquist criteria, and the impact of the selection of the pulse shaping in the underwater acoustic communication.

Appendix A

List of Publications

In this chapter, we list the research work of this thesis that have already been published. It is important to highlight that we are writing a journal article with the major thesis contributions.

A.1 Journal Publication

[J1] Gussen, C. M. G.; Diniz, P. S. R. ; Campos, M. L. R. ; Martins, W. A. ; Costa, F. M. ; Gois, J. N., "A Survey of Underwater Wireless Communication Technologies, " *Journal of Communication and Information Systems (JCIS)*, vol. 31, pp. 242–255, 2016.

A.2 Conference Publications

[C2] Gussen, C. M. G.; de Campos, M. L. R. ; Diniz, P. S. R. ; Xavier, F. C., "On the Channel Frequency Response in Shallow Seawater," *Proceedings of the 3rd International Conference & Exhibition on Underwater Acoustics, 2015*, Crete, Greece, June 2015.

[C1] Gussen, C. M. G., Chaves, R. S. ; Diniz, P. S. R. ; Martins, W. A., "Doppler effects on transceivers with reduced redundancy," *2015 IEEE International Conference on Digital Signal Processing (DSP)*, Singapore, July 2015.

A.3 Technical Report

[T1] Diniz, P. S. R. ; Costa, F. M. ; Campos, M. L. R. ; Martins, W. A. ; Gussen, C. M. G.; Gois, J. N., "Technical Report on Subsea Communications," *GE Technical Report*, December 2013.

Appendix B

Example of Doppler Effect in Distinct Transmission Media

In order to investigate the inherent Doppler effect in two distinct transmission media, we analyze situations in which the Doppler frequency may have a high value. Typically, in RF communications over the air, the carrier frequency is on the order of Giga Hertz. Considering the 3G-LTE system (Third-Generation Long Term Evolution) as an example, the carrier frequency is around 2500 MHz in South America. Suppose that a person traveling in a high speed train, whose velocity is $v = 500$ km/h, wants to establish a communication. In order for the communication to be set, this system will have to deal with a Doppler effect of $f_{\mathrm{D}} = 2.5 \cdot 10^9 \cdot \frac{500 \cdot 10^3}{3600 \cdot 3 \cdot 10^8} \approx 1.157 \cdot 10^3$ Hz. This number corresponds to a deviation of $\frac{f_{\mathrm{D}}}{f_{\mathrm{c}}} = 4.6 \cdot 10^{-5}\%$ around the signal-carrier frequency. Notice that the designated bandwidth for this system is of the order of Mega Hertz, and the subcarrier spacing is 15 kHz.

In the case of underwater acoustic transmission, the carrier frequency is also called central frequency due to its low value. The central frequency is of the order of kilo Hertz, and generally is situated from 5 kHz up to 100 kHz. The low value of the central frequency is related to the fact that an acoustic wave of high frequency faces high attenuation, compromising the signal propagation distance. In a theoretical case, where two vessels are moving with a relative velocity of 40 m/s, the resulting Doppler frequency varies from $f_{\mathrm{D}} \approx 5 \cdot 10^3 \frac{40}{1500} \approx 133$ Hz up to $f_{\mathrm{D}} = 100 \cdot 10^3 \frac{40}{1500} \approx 2667$ Hz. This signal frequency disturbance corresponds to a deviation of $\frac{f_{\mathrm{D}}}{f_{\mathrm{c}}} \approx 2.66\%$ around the central frequency. Notice that this percentage is 578% higher than the case for RF communications. The last percentage value illustrates a reason why the Doppler effect is considered to be more severe in underwater acoustic environments.

Figure B.1 illustrates the Doppler frequency for distinct relative movements for $c = 1500$ m/s. As can be observed, the use of higher central frequency leads to higher Doppler frequency, and for all values of central frequency, the signal suffers a deviation of $\frac{f_{\mathrm{D}}}{f_{\mathrm{c}}} \approx 2.66\%$ for $v = 40$ m/s. Therefore, for achieving a reliable

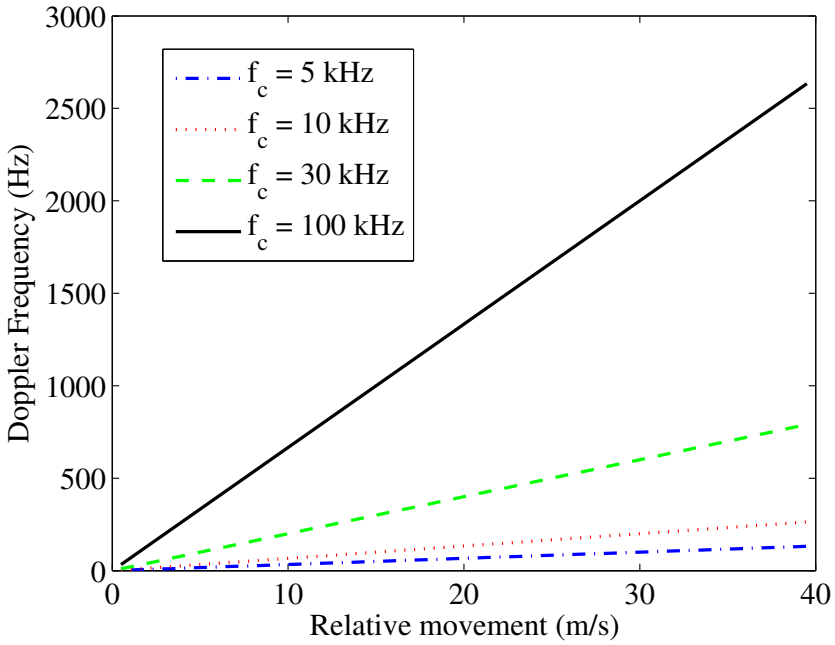

Figure B.1: Doppler frequency as a function of the relative movement considering an underwater acoustics environment.

communication, an efficient estimation and compensation of the Doppler frequency is mandatory.

Appendix C

Initial Case Study: Doppler Effects in RF Environment

In order to analyze the accuracy requirement of the Doppler estimator, we investigate the performance of transceivers with distinct redundancy lengths embedded in an environment subject to Doppler effects. We consider that the estimation of this effect was not properly performed, or in other words, that even after the Doppler effect compensation, a phase distortion remained in the signal.

C.1 Doppler Effects on Transceivers with Distinct Redundancy Lengths

To illustrate the importance of a good estimation process for the Doppler effect, we address the performance of transceivers with reduced redundancy operating in an RF environment. The motivation for this study [12] lies on the fact that these transceivers require a reduced amount of overhead data, possibly leading to systems with higher data throughput.

The received signal considering the Doppler effect, described in Eq. (3.18), is repeated here for convenience,

$$r(t) = \sum_{l=0}^{L} h_l(t)x(t-\tau_l(t))\mathrm{e}^{-\mathrm{j}2\pi f_\mathrm{c}\tau_l(t)} + \eta_\mathrm{PB}(t)\mathrm{e}^{-\mathrm{j}2\pi f_\mathrm{c}t}. \tag{C.1}$$

If we approximate the time delay within one block using Eq. (3.12), and consider that all channel paths are affected by the same Doppler factor: $a_1^{(l)} = a, \forall l$, Eq. (C.1)

can be rewritten as

$$\begin{aligned} r(t) &= \sum_{l=0}^{L} h_l(t)x((1+a_1^{(l)})t - a_0^{(l)})\mathrm{e}^{-\mathrm{j}2\pi f_c a_0^{(l)}}\mathrm{e}^{\mathrm{j}2\pi f_c a_1^{(l)} t} + \eta_{\mathrm{PB}}(t)\mathrm{e}^{-\mathrm{j}2\pi f_c t} \\ &= \sum_{l=0}^{L} h_l(t)x((1+a)t - a_0^{(l)})\mathrm{e}^{-\mathrm{j}2\pi f_c a_0^{(l)}}\mathrm{e}^{\mathrm{j}2\pi f_c a t} + \eta_{\mathrm{PB}}(t)\mathrm{e}^{-\mathrm{j}2\pi f_c t}. \end{aligned} \tag{C.2}$$

Assuming that an estimate of the Doppler factor $a \approx \hat{a}$ is available, a phase correction can be performed as:

$$\begin{aligned} y(t) &= r(t)\mathrm{e}^{-\mathrm{j}2\pi f_c \hat{a} t} \\ &= \sum_{l=0}^{L} h_l(t)x((1+a)t - a_0^{(l)})\mathrm{e}^{-\mathrm{j}2\pi f_c a_0^{(l)}} + \eta(t) \end{aligned} \tag{C.3}$$

where in the second equality we assumed that $(a - \hat{a}) \approx 0$, and $\eta(t) = \eta_{\mathrm{PB}}(t)\mathrm{e}^{-\mathrm{j}2\pi f_c t}\mathrm{e}^{-\mathrm{j}2\pi f_c \hat{a} t}$.

Considering that the pulse shaping is rectangular, that is, the value of $x(t)$ is constant during the symbol period T, the received signal described in Eq. (C.3) can be rewritten as:

$$y(t) = \sum_{l=0}^{L} h_l(t)x((1+a)t - lT)\mathrm{e}^{-\mathrm{j}2\pi f_c a_0^{(l)}} + \eta(t) \tag{C.4}$$

where the equality $a_0^{(l)} = lT$ holds only for the symbol index $x(\cdot)$ due to the rectangular pulse shaping assumption.

By resampling the signal at $t_n = \frac{nT}{(1+\hat{a})}$, we get:

$$y\left(\frac{nT}{(1+\hat{a})}\right) = \sum_{l=0}^{L} h_l\left(\frac{nT}{(1+\hat{a})}\right) x(nT - lT)\mathrm{e}^{-\mathrm{j}2\pi f_c a_0^{(l)}} + \eta\left(\frac{nT}{(1+\hat{a})}\right). \tag{C.5}$$

Knowing that $\breve{n} = \frac{nT}{(1+\hat{a})}$ represents the index of the received signal, and omitting the variable T, Eq. (C.5) can be rewritten as

$$y(\breve{n}) = \sum_{l=0}^{L} h_l(\breve{n})x(n-l)\mathrm{e}^{-\mathrm{j}2\pi f_c a_0^{(l)}} + \eta(\breve{n}). \tag{C.6}$$

Notice that the residual phase rotation is constant and depends only on the channel path, and assuming that the channel is essentially constant during the entire transmission: $h_l(\breve{n}) = h_l$. In the zero padding case, we can write the received signal of

Eq. (C.6) in a vector form, whereas the i-th block is described as

$$\boldsymbol{y}_i = \boldsymbol{H}_{\text{ISI}}\boldsymbol{T}_{\text{ZP}}\bar{\boldsymbol{F}}\ \boldsymbol{s}_i + \boldsymbol{H}_{\text{IBI}}\boldsymbol{T}_{\text{ZP}}\bar{\boldsymbol{F}}\ \boldsymbol{s}_{i-1} + \boldsymbol{\eta}_i, \tag{C.7}$$

where $\boldsymbol{H}_{\text{ISI}} \in \mathbb{C}^{(M+K)\times(M+K)}$ contains part of the channel that causes the intersymbol interference (ISI) within the same block, and is a Toeplitz matrix given by

$$\boldsymbol{H}_{\text{ISI}} = \begin{bmatrix} h_0 e^{-j2\pi f_c a_0^{(0)}} & 0 & 0 & \cdots & 0 \\ h_1 e^{-j2\pi f_c a_0^{(1)}} & h_0 e^{-j2\pi f_c a_0^{(0)}} & 0 & & \\ \vdots & \vdots & \ddots & & \\ h_L e^{-j2\pi f_c a_0^{(L)}} & h_{L-1} e^{-j2\pi f_c a_0^{(L-1)}} & \ddots & \ddots & \vdots \\ 0 & h_L e^{-j2\pi f_c a_0^{(L)}} & & \ddots & \\ \vdots & \ddots & \ddots & & 0 \\ 0 & \cdots & 0 & h_L e^{-j2\pi f_c a_0^{(L)}} \ \cdots & h_0 e^{-j2\pi f_c a_0^{(0)}} \end{bmatrix}.$$

The matrix $\boldsymbol{H}_{\text{IBI}} \in \mathbb{C}^{(M+K)\times(M+K)}$ contains part of the channel that causes interblock interference (IBI) and is a Toeplitz matrix given by

$$\boldsymbol{H}_{\text{IBI}} = \begin{bmatrix} 0 & \cdots & 0 & h_L e^{-j2\pi f_c a_0^{(L)}} & \cdots & h_2 e^{-j2\pi f_c a_0^{(2)}} & h_1 e^{-j2\pi f_c a_0^{(1)}} \\ & & & 0 & h_L e^{-j2\pi f_c a_0^{(L)}} & \cdots & h_2 e^{-j2\pi f_c a_0^{(2)}} \\ & & & & & \ddots & \vdots \\ \vdots & & & & \ddots & & h_L e^{-j2\pi f_c a_0^{(L)}} \\ & & & & & & 0 \\ 0 & & & \cdots & & & 0 \end{bmatrix}.$$

At the receiver end, a linear transformation is applied to the received signal

$$\hat{\boldsymbol{s}}_i = \boldsymbol{G}\boldsymbol{H}_{\text{ISI}}\boldsymbol{T}_{\text{ZP}}\bar{\boldsymbol{F}}\ \boldsymbol{s}_i + \boldsymbol{G}\boldsymbol{H}_{\text{IBI}}\boldsymbol{T}_{\text{ZP}}\bar{\boldsymbol{F}}\ \boldsymbol{s}_{i-1} + \boldsymbol{G}\boldsymbol{\eta}_i, \tag{C.8}$$

where

$$\boldsymbol{G} = \begin{bmatrix} \boldsymbol{0}_{M\times(L-K)} & \overline{\boldsymbol{G}} \end{bmatrix}, \tag{C.9}$$

and $\overline{\boldsymbol{G}} \in \mathbb{C}^{M\times(M+2K-L)}$ is the receiver matrix. Eq. (C.8) can be rewritten as

$$\hat{\boldsymbol{s}}_i = \bar{\boldsymbol{G}}\bar{\boldsymbol{H}}\bar{\boldsymbol{F}}\ \boldsymbol{s}_i + \boldsymbol{G}\boldsymbol{\eta}_i. \tag{C.10}$$

Notice that the IBI was eliminated due to the procedure of inserting and removing the zeros, and the matrix $\bar{\boldsymbol{H}}$ is given by Eq. (C.11) considering the zero padding

case:

$$\bar{\boldsymbol{H}} = \begin{bmatrix} h_{L-K}\mathrm{e}^{-\mathrm{j}2\pi f_c a_0^{(L-K)}} & \cdots & h_0\mathrm{e}^{-\mathrm{j}2\pi f_c a_0^{(0)}} & 0 & 0 & \cdots & 0 \\ \vdots & \ddots & & & & & \vdots \\ h_K\mathrm{e}^{-\mathrm{j}2\pi f_c a_0^{(K)}} & \ddots & & & & & 0 \\ \vdots & \ddots & & & & \ddots & h_0\mathrm{e}^{-\mathrm{j}2\pi f_c a_0^{(0)}} \\ h_L\mathrm{e}^{-\mathrm{j}2\pi f_c a_0^{(L)}} & & & & & & \vdots \\ 0 & & & & & \ddots & h_{L-K}\mathrm{e}^{-\mathrm{j}2\pi f_c a_0^{(L-K)}} \\ \vdots & & & & & & \vdots \\ 0 & \cdots & 0 & 0 & h_L\mathrm{e}^{-\mathrm{j}2\pi f_c a_0^{(L)}} & \cdots & h_K\mathrm{e}^{-\mathrm{j}2\pi f_c a_0^{(K)}} \end{bmatrix}. \quad \text{(C.11)}$$

The objective of the receiver matrix is to minimize the mean square error (MSE) of the received signal. A receiver matrix that minimizes the MSE for the multicarrier case is given by [81]:

$$\bar{\boldsymbol{G}}_{\mathrm{MMSE}} = \boldsymbol{F}^H \left(\bar{\boldsymbol{H}}^H \bar{\boldsymbol{H}} + \frac{1}{\mathrm{SNR}} \boldsymbol{I}_M \right)^{-1} \bar{\boldsymbol{H}}^H, \quad \text{(C.12)}$$

where SNR is the signal-to-noise ratio. This receiver matrix is designed for a system with reduced redundancy K, with $\lceil L/2 \rceil \leq K < L$. Despite the low redundancy, the implementation of Eq. (C.12) requires $\mathcal{O}(M^3)$ complex valued operations, while zero-prefix OFDM transceivers require only $\mathcal{O}(M \log_2 M)$ complex-valued operations. In [86] it is proposed an efficient design for this receiver matrix, which employs only $\mathcal{O}(M \log_2 M)$ complex-valued operations.

Notice that the receiver matrix $\bar{\boldsymbol{G}}_{\mathrm{MMSE}}$ is a function of the channel estimate $\bar{\boldsymbol{H}}$. The channel impulse response can be estimated using a least-squares solution for the case the transceiver has minimum redundancy. Thus, considering $\lceil L/2 \rceil$ redundancy, the coefficients of the matrix $\bar{\boldsymbol{H}}$ can be estimated as [82]

$$\hat{\boldsymbol{h}} = \left(\bar{\boldsymbol{S}}^H \bar{\boldsymbol{S}} + \frac{1}{\mathrm{SNR}} \boldsymbol{I}_{L+1} \right)^{-1} \bar{\boldsymbol{S}}^H \boldsymbol{y} \quad \text{(C.13)}$$

where $\bar{\boldsymbol{S}}$ is a Toeplitz matrix of the transmitted pilot symbols, whose first row is $[\bar{s}(L/2) \cdots \bar{s}(0) \ \mathbf{0}_{1\times L/2}]$, and the first column is $[\bar{s}(L/2) \cdots \bar{s}(M-1) \ \mathbf{0}_{1\times L/2}]^T$. Notice that we are assuming that the first transmitted block was composed only of pilot symbols. Another algorithm for implementing Eq. (C.13) was proposed in [82]. This algorithm employs efficient matrix decompositions in order to reduce the computational complexity required by Eq. (C.13).

C.1.1 Simulation Results

Simulations were performed in order to compare the performance of transceivers with reduced redundancy described in Subsection C.1 with the standard transceivers employing full redundancy, in an environment that induces a Doppler spread. We considered both single-carrier and multicarrier systems.

Only the implemented single-carrier (SC) system performs the equalization in the frequency domain (SC-FD), while the SC with reduced and minimum redundancy systems perform the equalization in the time domain. For both single-carrier and multicarrier systems, zeros are inserted as redundancy, and the redundancy length varies between the minimum case ($K = \lceil \frac{L}{2} \rceil$) and the full case ($K = L$).

The channel fading model follows a Rayleigh distribution on each path[1], and the channel impulse response has length $L = 16$. The channel coefficients were normalized, and new channel coefficients were generated in each simulation. We ran 200 simulations for each system configuration.

Firstly, our objective is to analyze the system performance when the Doppler effect is estimated imprecisely. For this purpose, we ran simulations for single-carrier and multicarrier systems with distinct redundancy values: $K = 15$, $K = 11$, and $K = 8$. The Doppler effect was considered to be the same for all the multiple paths. The value of the Doppler effect was $f_{\mathrm{D}} \in \{20, 50, 100, 200\}$ Hz, which are equivalent to relative movements between transmitter and receiver of $v \in \{6, 15, 30, 60\}$ m/s, respectively, considering that the carrier frequency is at $f_{\mathrm{c}} = 1 \times 10^9$ Hz, and that the wave speed of propagation is $c = 3 \times 10^8$ m/s. We considered that the estimated Doppler frequency (f_{D}) had an error between $0 - 10\%$, i.e., we had the perfect knowledge of the parameter a, and we added a fixed error when compensating this factor. The channel was estimated using a least-squares estimator, e.g., Eq. (C.13). In each simulation 200 blocks were transmitted, each block had a length of $M = 256$, and each block had a duration of 64 μ s. Figures C.1 and C.2 show the bit-error rate (BER) as a function of the estimation error for single-carrier and multicarrier systems, respectively, for an SNR = 20 dB. As observed in both Figures C.1 and C.2, higher error in Doppler estimation leads to worse system performance. Besides, for errors near 10% for $f_{\mathrm{D}} = 200$ Hz, all the systems seem to have the same poor performance.

Besides, we calculated the mean squared error in order to understand why the initial performance shown in Figure C.2 of reduced redundancy system was better than minimum and full redundancy, respectively. We measured the mean squared error between the received signal embedded in noise and an auxiliary signal without

[1]Each channel coefficient is a complex Gaussian random variable.

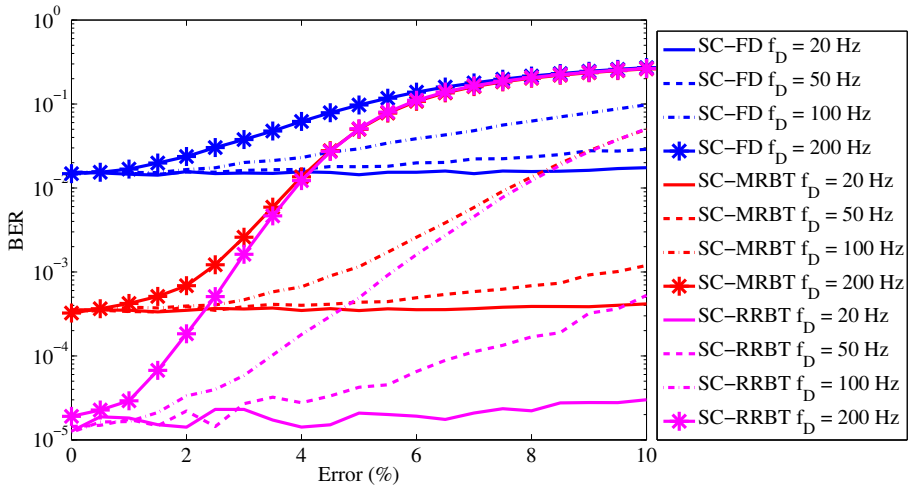

Figure C.1: BER versus Doppler estimation error for SC systems: SC-FDE ($K = 15$), SC-MRBT stands for single-carrier with minimum redundancy block transceiver ($K = 8$), and SC-RRBT stands for single-carrier with reduced redundancy block transceiver ($K = 11$).

noise (denoted by $\check{\boldsymbol{s}}_i$) as follows:

$$\|\hat{\boldsymbol{s}}_i - \check{\boldsymbol{s}}_i\|^2 = \|\bar{\boldsymbol{G}}\bar{\boldsymbol{H}}\bar{\boldsymbol{F}}\ \boldsymbol{s}_i + \boldsymbol{G}\boldsymbol{\eta}_i - \bar{\boldsymbol{G}}\bar{\boldsymbol{H}}\bar{\boldsymbol{F}}\ \boldsymbol{s}_i\|^2 = \|\boldsymbol{G}\boldsymbol{\eta}_i\|^2. \tag{C.14}$$

The obtained values are on Table C.1. These measurements are in agreement with observed performance of the transceivers at low Doppler error.

Table C.1: MSE of Eq. (C.14)

Redundancy	MSE
Minimum ($K = 8$)	0.0582
Reduced ($K = 11$)	0.0563
Full ($K = 15$)	0.0599

In order to observe the behavior of the bit-error rate (BER) as a function of the SNR, we chose a Doppler frequency of $f_{\mathrm{D}} = 200$ Hz. Figures C.3 and C.4 show the BER as a function of the SNR for single-carrier and multicarrier systems, respectively, when the Doppler was estimated with an error of 3%. In Figures C.5 and C.6, we considered that the estimated Doppler frequency had an error that follows a uniform distribution: $-5\text{ Hz} < \epsilon_{f_{\mathrm{D}}} < 5\text{ Hz}$. For all cases, no channel coding was performed. We observe that when Doppler effect is not compensated, the BER increases, what can hinder a reliable communication. On the other hand, when this effect is compensated, all the systems reach a performance near the ones obtained by the scenarios that are not affected by Doppler shift. Since the reduced redundancy systems achieved a lower BER than the full redundancy systems in this setup, then the throughput might be higher for these reduced redundancy transceivers.

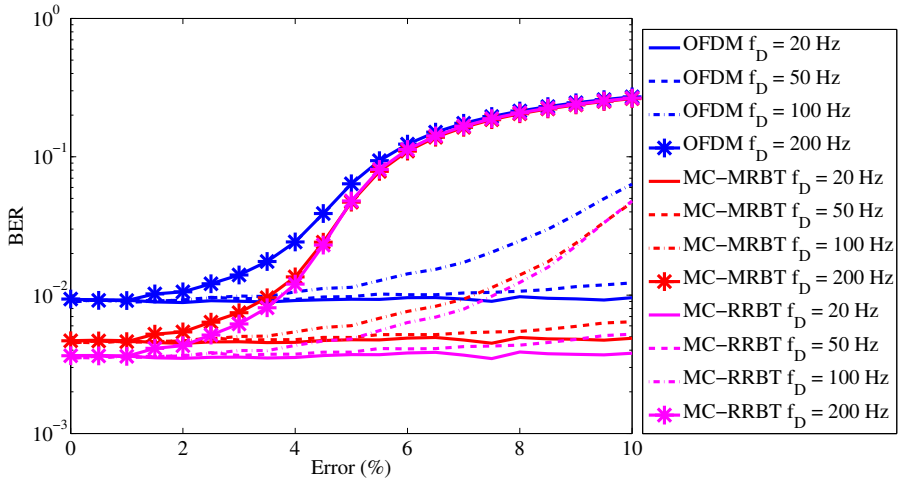

Figure C.2: BER versus Doppler estimation error for multicarrier systems: OFDM ($K = 15$), MC-MRBT stands for multicarrier with minimum redundancy block transceiver ($K = 8$), and MC-RRBT stands for multicarrier with reduced redundancy block transceiver ($K = 11$).

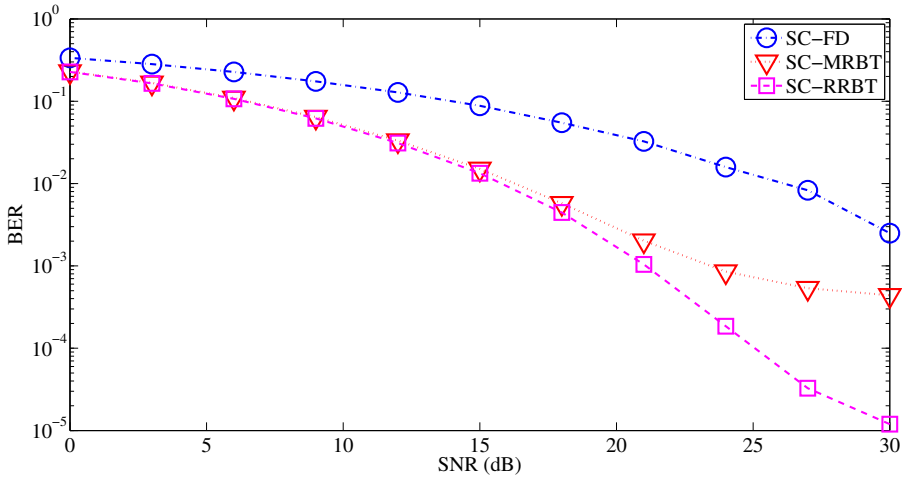

Figure C.3: BER versus SNR for SC systems with 3% error in Doppler estimation: SC-FDE ($K = 15$), SC-MRBT stands for single-carrier with minimum redundancy block transceiver ($K = 8$), and SC-RRBT stands for single-carrier with reduced redundancy block transceiver ($K = 11$).

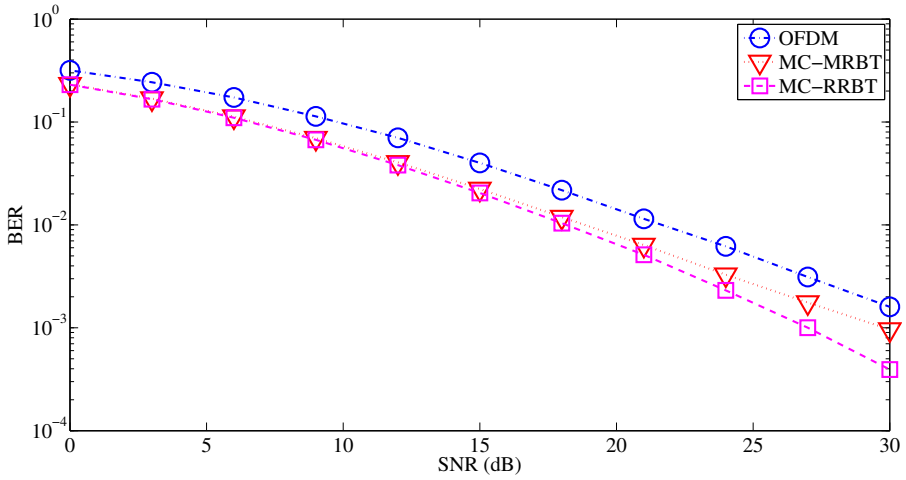

Figure C.4: BER versus SNR for multicarrier systems with 3% error in Doppler estimation: OFDM ($K = 15$), MC-MRBT stands for multicarrier with minimum redundancy block transceiver ($K = 8$), and MC-RRBT stands for multicarrier with reduced redundancy block transceiver ($K = 11$).

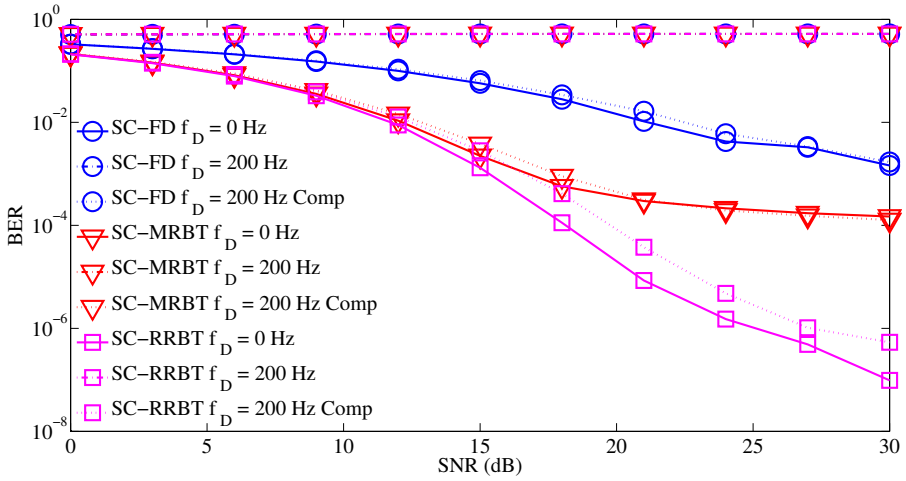

Figure C.5: BER versus SNR for SC systems with random error in Doppler estimation: SC-FDE ($K = 15$), SC-MRBT stands for single-carrier with minimum redundancy block transceiver ($K = 8$), and SC-RRBT stands for single-carrier with reduced redundancy block transceiver ($K = 11$).

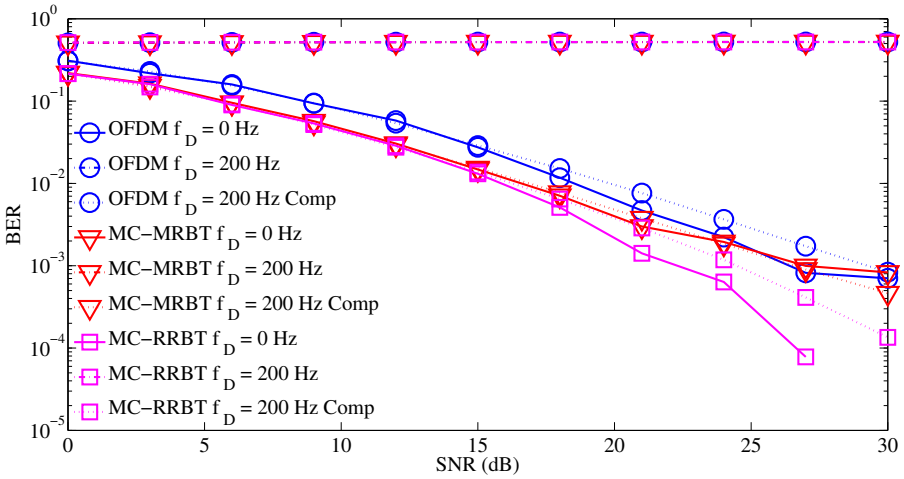

Figure C.6: BER versus SNR for multicarrier systems with random error in Doppler estimation: OFDM ($K = 15$), MC-MRBT stands for multicarrier with minimum redundancy block transceiver ($K = 8$), and MC-RRBT stands for multicarrier with reduced redundancy block transceiver ($K = 11$).

C.2 Summary

In order to investigate the robustness of the transceivers with reduced redundancy with respect to Doppler effect, we analyzed the performance of these transceivers considering that this effect was not properly estimated and compensated[2]. The conclusion is that the communication might be compromised in case this effect is not accurately estimated and mitigated.

[2]In RF communications over the air.

Appendix D

Algorithm Tracking Analysis Constraints

This appendix contains a brief analysis of the algorithm tracking constraints presented in Subsection 4.3.1.

As the symbol period can be described as

$$T = T_h \cdot p \tag{D.1}$$

where T_h is the sampling period, and p is a parameter representing the number of samples of one symbol, the system bandwidth is given by

$$B = 2F_h/p = \frac{2}{T_h \cdot p} = \frac{2}{T}. \tag{D.2}$$

Knowing that the carrier frequency must assume a value at least twice than the system bandwidth:

$$f_c - B/2 > 0, \tag{D.3}$$

Eq. (D.2) can be rewritten as

$$\frac{1}{f_c} < T, \tag{D.4}$$

resulting in

$$\frac{1}{8 \cdot f_c} < \frac{1}{2 \cdot f_c} < \frac{T}{2}. \tag{D.5}$$

Considering the single-carrier system with a QPSK constellation described in Subsection 4.3.1, whose error boundary with respect to the signal phase was de-

scribed as

$$\begin{aligned} \theta - \frac{\pi}{4} &< 2\pi f_c \epsilon_n + \theta < \theta + \frac{\pi}{4}, \\ \frac{-1}{8f_c} &< \epsilon_n < \frac{1}{8f_c}, \end{aligned} \tag{D.6}$$

and the error with respect to the sampling instant as:

$$\begin{aligned} (2n-1)T/2 &< nT + \epsilon_n < (2n+1)T/2 \\ \frac{-T}{2} &< \epsilon_n < \frac{T}{2}, \end{aligned} \tag{D.7}$$

one can observe the phase constraint always prevails over the time-shift constraint.

Proof. If Eq. (D.6) is satisfied then Eq. (D.7) is also satisfied:

$$\frac{-T}{2} < \frac{-1}{8f_c} < \epsilon_n < \frac{1}{8f_c} < \frac{T}{2}. \tag{D.8}$$

□

Bibliography

[1] GABRIEL, C., KHALIGHI, M. A., BOURENNANE, S., et al. "Monte-Carlo-Based Channel Characterization for Underwater Optical Communication Systems", *J. Opt. Commun. Netw.*, v. 5, n. 1, pp. 1–12, January 2013. doi: 10.1364/JOCN.5.000001.

[2] COCHENOUR, B. M., MULLEN, L. J., LAUX, A. E. "Characterization of the Beam-Spread Function for Underwater Wireless Optical Communications Links", *Oceanic Engineering, IEEE Journal of*, v. 33, n. 4, pp. 513–521, 2008. ISSN: 0364-9059. doi: 10.1109/JOE.2008.2005341.

[3] LANZAGORTA, M. *Underwater Communication*, v. 5, *Synthesis Lectures on Communications*. Morgan & Claypool Publishers, 2012. doi: 10.2200/S00409ED1V01Y201203COM006.

[4] GUSSEN, C. M. G., DINIZ, P. S. R., CAMPOS, M. L. R., et al. "A Survey of Underwater Wireless Communication Technologies", *Journal of Communication and Information Systems*, v. 31, n. 1, pp. 242–255, 2016.

[5] CHITRE, M., SHAHABUDEEN, S., STOJANOVIC, M. "Underwater Acoustic Communications and Networking: Recent Advances and Future Challenges", *Marine Technology Society Journal*, v. 42, n. 1, pp. 103–116, 2008. doi: https://doi.org/10.4031/002533208786861263.

[6] MELODIA, T., KULHANDJIAN, H., KUO, L.-C., et al. "Advances in Underwater Acoustic Networking". In: *Mobile Ad Hoc Networking*, first ed., cap. 23, pp. 804–852, John Wiley & Sons, Inc., 2012. doi: 10.1002/9781118511305.ch23.

[7] PALMEIRO, A., MARTIN, M., CROWTHER, I., et al. "Underwater Radio Frequency Communications". In: *OCEANS, 2011 IEEE - Spain*, pp. 1–8, 2011. doi: 10.1109/Oceans-Spain.2011.6003580.

[8] CHE, X., WELLS, I., DICKERS, G., et al. "Re-Evaluation of RF Electromagnetic Communication in Underwater Sensor Networks", *Communications*

Magazine, IEEE, v. 48, n. 12, pp. 143–151, 2010. ISSN: 0163-6804. doi: 10.1109/MCOM.2010.5673085.

[9] SIMPSON, J. A., HUGHES, B. L., MUTH, J. F. "Smart Transmitters and Receivers for Underwater Free-Space Optical Communication", *Selected Areas in Communications, IEEE Journal on*, v. 30, n. 5, pp. 964–974, June 2012. ISSN: 0733-8716. doi: 10.1109/JSAC.2012.120611.

[10] DINIZ, P. S. R., COSTA, F. M., CAMPOS, M. L. R. D., et al. *Subsea Communications*. Relatório técnico, GE Global Research, 2013.

[11] GUSSEN, C. M. G., CAMPOS, M. L. R., DINIZ, P. S. R., et al. "On the channel frequency response in shallow seawater". In: *International Conference & Exhibition on Underwater Acoustics*, pp. 387–392, June 2015.

[12] GUSSEN, C. M. G., CHAVES, R. S., DINIZ, P. S. R., et al. "Doppler effects on transceivers with reduced redundancy". In: *Digital Signal Processing (DSP), 2015 IEEE International Conference on*, pp. 388–392, July 2015. doi: 10.1109/ICDSP.2015.7251899.

[13] MOORE, R. "Radio communication in the sea", *Spectrum, IEEE*, v. 4, n. 11, pp. 42–51, 1967. ISSN: 0018-9235. doi: 10.1109/MSPEC.1967.5217169.

[14] ROWE, H. E. "Extremely Low Frequency (ELF) Communication to Submarines", *Communications, IEEE Transactions on*, v. 22, n. 4, pp. 371–385, 1974. ISSN: 0090-6778. doi: 10.1109/TCOM.1974.1092211.

[15] CHEN, Y., YAN PAN, W., YUN PENG, H., et al. "The ELF/VLF field at the depth of submarine excited by satellite electropult". In: *Antennas Propagation and EM Theory (ISAPE), 2010 9th International Symposium on*, pp. 505–508, 2010. doi: 10.1109/ISAPE.2010.5696513.

[16] DOWDEN, R., HOLZWORTH, R., RODGER, C., et al. "World-wide lightning location using VLF propagation in the Earth-ionosphere waveguide", *Antennas and Propagation Magazine, IEEE*, v. 50, n. 5, pp. 40–60, 2008. ISSN: 1045-9243. doi: 10.1109/MAP.2008.4674710.

[17] SEXTON, D. *Subsea Communications, RPSEA Final Report*. Relatório técnico, GE Global Research, December 2011.

[18] HANSON, F., RADIC, S. "High Bandwidth Underwater Optical Communication", *J. Opt. Commun. Netw.*, v. 47, n. 2, pp. 277–283, January 2008.

[19] SIMPSON, J. *A 1 Mbps Underwater Communications System using LEDs and Photodiodes with Signal Processing Capability*. Tese de Mestrado, North Carolina State University, Raleigh, North Carolina, USA, 2007.

[20] HALTRIN, V. I. "Chlorophyll-Based Model of Seawater Optical Properties", *Applied Optics*, v. 38, pp. 6826–6832, 1999.

[21] ARNON, S. "An underwater optical wireless communication network". In: *Proc. SPIE 7464, Free-Space Laser Communications IX*, 2010.

[22] JARUWATANADILOK, S. "Underwater Wireless Optical Communication Channel Modeling and Performance Evaluation using Vector Radiative Transfer Theory", *Selected Areas in Communications, IEEE Journal on*, v. 26, n. 9, pp. 1620–1627, 2008. ISSN: 0733-8716. doi: 10.1109/JSAC.2008.081202.

[23] BRUNDAGE, H. *Designing a Wireless Underwater Optical Communication System*. Tese de Mestrado, Massachusetts Institute of Technology, Cambridge, MA, USA, 2010.

[24] JENSEN, F. B., KUPERMAN, W. A., PORTER, M. B., et al. *Computational Ocean Acoustics*. Modern Acoustics and Signal Processing. 2 ed. , Springer Publishers, 2011.

[25] STOJANOVIC, M. "Recent advances in high-speed underwater acoustic communications", *IEEE Journal of Oceanic Engineering*, v. 21, n. 2, pp. 125–136, Apr 1996. ISSN: 0364-9059. doi: 10.1109/48.486787.

[26] KILFOYLE, D. B., BAGGEROER, A. B. "The state of the art in underwater acoustic telemetry", *IEEE Journal of Oceanic Engineering*, v. 25, n. 1, pp. 4–27, Jan 2000. ISSN: 0364-9059. doi: 10.1109/48.820733.

[27] P. QARABAQI, M. S. "Statistical modeling of a shallow water acoustic communication channel". In: *Proc. Underwater Acoust. Meas. Conf.*, pp. 1341–1350, Nafplion, Greece, June 2009.

[28] QARABAQI, P., STOJANOVIC, M. "Statistical Characterization and Computationally Efficient Modeling of a Class of Underwater Acoustic Communication Channels", *Oceanic Engineering, IEEE Journal of*, v. 38, n. 4, pp. 701–717, Oct 2013. ISSN: 0364-9059. doi: 10.1109/JOE.2013.2278787.

[29] CHITRE, M. "A high-frequency warm shallow water acoustic communications channel model and measurements", *J. Acoust. Soc. Amer.*, v. 122, n. 5, pp. 2580–2586, 2007.

[30] PASSERIEUX, J. M., SOCHELEAU, F. X., LAOT, C. "On the Capacity of the Underwater Acoustic Communication Channel under Realistic Assumptions". In: *Wireless Conference 2011 - Sustainable Wireless Technologies (European Wireless), 11th European*, pp. 1–6, April 2011.

[31] PASSERIEUX, J. M., SOCHELEAU, F. X., LAOT, C. "Achievable Rates over Doubly Selective Rician-Fading Channels under Peak-Power Constraint", *IEEE Transactions on Wireless Communications*, v. 12, n. 2, pp. 586–594, February 2013. ISSN: 1536-1276. doi: 10.1109/TWC.2012.122212.111812.

[32] PREISIG, J. "Acoustic Propagation Considerations for Underwater Acoustic Communications Network Development", *SIGMOBILE Mobile Computing and Communications Review*, v. 11, n. 4, pp. 2–10, October 2007. ISSN: 1559-1662. doi: 10.1145/1347364.1347370.

[33] BAGGEROER, A. B. "An overview of acoustic communications from 2000-2012". In: *Underwater Communications: Channel Modelling & Validation (UComms)*, Sestri Levante, Italy, September 2012. NATO Centre for Maritime Research and Experimentation.

[34] CHOI, J. W., RIEDL, T. J., KIM, K., et al. "Adaptive Linear Turbo Equalization Over Doubly Selective Channels", *Oceanic Engineering, IEEE Journal of*, v. 36, n. 4, pp. 473–489, 2011. ISSN: 0364-9059. doi: 10.1109/JOE.2011.2158013.

[35] SONG, H. C. "An Overview of Underwater Time-Reversal Communication", *IEEE Journal of Oceanic Engineering*, v. PP, n. 99, pp. 1–12, 2015. ISSN: 0364-9059. doi: 10.1109/JOE.2015.2461712.

[36] FINK, M. "Time-Reversed Acoustics", *Scientific American*, pp. 91–97, November 1999.

[37] VAN WALREE, P. "Propagation effects in underwater acoustic communication channels". In: *Underwater Communications: Channel Modelling & Validation (UComms)*, Sestri Levante, Italy, September 2012. NATO Centre for Maritime Research and Experimentation.

[38] ETTER, P. C. *Underwater Acoustic Modeling and Simulation*. Third edition ed. , Spon Press, 2003.

[39] STOJANOVIC, M. "On the Relationship Between Capacity and Distance in an Underwater Acoustic Communication Channel", *SIGMOBILE Mobile Computing and Communications Review*, v. 11, n. 4, pp. 34–43, October 2007. ISSN: 1559-1662. doi: 10.1145/1347364.1347373.

[40] BREKHOVSKIKH, L. M., LYSANOV, Y. P. *Fundamentals of Ocean Acoustics*. 3 ed. , Springer Publishers, 2003.

[41] STOJANOVIC, M., PREISIG, J. "Underwater acoustic communication channels: Propagation models and statistical characterization", *Communications Magazine, IEEE*, v. 47, n. 1, pp. 84–89, January 2009. ISSN: 0163-6804. doi: 10.1109/MCOM.2009.4752682.

[42] DOMINGO, M. C. "Overview of Channel Models for Underwater Wireless Communication Networks ", *Physical Communication*, v. 1, n. 3, pp. 163–182, 2008. ISSN: 1874-4907. doi: http://dx.doi.org/10.1016/j.phycom.2008.09.001.

[43] RIEDL, T., BEAN, A., SINGER, A. "Broadband Doppler Compensation: Experimental Evaluation". In: *Underwater Communications: Channel Modelling & Validation (UComms)*, Sestri Levante, Italy, September 2012. NATO Centre for Maritime Research and Experimentation.

[44] RIEDL, T. J., SINGER, A. C. "Broadband Doppler Compensation: Principles and New Results". In: *Signals, Systems and Computers (ASILOMAR), 2011 Conference Record of the Forty Fifth Asilomar Conference on*, pp. 944–946, 2011. doi: 10.1109/ACSSC.2011.6190149.

[45] DIAMANT, R., FEUER, A., LAMPE, L. "Choosing the Right Signal: Doppler Shift Estimation for Underwater Acoustic Signals". In: *7th ACM International Conference on Underwater Networks & Systems*, Los Angeles, CA, USA, November 2012.

[46] PERRINE, K. A., NIEMAN, K. F., HENDERSON, T. L., et al. "Doppler estimation and correction for shallow underwater acoustic communications". In: *Signals, Systems and Computers (ASILOMAR), 2010 Conference Record of the Forty Fourth Asilomar Conference on*, pp. 746–750, 2010. doi: 10.1109/ACSSC.2010.5757663.

[47] RABASTE, O., CHONAVEL, T. "Estimation of Multipath Channels With Long Impulse Response at Low SNR via an MCMC Method", *Signal Processing, IEEE Transactions on*, v. 55, n. 4, pp. 1312–1325, 2007. ISSN: 1053-587X. doi: 10.1109/TSP.2006.888060.

[48] YUEN, C. H., FARHANG-BOROUJENY, B. "Doppler scaling correction in OFDM". In: *Communications (ICC), 2013 IEEE International Conference on*, pp. 4713–4717, June 2013. doi: 10.1109/ICC.2013.6655317.

[49] ABDELKAREEM, A. E., SHARIF, B. S., TSIMENIDIS, C. C., et al. "Low-complexity Doppler compensation for OFDM-based underwater acoustic communication systems". In: *OCEANS, 2011 IEEE - Spain*, pp. 1–6, June 2011. doi: 10.1109/Oceans-Spain.2011.6003384.

[50] KANG, T., ILTIS, R. A. "Fast-varying Doppler compensation for underwater acoustic OFDM systems". In: *Signals, Systems and Computers, 2008 42nd Asilomar Conference on*, pp. 933–937, October 2008. doi: 10.1109/ACSSC.2008.5074548.

[51] KIBANGOU, A. Y., ROS, L., SICLET, C. "Doppler estimation and data detection for underwater acoustic ZF-OFDM receiver". In: *Wireless Communication Systems (ISWCS), 2010 7th International Symposium on*, pp. 591–595, September 2010. doi: 10.1109/ISWCS.2010.5624286.

[52] LI, B., ZHOU, S., STOJANOVIC, M., et al. "Multicarrier Communication Over Underwater Acoustic Channels With Nonuniform Doppler Shifts", *Oceanic Engineering, IEEE Journal of*, v. 33, n. 2, pp. 198–209, April 2008. ISSN: 0364-9059. doi: 10.1109/JOE.2008.920471.

[53] MASON, S. F., BERGER, C. R., ZHOU, S., et al. "Detection, Synchronization, and Doppler Scale Estimation with Multicarrier Waveforms in Underwater Acoustic Communication", *Selected Areas in Communications, IEEE Journal on*, v. 26, n. 9, pp. 1638–1649, December 2008. ISSN: 0733-8716. doi: 10.1109/JSAC.2008.081204.

[54] TRUBUIL, J., CHONAVEL, T. "Accurate Doppler estimation for underwater acoustic communications". In: *OCEANS, 2012 - Yeosu*, pp. 1–5, May 2012. doi: 10.1109/OCEANS-Yeosu.2012.6263500.

[55] TU, K., DUMAN, T. M., STOJANOVIC, M., et al. "Multiple-Resampling Receiver Design for OFDM Over Doppler-Distorted Underwater Acoustic Channels", *Oceanic Engineering, IEEE Journal of*, v. 38, n. 2, pp. 333–346, April 2013. ISSN: 0364-9059. doi: 10.1109/JOE.2012.2221812.

[56] ZAKHAROV, Y. V., KODANEV, V. P. "Multipath-Doppler diversity of OFDM signals in an underwater acoustic channel". In: *Acoustics, Speech, and Signal Processing, 2000. ICASSP '00. Proceedings. 2000 IEEE International Conference on*, v. 5, pp. 2941–2944, 2000. doi: 10.1109/ICASSP.2000.861150.

[57] YUEN, C. H., FARHANG-BOROUJENY, B. "Non-linear Doppler scaling correction in underwater acoustic channels: Analysis and simulation". In: *Oceans - San Diego, 2013*, pp. 1–7, Sept 2013.

[58] LI, W., PREISIG, J. C. "Estimation of Rapidly Time-Varying Sparse Channels", *IEEE Journal of Oceanic Engineering*, v. 32, n. 4, pp. 927–939, Oct 2007. doi: 10.1109/JOE.2007.906409.

[59] STOJANOVIC, M. "OFDM for underwater acoustic communications: Adaptive synchronization and sparse channel estimation". In: *2008 IEEE International Conference on Acoustics, Speech and Signal Processing*, pp. 5288–5291, March 2008. doi: 10.1109/ICASSP.2008.4518853.

[60] BERGER, C. R., ZHOU, S., PREISIG, J. C., et al. "Sparse Channel Estimation for Multicarrier Underwater Acoustic Communication: From Subspace Methods to Compressed Sensing", *IEEE Transactions on Signal Processing*, v. 58, n. 3, pp. 1708–1721, March 2010. doi: 10.1109/TSP.2009.2038424.

[61] KANG, T., ILTIS, R. A. "Iterative Carrier Frequency Offset and Channel Estimation for Underwater Acoustic OFDM Systems", *IEEE Journal on Selected Areas in Communications*, v. 26, n. 9, pp. 1650–1661, December 2008. doi: 10.1109/JSAC.2008.081205.

[62] PELEKANAKIS, K., CHITRE, M. "Adaptive Sparse Channel Estimation under Symmetric alpha-Stable Noise", *IEEE Transactions on Wireless Communications*, v. 13, n. 6, pp. 3183–3195, June 2014. doi: 10.1109/TWC.2014.042314.131432.

[63] LI, J., ZAKHAROV, Y. V. "Sliding window adaptive filter with diagonal loading for estimation of sparse UWA channels". In: *OCEANS 2016 - Shanghai*, pp. 1–5, April 2016. doi: 10.1109/OCEANSAP.2016.7485346.

[64] FINK, M. "Time Reversal of Ultrasonic Fields – Part I: Basic Principles", *Ultrasonics, Ferroelectrics and Frequency Control, IEEE Transactions on*, v. 39, n. 5, pp. 555–566, September 1992. ISSN: 0885-3010. doi: 10.1109/58.156174.

[65] TUCHLER, M., KOETTER, R., SINGER, A. C. "Turbo equalization: principles and new results", *IEEE Transactions on Communications*, v. 50, n. 5, pp. 754–767, May 2002. doi: 10.1109/TCOMM.2002.1006557.

[66] OTNES, R., TUCHLER, M. "Iterative channel estimation for turbo equalization of time-varying frequency-selective channels", *IEEE Transactions on Wireless Communications*, v. 3, n. 6, pp. 1918–1923, Nov 2004. doi: 10.1109/TWC.2004.837421.

[67] OTNES, R., EGGEN, T. H. "Underwater Acoustic Communications: Long-Term Test of Turbo Equalization in Shallow Water", *IEEE Journal of Oceanic Engineering*, v. 33, n. 3, pp. 321–334, July 2008. doi: 10.1109/JOE.2008.925893.

[68] FANG, K., RUGINI, L., LEUS, G. "Low-Complexity Block Turbo Equalization for OFDM Systems in Time-Varying Channels", *IEEE Transactions on Signal Processing*, v. 56, n. 11, pp. 5555–5566, Nov 2008. doi: 10.1109/TSP.2008.929129.

[69] FREITAG, L., GRUND, M., SINGH, S., et al. "A bidirectional coherent acoustic communication system for underwater vehicles". In: *OCEANS '98 Conference Proceedings*, v. 1, pp. 482–486, 1998. doi: 10.1109/OCEANS.1998.725794.

[70] KOJIMA, J., URA, T., ANDO, H., et al. "High-speed acoustic data link transmitting moving pictures for autonomous underwater vehicles". In: *Underwater Technology, 2002. Proceedings of the 2002 International Symposium on*, pp. 278–283, 2002. doi: 10.1109/UT.2002.1002439.

[71] PELEKANAKIS, C., STOJANOVIC, M., FREITAG, L. "High rate acoustic link for underwater video transmission". In: *OCEANS 2003. Proceedings*, v. 2, pp. 1091–1097, 2003. doi: 10.1109/OCEANS.2003.178494.

[72] OCHI, H., WATANABE, Y., SHIMURA, T., et al. "The acoustic communication experiment at 1,600 m depth using QPSK and 8PSK". In: *OCEANS 2010*, pp. 1–5, 2010. doi: 10.1109/OCEANS.2010.5664308.

[73] TIVEY, M., FUCILE, P., SICHEL, E. "A low power, low cost, underwater optical communication system". In: *Ridge 2000 Events*, pp. 27–29, April 2004.

[74] SCHILL, F., ZIMMER, U. R., TRUMPF, J. "Visible spectrum optical communication and distance sensing for underwater applications". In: *Australian Conf. on Robotics and Automation (ACRA), Canberra, Australia*, December 2004.

[75] DONIEC, M., VASILESCU, I., CHITRE, M., et al. "AquaOptical: A Lightweight Device for High-Rate Long-Range Underwater Point-to-Point Communication". In: *OCEANS 2009, MTS/IEEE Biloxi - Marine Technology for Our Future: Global and Local Challenges*, pp. 1–6, 2009.

[76] FARR, N., BOWEN, A., WARE, J., et al. "An integrated, underwater optical /acoustic communications system". In: *OCEANS 2010 IEEE*, pp. 1–6, Sydney, Australia, May 2010. IEEE. doi: 10.1109/OCEANSSYD.2010.5603510.

[77] LI, B., ZHOU, S., HUANG, J., et al. "Scalable OFDM design for underwater acoustic communications". In: *Acoustics, Speech and Signal Processing, 2008. ICASSP 2008. IEEE International Conference on*, pp. 5304–5307, March 2008. doi: 10.1109/ICASSP.2008.4518857.

[78] M. STOJANOVIC, J. A. CATIPOVIC, J. G. P. "Adaptive multichannel combining and equalization for underwater acoustic communications", *Journal of the Acoustical Society of America*, v. 94, n. 3, pp. 1621–1631, 1993.

[79] ZHOU, S., WANG, Z. *OFDM for Underwater Acoustic Communication*. 1 ed. , Wiley, 2014.

[80] XU, X., WANG, Z., ZHOU, S., et al. "Parameterizing both path amplitude and delay variations of underwater acoustic channels for block decoding of orthogonal frequency division multiplexing", *J. Acoust. Soc. Am*, v. 31, n. 6, pp. 4672–4679, 2012.

[81] DINIZ, P. S. R., MARTINS, W. A., LIMA, M. V. S. *Block Transceivers: OFDM and Beyond*. 1 ed. , Morgan & Claypool, New York, NY, 2012.

[82] MARTINS, W. A., DINIZ, P. S. R. "Pilot-aided designs of memoryless block equalizers with minimum redundancy". In: *Circuits and Systems (ISCAS), Proceedings of 2010 IEEE International Symposium on*, pp. 3312–3315, May 2010. doi: 10.1109/ISCAS.2010.5537975.

[83] PORTER, M. B., Y.-C.LIU. "Finite element ray tracing", *Theoretical and Computational Acoustics*, v. 2, pp. 947–966, 1994.

[84] SIMÕES, I., XAVIER, F., BARREIRA, L., et al. "Medições geoacústicas em sedimentos marinhos da plataforma continental próxima a Arraial do Cabo-RJ - Brasil". In: *2as Jornadas de Engenharia Hidrográfica, Lisbon*, June 2012.

[85] HAYKIN, S. *Communication Systems*. 4 ed. , John Wiley & Sons, Inc., 2001.

[86] MARTINS, W. A., DINIZ, P. S. R. "LTI Transceivers With Reduced Redundancy", *Signal Processing, IEEE Transactions on*, v. 60, n. 2, pp. 766–780, Feb. 2012. doi: 10.1109/TSP.2011.2174056.